THE METHOD OF LINES SOLUTION OF DISCRETE ORDINATES METHOD FOR NONGRAY MEDIA

A THESIS SUBMITTED TO
THE GRADUATE SCHOOL OF NATURAL AND APPLIED SCIENCES
OF
MIDDLE EAST TECHNICAL UNIVERSITY

BY

FATMA NİHAN ÇAYAN

IN PARTIAL FULFILLMENT OF THE REQUIREMENTS
FOR
THE DEGREE OF MASTER OF SCIENCE
IN
CHEMICAL ENGINEERING

JULY 2006

Approval of the Graduate School of Natural and Applied Sciences

Prof. Dr. Canan Özgen
Director

I certify that this thesis satisfies all the requirements as a thesis for the degree of Master of Science.

Prof. Dr. Nurcan Baç
Head of Department

This is to certify that we have read this thesis and that in our opinion it is fully adequate, in scope and quality, as a thesis and for the degree of Master of Science.

Prof. Dr. Faruk Arınç
Co-Supervisor

Prof. Dr. Nevin Selçuk
Supervisor

Examining Committee Members

Prof. Dr. Nurcan Baç (METU, CHE)

Prof. Dr. Nevin Selçuk (METU, CHE)

Prof. Dr. Faruk Arınç (METU, ME)

Asst. Prof. Dr. Görkem Kırbaş (METU, CHE)

Asst. Prof. Dr. Nimeti Döner (DPU, ME)

I hereby declare that all information in this document has been obtained and presented in accordance with academic rules and ethical conduct. I also declare that, as required by these rules and conduct, I have fully cited and referenced all material and results that are not original to this work.

Name, Last name : Fatma Nihan Çayan

Signature :

ABSTRACT

THE METHOD OF LINES SOLUTION OF DISCRETE ORDINATES METHOD FOR NONGRAY MEDIA

Çayan, Fatma Nihan

M.Sc., Department of Chemical Engineering

Supervisor: Prof. Dr. Nevin Selçuk

Co-Supervisor: Prof. Dr. Faruk Arınç

July 2006, 110 Pages

A radiation code based on method of lines (MOL) solution of discrete ordinates method (DOM) for the prediction of radiative heat transfer in nongray absorbing-emitting media was developed by incorporation of two different gas spectral radiative property models, namely wide band correlated-*k* (WBCK) and spectral line-based weighted sum of gray gases (SLW) models.

Predictive accuracy and computational efficiency of the developed code were assessed by applying it to the predictions of source term distributions and net wall radiative heat fluxes in several one- and two-dimensional test problems including isothermal/non-isothermal and homogeneous/non-homogeneous media of water vapor, carbon dioxide or mixture of both, and benchmarking its steady-state predictions against line-by-line (LBL) solutions and measurements available in the

literature. In order to demonstrate the improvements brought about by these two spectral models over and above the ones obtained by gray gas approximation, predictions obtained by these spectral models were also compared with those of gray gas model. Comparisons reveal that MOL solution of DOM with SLW model produces the most accurate results for radiative heat fluxes and source terms at the expense of computation time when compared with MOL solution of DOM with WBCK and gray gas models.

In an attempt to gain an insight into the conditions under which the source term predictions obtained with gray gas model produce acceptable accuracy for engineering applications when compared with those of gas spectral radiative property models, a parametric study was also performed. Comparisons reveal reasonable agreement for problems containing low concentration of absorbing-emitting media at low temperatures.

Overall evaluation of the performance of the radiation code developed in this study points out that it provides accurate solutions with SLW model and can be used with confidence in conjunction with computational fluid dynamics (CFD) codes based on the same approach.

Keywords: Method of Lines, Discrete Ordinates Method, Nongray media, Wide Band Correlated-*k* (WBCK) model, Spectral Line-Based Weighted Sum of Gray Gases (SLW) model

ÖZ

GRİ OLMAYAN ORTAMLAR İÇİN BELİRLİ YÖNLER YÖNTEMİNİN ÇİZGİLER METODUYLA ÇÖZÜMÜ

Çayan, Fatma Nihan

Yüksek Lisans, Kimya Mühendisliği Bölümü

Tez Yöneticisi: Prof. Dr. Nevin Selçuk

Ortak Tez Yöneticisi: Prof. Dr. Faruk Arınç

Temmuz 2006, 110 Sayfa

Gri olmayan yutan-yayan ortamlardaki ışınım ısı transferinin öngörülmesi için iki farklı gaz spektral ışınım özellik modeli; geniş bantlı bağdaşık-*k* modeli ve spektral çizgilere dayalı gri gazların ağırlıklı toplamı modeli, belirli yönler yönteminin çizgiler metoduyla çözümü ile birleştirilerek yeni bir ışınım kodu geliştirilmiştir.

Geliştirilen kodun öngörme doğruluğunun ve bilgisayar zamanı açısından veriminin değerlendirilmesi için, kod eş-sıcaklıklı/farklı-sıcaklıklı, homojen/homojen-olmayan, karbondioksit, su buharı veya ikisinin karışımını içeren çeşitli bir- ve iki-boyutlu test problemlerine uygulanmış ve kodun yatışkın durum için ürettiği öngörüler literatürdeki çizgi-çizgi çözümleriyle ve ölçümlerle karşılaştırılmıştır. Kullanılan spektral modellerin gri gaz yaklaşımının üzerine

getirdikleri iyileşmeyi görmek için, bu modellerle elde edilen öngörüler gri gaz modeliyle elde edilen öngörülerle karşılaştırılmıştır. Karşılaştırmalar, geniş bantlı bağdaşık-*k* ve gri gaz modelli çözümlere kıyasla spektral çizgilere dayalı gri gazların ağırlıklı toplamı modelli çözümün fazla hesaplama zamanı pahasına en doğru ışınım ısı akısı ve kaynak terimi ürettiğini göstermiştir.

Gri gaz modeliyle elde edilen kaynak terimi öngörülerinin, spektral model kullanılarak elde edilen öngörülerle karşılaştırıldığında, mühendislik uygulamaları için hangi şartlarda kabul edilebilir doğrulukta olduğunu görebilmek için ayrıca parametrik bir çalışma yapılmış ve sadece düşük sıcaklık ve konsantrasyonlardaki yutan-yayan ortamlarda bu uyumun ortaya çıktığı görülmüştür.

Bu çalışmada geliştirilen ışınım kodunun değerlendirmesi sonucu bu kodun spektral çizgilere dayalı gri gazların ağırlıklı toplamı modeli kullanıldığında doğru çözümler sağladığı ve bu nedenle aynı yönteme dayalı hesaplamalı akışkanlar dinamiği kodları ile birlikte güvenle kullanılabileceği görülmüştür.

Anahtar kelimeler: Çizgiler Metodu, Belirli Yönler Yöntemi, Gri olmayan ortam, Geniş Bantlı Bağdaşık-*k* modeli, Spectral Çizgilere Dayalı Gri Gazların Ağırlıklı Toplamı modeli

to *my precious family*

and

Ertan

ACKNOWLEDGEMENTS

I wish to express my deepest gratitude to my supervisor, Prof. Dr. Nevin Selçuk for her guidance and encouragement throughout this study.

I would like to show my appreciation to my co-supervisor Prof. Dr. Faruk Arınç, for his precious suggestions and support.

I also thank to the research team members for their friendship and support during my study; Onur Afacan, Mehmet Kürkçü, Ahmet Bilge Uygur, Yusuf Göğebakan, Dr. Tanıl Tarhan, Mehmet Moralı and Düriye Ece Alagöz. Special thanks to Işıl, for her outstanding help and patience.

Special thanks go to my family, Asuman, Ömer Faruk and Neval Çayan, for their great support, encouragement and unshakable faith in me.

Finally, my warmest thanks to my fiancé Ertan, for his understanding, endless patience and encouragement when it was most required.

TABLE OF CONTENTS

LIST OF TABLES

TABLES

LIST OF FIGURES

FIGURES

LIST OF SYMBOLS

a	gray gas weights, [-]
C_{abs}	absorption cross section, [mol/m^2]
$\tilde{C}_{abs}$	supplemental absorption cross-section, [mol/m^2]
C_{ij}	coefficients, [-]
$div\ \boldsymbol{q}$	source term, [kW/m^3]
$\mathbf{e_i}$	unit vector in the coordinate direction i, [-]
E_b	blackbody emissive power, [W/m^2]
E_1	exponential integral of order 1, [-]
F	blackbody fractional function, [-]
F_s	absorption-line blackbody distribution function, [-]
I	radiative intensity, [W/m^{2}sr]
G	total incident heat flux, [W/m^2]
k_t	time constant, [(m/s)$^{-1}$]
ℓ	index for a discrete direction, [-]
L	distance between parallel plates, [m]
L_m	mean beam length, [m]
m	discrete direction, [-]
$\mathbf{n}$	unit normal vector, [-]
N	molar density, [mol/m^3]
p_i	poles, [-]
$\boldsymbol{q}$	radiative heat flux, [kW/m^2]
q$^+$	incident radiative heat flux, [W/m^2]
q$^-$	leaving radiative heat flux, [W/m^2]
q_{net}	net radiative heat flux, [kW/m^2]
$\mathbf{r}$	position vector, [-]

r	co-ordinate axis in cylindrical geometry, [-]
s	distance, [m]
t	pseudo-time variable, [s]
T	temperature, [K]
$w_{m,\ell}$	quadrature weight for ordinate m, ℓ , [-]
Y	species mole fraction, [-]
z	co-ordinate axis in cylindrical geometry, [-]

Greek Symbols

α	band strength parameter, [$cm^{-1}/(g/m^2)$]
β	line overlap parameter, [-]
ε	emissivity, [-]
ϕ	azimuthal angle, [rad]
γ	angular differencing coefficient, [-]
η	wave number, [cm^{-1}]
κ	gray gas absorption coefficients, [m^{-1}]
μ	direction cosines, [-]
θ	polar angle, [rad]
ρ	density of the absorbing gas, [g/m^3]
σ	Stefan-Boltzmann constant, $=5.67\times10^{-8}$ [$W/m^2\ K^4$]
τ	optical thickness, [-]
ω	band strength parameter, [cm^{-1}]
ξ	direction cosines [-], re-ordered wave number, [cm^{-1}]
ς	direction cosines, [-]
ζ	direction cosine (μ, ς, ξ), [-]
$\mathbf{\Omega}$	direction of radiation intensity, [-]
$d\mathbf{\Omega}$	solid angle, [-]
$\mathbf{\Omega}_m$	ordinate direction, [-]
$\in$	error tolerance, [-]

Superscripts and Subscripts

b	black body
g	gas
j	gray gas
k	wide band, gray gas for CO_2
ref	reference
t	print time
w	wall
η	spectral variable
$'$	incident

Abbreviations

CFD	computational fluid dynamics
DOM	discrete ordinates method
DSS012	two-point upwind differencing scheme
DSS014	three-point upwind differencing scheme
EWBM	exponential wide band model
FDM	finite difference method
GTCS	gas turbine combustor simulator
LBL	line-by-line
MOL	method of lines
NEQN	number of ODEs
NG	number of gray gases
NR	number of grids in r direction
NZ	number of grids in z direction
NWB	number of wide bands
ODE	ordinary differential equation
PDE	partial differential equation
RTE	radiative transfer equation
SLW	spectral line-based weighted sum of gray gases
WBCK	wide band correlated-*k*
WSGG	weighted sum of gray gases

CHAPTER 1

INTRODUCTION

Prediction of transient behavior of turbulent, reacting and radiating flows is of great importance from the design stand-point of high temperature industrial systems such as furnaces and combustors. Thermal radiation is the predominant mode of heat transfer in such applications. Accurate modeling of these systems necessitates reliable evaluation of the medium radiative properties and accurate solution of the radiative transfer equation (RTE) in conjunction with the time-dependent conservation equations for mass, momentum, energy and chemical species.

Standard computational fluid dynamics (CFD) codes are based on the simplest and most practical approach in use at present, i.e., the solution of the Reynolds-Averaged Navier-Stokes equations along with turbulence models. On the other hand, the most straightforward approach to the solution of turbulent flows is the direct numerical simulation (DNS) in which the governing equations are discretized and solved numerically for the time development of detailed, unsteady structures in a turbulent flow field without using any turbulence models. However, a lot of grid points as well as time steps are needed for DNS and hence the computational effort is enormous. Use of efficient methods can decrease the computational time considerably. This can be achieved in two ways; the first way is to increase the order of spatial discretization method, resulting in high accuracy with less grid points, and the second way is to use a highly accurate but also a stable numerical algorithm for the time integration. The method of lines (MOL) that meets

the latter requirement is an alternative approach for time dependent problems, which does not involve the discretization of all variables. The MOL consists of converting the system of PDEs into an ordinary differential equations (ODE) initial value problem by discretizing the spatial derivatives together with the boundary conditions via Taylor series, or weighted residual techniques and integrating ODEs using a sophisticated ODE solver, which takes the burden of time discretization and chooses the time steps in such a way that maintains the accuracy and stability of the evolving solution. The advantages of MOL approach are twofold. First, it is possible to achieve higher order approximations in the discretization of spatial derivatives without significant increases in computational complexity and without additional difficulties with boundary conditions. Second, the use of highly efficient and reliable initial value ODE solvers means that comparable orders of accuracy can also be achieved in the time integration without using extremely small steps.

In recent years, studies carried out on a novel code, MOLS4MEE (MOL Solution for Momentum and Energy Equations), based on DNS demonstrated that conservation equations for mass, momentum and energy for transient problems can be solved simultaneously with ease by MOL approach [1-6]. Recently, the MOLS4MEE code was parallelized and it is found that parallelization provides accurate solution of flow fields using higher number of grid points required in DNS applications and also by parallelization CPU time requirement decreases [7].

MOL solution of discrete ordinates method (DOM) is a promising method when RTE is to be solved in conjunction with the time-dependent conservation equations for mass, momentum, energy and species. It is based on the implementation of false-transients approach to the discrete ordinates representation of RTE. Solution of the RTE by using this approach not only makes its coupling with computational fluid dynamics (CFD) codes easier, but it also alleviates the slow-convergence problem encountered in the implementation of the classical DOM to steady-state problems involving strongly scattering media [8].

In this approach, the integro-differential equation representing the RTE is converted into a system of PDEs by the application of DOM. Implementation of false-transients approach to the resulting equations, followed by discretization of spatial derivatives transforms system of PDEs into an ODE initial value problem.

Starting from an initial condition for radiation intensities in all discrete directions the resulting ODE system is integrated until steady-state by using a powerful ODE solver.

This method has first been suggested by Yücel [9] for a two-dimensional rectangular enclosure surrounded by black walls containing absorbing-emitting and scattering medium and tested for accuracy by benchmarking its predictions against exact solutions. Later, the predictive accuracy of MOL solution DOM was investigated by comparing its steady-state predictions with analytical solution of DOM [10] and exact solutions of RTE on a one-dimensional slab containing absorbing-emitting gray medium with uniform temperature profile [11, 12]. The method was then extended to a three-dimensional problem, box-shaped enclosure with black walls bounding absorbing-emitting gray medium with steep temperature gradients typical of operating furnaces and combustors, and validated against exact solutions obtained previously for the same problem [13, 14]. The predictive accuracy of MOL solution of DOM was also tested on a three-dimensional rectangular enclosure problem [14, 15] containing absorbing-emitting-scattering medium with gray walls by comparing its predictions with those of zone method [14] and measurements. Later, the method was applied to axisymmetric cylindrical enclosures containing absorbing, emitting, gray medium and its predictions were validated against exact solutions and measurements [16]. The method was also found to be successfully applicable to solution of transient radiative transfer problems [17]. Recently, the method was used in conjunction with a CFD code based on MOL approach for modeling transient, radiating, laminar, axisymmetric flow of a gray, absorbing, emitting fluid in a heated pipe and favorable agreement obtained between steady-state predictions and solutions available in the literature [18].

Encouraging performance of MOL solution of DOM in the above-mentioned studies has led to extension of the method to treatment of nongray media by incorporation of gas spectral radiative property models compatible with MOL solution of DOM. Wide variety of gas spectral radiative property models with different degrees of complexity and accuracy are available in the literature. LBL model [19], which is the most accurate of all, requires calculation of radiative properties for millions of vibrational-rotational lines, and hence, its computational

cost is extremely high for practical engineering applications. Indeed, they only serve as benchmarks to test the accuracy of other approximate models. The significant computational burden required by LBL model has necessitated the use of band models which are designed to approximate the nongray gas behavior over wave number intervals within which the radiative properties are assumed to be constant. Depending on the width of wave number intervals, band models are classified as narrow band [20, 21] and wide band [22, 23] models. Drawback of these models is that they provide gas transmissivities or absorptivities instead of absorption coefficients, which are required for the solution of RTE. Recently there has been an increasing effort for the development of gas spectral radiative property models which yield absorption coefficients and therefore are suitable for incorporation into any RTE solution technique. The correlated-*k* (CK) distribution model originally developed by Goody *et al*. [24] and Lacis and Oinas [25] for atmospheric radiation, presents such an opportunity. This model neglects the variation of blackbody intensity over a band and therefore enables the replacement of spectral integration over wave number within a band by a quadrature over the absorption coefficient. However, CK model is computationally very demanding if narrow bands are utilized [26]. In order to alleviate this problem, recently the CK model has been extended to wide bands, yielding WBCK model [27-30]. In the WBCK model, the wave number spectrum is re-ordered to yield a smooth function of the absorption coefficient around the band centers within the wide band, so that for a certain wave number interval, a set of mean values of the absorption coefficient can be introduced [23]. For the re-ordered wave number, Denison and Fiveland [29] developed a closed-form function. Implementation of this function to WBCK model was demonstrated on DOM solution of RTE by Ströhle and Coelho [23] and predictions were validated against narrow band and LBL results. Global models, on the other hand, approximate the radiative properties of the gases over the entire spectrum instead of wave number intervals. The most commonly used global model is the weighted sum of grey gases (WSGG) model which is originally developed by Hottel and Sarofim [31] within the framework of zone method. In this model the nongray gas is replaced by a number of gray gases associated with certain weight factors and the heat transfer calculations are then performed independently for each gray gas. The weight factors are calculated from a fit to the total emissivity data [32]. This model offers the

advantages of accuracy and computational efficiency for the calculation of total emissivity. Modest [33] extended the applicability of this model for the solution of RTE. Later, Denison and Webb [34-39] improved this model to spectral line-based weighted sum of grey gases (SLW) model by expressing the gray gas weights in terms of absorption-line blackbody distribution function [36, 39] derived from the high resolution HITRAN database [40]. Denison and Webb [35, 37, 38, 41] validated the model against LBL solutions on a wide variety of one- and two-dimensional axisymmetric enclosure problems including absorbing-emitting and scattering medium. Solovjov and Webb [42, 43] further improved the model for multi-component gas mixtures including soot particles. Goutiere *et al*. [44] compared SLW model with various nongray models and showed that SLW model is the best choice with regard to computational time and accuracy.

The importance of reliable evaluation of medium radiative properties and the favorable comparisons obtained with MOL solution of DOM have led to incorporation of accurate and efficient gas spectral radiative property models into MOL solution of DOM.

Therefore, the principal objective of the present study has been to develop a radiation code based on MOL solution of DOM for simulation of radiative transfer in nongray media. To achieve this objective, a computer code was developed by incorporation of WBCK and SLW models into MOL solution of DOM. The predictive accuracy of this technique was examined on the following test problems:

- Several one-dimensional test problems involving isothermal/non-isothermal and homogeneous/non-homogeneous media of water vapor, carbon dioxide and mixture of both,
- A two-dimensional axisymmetric cylindrical enclosure problem containing isothermal-homogeneous medium of water vapor
- Gas Turbine Combustor Simulator (GTCS) containing a non-homogeneous absorbing-emitting medium with gray walls for which experimental data required for both the application and validation of the radiation code were previously made available within the framework of NATO-AGARD Project T51/PEP.

CHAPTER 2

NUMERICAL SOLUTION TECHNIQUE

In this chapter, method of lines (MOL) solution of discrete ordinates method (DOM) is described for mathematical modeling of radiative heat transfer in axisymmetric cylindrical enclosures containing absorbing-emitting, non-scattering radiatively nongray medium with diffuse gray walls. Values of blackbody emissive power are assumed to be known at all points within the enclosed medium, and at all points on the interior bounding surfaces of the enclosure. Based on this physical problem, equations representing MOL solution of DOM are derived starting from the radiative transfer equation (RTE) for axisymmetric cylindrical coordinate system. This is followed by the numerical solution procedure utilized for the MOL solution of DOM.

2.1 Radiative Transfer Equation (RTE)

The basis of all methods for the solution of radiation problems is the radiative transfer equation (RTE), which is derived by writing a balance equation for radiant energy passing in a specified direction through a small volume element in an absorbing-emitting nongray medium and can be written in the form:

$$\frac{dI_\eta}{ds} = \left(\mathbf{\Omega}\cdot\nabla\right) I_\eta(\mathbf{r},\mathbf{\Omega}) = -\kappa_\eta I_\eta(\mathbf{r},\mathbf{\Omega}) + \kappa_\eta I_{b\eta}(\mathbf{r}) \tag{2.1}$$

where $I_\eta(\mathbf{r},\mathbf{\Omega})$ is the spectral radiation intensity at position $\mathbf{r}$ in the direction $\mathbf{\Omega}$. κ_η is

the spectral absorption coefficient of the medium and $I_{b\eta}$ is the spectral blackbody radiation intensity at the temperature of the medium. The expression on the left-hand side represents the change of the intensity in the specified direction $\mathbf{\Omega}$. The first term on the right-hand side is attenuation through absorption and the second term represents augmentation due to emission.

In axisymmetric cylindrical geometry (r, z), the directional derivative of radiation intensity can be expressed as

$$\frac{dI_\eta}{ds} = \frac{\partial I_\eta}{\partial r}\frac{dr}{ds} + \frac{\partial I_\eta}{\partial \phi}\frac{d\phi}{ds} + \frac{\partial I_\eta}{\partial z}\frac{dz}{ds} \tag{2.2}$$

where

$$\frac{dr}{ds} = \mathbf{\Omega}\cdot\mathbf{e}_\mathbf{r} = \mu \tag{2.3}$$

$$\frac{d\phi}{ds} = \mathbf{\Omega}\cdot\mathbf{e}_{\mathbf{\Psi}} = -\frac{\varsigma}{r} \tag{2.4}$$

$$\frac{dz}{ds} = \mathbf{\Omega}\cdot\mathbf{e}_\mathbf{z} = \xi \tag{2.5}$$

In Eqs. (2.3-2.5) $\mathbf{e_r}$, $\mathbf{e_\psi}$ and $\mathbf{e_z}$ are unit vectors and $\mu\,(=\sin\theta\cos\phi)$, $\varsigma\,(=\sin\theta\sin\phi)$ and $\xi\,(=\cos\theta)$ are direction cosines in r, ψ and z directions, respectively (see Figure 2.1). Hence, the derivative of radiation intensity can be written as:

$$\frac{dI_\eta}{ds} = \mu\frac{\partial I_\eta}{\partial r} - \frac{\varsigma}{r}\frac{\partial I_\eta}{\partial \phi} + \xi\frac{\partial I_\eta}{\partial z} \tag{2.6}$$

The directional derivative (*d/ds*) is written in so-called conservation form to assure that approximation to the RTE retain conservation properties. Mathematically it means that upon multiplying the differential equation by a volume element, the resulting coefficients of any differential term does not contain the variable of differentiation. Eq.(2.6) is not yet in conservative form, since the coefficient of $\partial I_\eta/\partial\phi$ is ς/r and $\varsigma=\sin\theta\sin\phi$. This difficulty is easily remedied by adding and subtracting a term, $\frac{\mu}{r}I_\eta$ to Eq. (2.6) [45] as shown below:

$$\frac{dI_\eta}{ds} = \mu \frac{\partial I_\eta}{\partial r} - \frac{\varsigma}{r}\frac{\partial I_\eta}{\partial \phi} + \xi \frac{\partial I_\eta}{\partial z} + \frac{\mu}{r} I_\eta - \frac{\mu}{r} I_\eta \tag{2.7}$$

$$\frac{dI_\eta}{ds} = \frac{\mu}{r}\left[r\frac{\partial I_\eta}{\partial r} + \frac{\partial r}{\partial r} I_\eta \right] - \frac{1}{r}\left[\varsigma \frac{\partial I_\eta}{\partial \phi} + \frac{\partial \varsigma}{\partial \phi} I_\eta \right] + \xi \frac{\partial I_\eta}{\partial z} \tag{2.8}$$

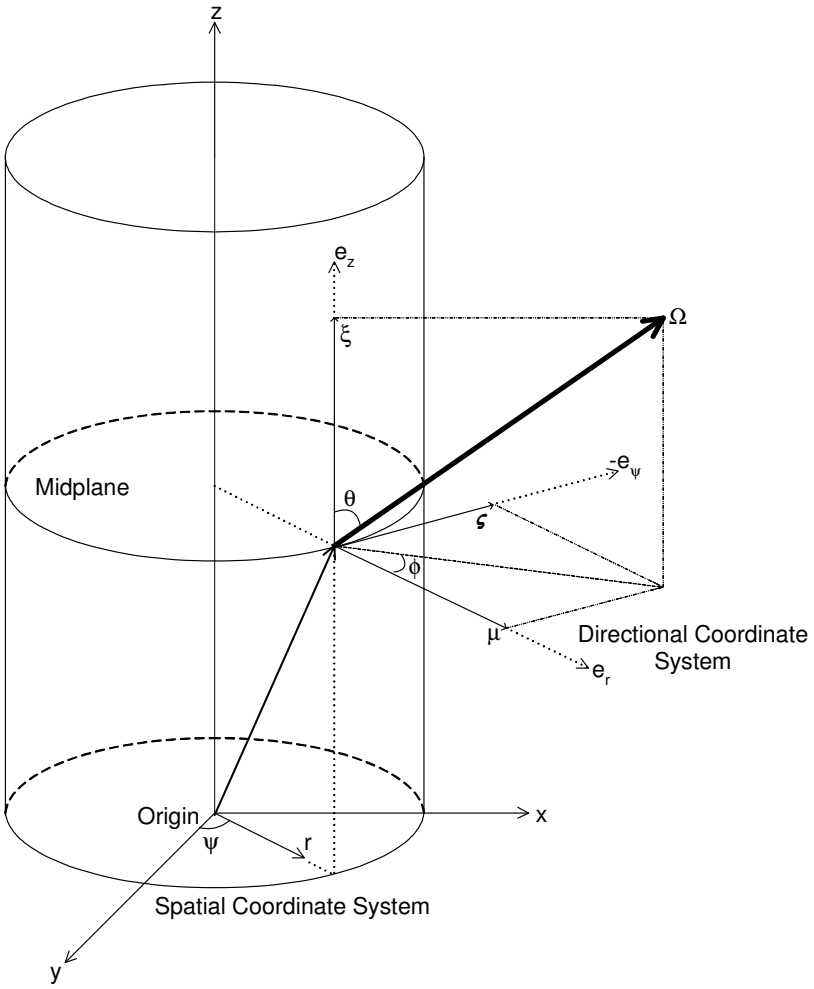

Figure 2.1 Coordinate system

Consequently in conservative form RTE (Eq. (2.1)) in axisymmetrical cylindrical coordinates takes the following form

$$\frac{dI_\eta}{ds} = \frac{\mu}{r}\frac{\partial(rI_\eta)}{\partial r} - \frac{1}{r}\frac{\partial(\varsigma I_\eta)}{\partial \phi} + \xi\frac{\partial I_\eta}{\partial z} = -\kappa_\eta I_\eta + \kappa_\eta I_{b\eta} \tag{2.9}$$

If the surfaces bounding the medium are diffuse and gray at specified temperature, the Eq. (2.1) is subject to the boundary condition:

$$I_\eta(\mathbf{r_w},\mathbf{\Omega}) = \varepsilon_w I_{b\eta}(\mathbf{r_w}) + \frac{(1-\varepsilon_w)}{\pi}\int_{\mathbf{n_w}\cdot\mathbf{\Omega}'<0} \left|\mathbf{n_w}\cdot\mathbf{\Omega}'\right| I_\eta(\mathbf{r_w},\mathbf{\Omega}')d\mathbf{\Omega}' \quad \mathbf{n}\cdot\mathbf{\Omega}>0 \tag{2.10}$$

where $I_\eta(\mathbf{r_w},\mathbf{\Omega})$ and $I_\eta(\mathbf{r_w},\mathbf{\Omega}')$ are the spectral radiative intensities leaving and incident on the surface at a boundary location, ε_w is the surface emissivity, $I_{b\eta}(\mathbf{r_w})$ is the spectral blackbody radiation intensity at the surface temperature, $\mathbf{n}$ is the local outward surface normal and $\mathbf{n_w}\cdot\mathbf{\Omega}'$ is the cosine of the angle between incoming direction $\mathbf{\Omega}'$ and the surface normal. The first and the second terms on the right-hand side of Eq. (2.10) stand for the contribution to the leaving intensity due to emission from the surface and reflection of the incoming radiation, respectively.

In order to determine the radiative intensity distribution, the whole spectrum is discretized into wave number intervals within which the radiative properties are assumed to be constant. All wave number intervals having an absorption coefficient within a certain range are combined to a gray gas so the RTE (Eq.(2.1)) is solved for each gray gas by modifying the Eq. (2.1) as follows:

$$\frac{dI_j}{ds} = \frac{\mu}{r}\frac{\partial(rI_j)}{\partial r} - \frac{1}{r}\frac{\partial(\varsigma I_j)}{\partial \phi} + \xi\frac{\partial I_j}{\partial z} = \kappa_j(a_j I_b - I_j) \tag{2.11}$$

where subscript j denotes the spectral division and a_j are the blackbody weights determined from the standard blackbody distribution function in the Wide Band Correlated- k (WBCK) model [29], and from the absorption-line distribution functions in the Spectral Line-Based Weighted Sum of Gray Gases (SLW) model [35]. I_b ($\equiv \sigma T^4/\pi$) is the blackbody radiation intensity at the surface temperature. This form of RTE in Eq. (2.11) is known as the Weighted Sum of Gray Gases (WSGG) RTE derived by Modest [33] from WSGG model first introduced by Hottel

and Sarofim [31] for total emissivity calculation. Estimation of spectral properties will be discussed in detail in the following chapter.

Eq. (2.11) is solved for each gray gas with the following modified boundary condition:

$$I_j(\mathbf{r_w},\mathbf{\Omega}) = \varepsilon_w a_j I_b(\mathbf{r_w}) + \frac{(1 - \varepsilon_w)}{\pi} \int_{\mathbf{n_w}\cdot\mathbf{\Omega}' < 0} |\mathbf{n_w}\cdot\mathbf{\Omega}'| I_j(\mathbf{r_w},\mathbf{\Omega}') d\mathbf{\Omega}' \quad \mathbf{n}\cdot\mathbf{\Omega} > 0 \tag{2.12}$$

Once the radiation intensities are determined by solving Eq. (2.11) together with its boundary condition (Eq. (2.12)), quantities of interest such as radiative heat flux and energy source term can be readily evaluated. The net radiative heat flux on a surface element is defined as:

$$q_{net} = q^+ - q^- \tag{2.13}$$

where q^+ and q^- are incident and leaving wall heat fluxes, respectively. For a diffuse gray wall, q^+ and q^- are evaluated from:

$$q^+ = \sum_j^{NG} \int_{\mathbf{n}\cdot\mathbf{\Omega} < 0} |\mathbf{n}\cdot\mathbf{\Omega}| \cdot I_j \cdot d\mathbf{\Omega} \tag{2.14}$$

$$q^- = \sum_j^{NG} \int_{\mathbf{n}\cdot\mathbf{\Omega} > 0} |\mathbf{n}\cdot\mathbf{\Omega}| \cdot I_j \cdot d\mathbf{\Omega} \tag{2.15}$$

The radiative energy source term, divergences of the total radiative heat flux, for problems where temperature distributions are available is expressed as

$$div\,\mathbf{q} = \sum_j^{NG} \kappa_j \left(4\pi\, a_j I_b - \int_{4\pi} I_j(\mathbf{r},\mathbf{\Omega}) d\mathbf{\Omega} \right) \tag{2.16}$$

2.2 Discrete Ordinates Method (DOM)

This method is based on representation of continuous angular domain by a discrete set of ordinates with appropriate angular weights, spanning the total solid angle of 4π steradians. The discrete ordinates representation of RTE for an absorbing-emitting nongray medium in axisymmetric cylindrical coordinate system takes the following form:

$$\frac{\mu_m}{r}\frac{\partial\,(r\,I_j^m)}{\partial\,r}-\frac{1}{r}\frac{\partial\,(\varsigma_m I_j^m)}{\partial\,\phi}+\xi_m\frac{\partial\,I_j^m}{\partial\,z}=\kappa_j(a_j I_b-I_j^m) \tag{2.17}$$

where I_j^m [=I_j (r,z;θ,ϕ)] is the total spectral radiation intensity at position (r, z) in the discrete direction $\mathbf{\Omega_m}$ which is defined in terms of polar angle θ between z axis and $\mathbf{\Omega_m}$, and azimuthal angle ϕ between r and projection of $\mathbf{\Omega_m}$ on the x-y plane. The components of direction $\mathbf{\Omega_m}$ along the μ, ς and ξ axes are $\mu_m(=\sin\theta\cos\phi)$, $\varsigma_m(=\sin\theta\sin\phi)$ and $\xi_m(=\cos\theta)$, which are the direction cosines of $\mathbf{\Omega_m}$. Consequently, $\mu_m^2+\varsigma_m^2+\xi_m^2=1$. The direction $\mathbf{\Omega_m}$ can be pictured as a point on the surface of a unit sphere with which a surface area, w_m is associated. The w_m has the role of angular quadrature weights, with the obvious requirement that the weights sum to the total surface area of the unit sphere, i.e. $\sum_m w_m=\pi$.

The angular derivative term, which makes the solution of DOM complicated, is discretized by introducing an angular redistribution term $\gamma_{m,\ell\pm1/2}$, proposed by Carlson and Lathrop [46]. After discretization the angular derivative term takes the following form,

$$\left[\frac{\partial\,(\varsigma_m I_j^m)}{\partial\,\phi}\right]_{\Omega_m=\Omega_{m,\ell}}=\frac{(\gamma_{m,\ell+1/2}I_j^{m,\ell+1/2}-\gamma_{m,\ell-1/2}I_j^{m,\ell-1/2})}{w_{m,\ell}} \tag{2.18}$$

where $I_j^{m,\ell+1/2}$ and $I_j^{m,\ell-1/2}$ are radiation intensities in directions $m,\ell+1/2$ and $m,\ell-1/2$ which define the edges of angular range of $w_{m,\ell}$. The two terms on the right hand side of Eq. (2.18) represent the flow out of and into the angular range, respectively. The pair of indices m and ℓ in Eq (2.18) denotes constant polar angle θ

and variation of azimuthal angle ϕ, respectively. Direction cosines in standard quadrature sets are ordered in latitudes so that for each $\xi_m (=\cos\theta)$ level there will be several μ_m values [47]. A sketch of discrete directions represented by pair of indices m, ℓ in one octant of a unit sphere for S_4 order of approximation, which is explained in the following sections, is shown in Figure 2.2.

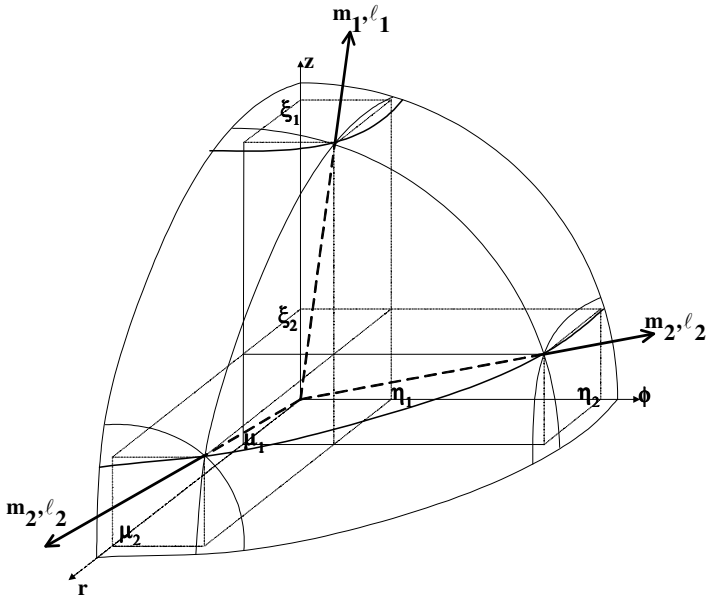

Figure 2.2 Schematic representation of discrete directions represented by m, ℓ in one octant of a unit sphere for S_4 order of approximation

As can be seen from the figure, for S_4 order of approximation there are two latitudes, ℓ_1 and ℓ_2, and one value of μ_m for the first latitude and two values of μ_m for the second latitude. In order to avoid physically unrealistic directional coupling, discrete directions for a given $\xi_m (=\cos\theta)$ should be ordered according to the values of $\phi (=\tan^{-1}(\varsigma/\mu))$.

By moving through the directions along the constant ξ_m level, the angular differencing coefficients, $\gamma_{m,\ell\pm1/2}$, are evaluated from the following recurrence

formula obtained for isotropic radiation ($I_j^{m,\ell} = I_j^{m,\ell-1/2} = I_j^{m,\ell+1/2}$) and for zero divergence [46]

$$\gamma_{m,\ell+1/2} = \gamma_{m,\ell-1/2m} + \mu_{m,\ell} w_{m,\ell} \qquad \ell = 1,\ 2,\ 3....\text{L, for fixed } \xi_m \tag{2.19}$$

When Eq. (2.18) is integrated over all angles (multiplied by $w_{m,\ell}$ and summed over m, ℓ) the result is

$$\sum_m (\ \gamma_{m,L+1/2}\ I_j^{m,L+1/2}\ -\ \gamma_{m,1/2}\ I_j^{m,1/2}) \tag{2.20}$$

which is made to vanish, as required for energy conservation, by setting

$$\gamma_{m,1/2} \ = \ \gamma_{m,L+1/2} \ = \ 0; \qquad \text{for all } m \tag{2.21}$$

where L is the maximum value of ℓ for a particular m. For example, for S_4 order of approximation L = 4 for m = 2 within two octants in the range $0 \le \phi \le \pi$.

Intensities at the edges of $w_{m,\ell}$ and $I_j^{m,\ell\pm1/2}$, are approximated in terms of discrete intensities $I_j^{m,\ell}$ by linear relations

$$I_j^{m,\ell+1/2} \ = \ \frac{I_j^{m,\ell} \ + \ I_j^{m,\ell+1}}{2} \ \text{ and } \ I_j^{m,\ell-1/2} \ = \ \frac{I_j^{m,\ell-1} \ + \ I_j^{m,\ell}}{2} \tag{2.22}$$

Equations (2.18) and (2.17), and the recurrence relations (Eqs. (2.19) and (2.22)) yield discrete ordinates equations for axisymmetric cylindrical geometry. The final form of discrete ordinates equation for axisymmetric cylindrical geometry takes the following form

$$\frac{\mu_{m,\ell}}{r}\frac{\partial\ (r\ I_j^{m,\ell})}{\partial\ r} - \frac{1}{r}\frac{(\gamma_{m,\ell+1/2} I_j^{m,\ell+1/2} - \gamma_{m,\ell-1/2} I_j^{m,\ell-1/2})}{w_{m,\ell}} + \xi_{m,\ell}\frac{\partial\ I_j^{m,\ell}}{\partial\ z} \tag{2.23}$$
$$= \kappa_j (a_j I_b - I_j^{m,\ell})$$

Boundary conditions required for the solution of Eq. (2.23) on the surface of the enclosure take the following forms for diffusely emitting-reflecting surfaces

$$\text{at } r = L_r; \quad I_j^{m,\ell} = \varepsilon_w a_j I_b(\mathbf{r_w}) + \frac{(1 - \varepsilon_w)}{\pi} \sum_{m',\ell'} w_{m',\ell'} \mu_{m',\ell'} I_j^{m',\ell'} \quad \mu_{m,\ell} < 0 \tag{2.24}$$

$$\text{at } z = 0; \quad I_j^{m,\ell} = \varepsilon_w a_j I_b(\mathbf{r_w}) + \frac{(1 - \varepsilon_w)}{\pi} \sum_{m',\ell'} w_{m',\ell'} \left|\xi_{m',\ell'}\right| I_j^{m',\ell'} \quad \xi_{m,\ell} > 0 \tag{2.25}$$

$$\text{at } z = L_z; \quad I_j^{m,\ell} = \varepsilon_w a_j I_b(\mathbf{r_w}) + \frac{(1 - \varepsilon_w)}{\pi} \sum_{m',\ell'} w_{m',\ell'} \xi_{m',\ell'} I_j^{m',\ell'} \quad \xi_{m,\ell} < 0 \tag{2.26}$$

On the axis of symmetry (r=0) the exact boundary condition is given by

$$\left(\frac{\partial I_j}{\partial \phi}\right)_{\theta = \text{constant}} = 0 \tag{2.27}$$

In discrete terms this is equivalent to $I_j^{m,\ell}$ being independent of ℓ for a fixed m. With a finite quadrature this condition is generally not satisfied exactly for all values of ℓ. In order to overcome this difficulty, conservation of heat flux on the axis of symmetry for the radial component of the net heat flux ($\boldsymbol{q}_r$(r=0)=0), is suggested by Hyde and Truelove [47]. This condition is satisfied if the axis of symmetry is treated as a fictitious, perfectly specular reflecting boundary ($I_j(r=0;\theta, \phi) = I_j^{'}(r=0; \theta, \pi - \phi)$).

Consequently, boundary condition in discrete terms at the axis of symmetry can be written as

$$\text{at } r = 0; \qquad I_j^{m,\ell} = I_j^{m',\ell'} \qquad \mu_{m',\ell'} = -\mu_{m,\ell} \qquad \mu_{m,\ell} > 0 \tag{2.28}$$

In Eqs. (2.24-2.26) and (2.28), the values m, ℓ and m', $\ell^{'}$ denote outgoing and incoming directions, respectively.

Once the intensity distribution is determined by solving Eq. (2.23) together with its boundary conditions, the net radiative flux and source term can be obtained from the following equations

$$q_{net} = q^{+} - q^{-} = \varepsilon_w \left(\sum_{j}^{NG} \sum_{m}^{M} w_m \zeta_m I_j^m - a_j \pi I_b \right) \tag{2.29}$$

$$div\, \boldsymbol{q} = \sum_{j}^{NG} \kappa_j (4\pi a_j I_b - \sum_{m}^{M} w_m I_j^m) \tag{2.30}$$

2.3 The Method of Lines (MOL) Solution of DOM

The solution of discrete ordinates equations with MOL is carried out by adaptation of the false-transients approach which involves incorporation of a pseudo-time derivative of intensity into the discrete ordinates equations [9]. Adaptation of the false-transient approach to Eq. (2.23) yields:

$$k_t \frac{\partial I_j^{m,\ell}}{\partial \mathrm{t}} = -\frac{\mu_{m,\ell}}{r}\frac{\partial (r\, I_j^{m,\ell})}{\partial r} + \frac{1}{r}\frac{(\gamma_{m,\ell+1/2} I_j^{m,\ell+1/2} - \gamma_{m,\ell-1/2} I_j^{m,\ell-1/2})}{w_{m,\ell}} - \xi_{m,\ell}\frac{\partial I_j^{m,\ell}}{\partial z} + \kappa_j (a_j I_b - I_j^{m,\ell}) \tag{2.31}$$

where t is the pseudo-time variable and k_t is a time constant with dimension $[(\mathrm{m/s})^{-1}]$ which is introduced to maintain dimensional consistence in the equation and it is taken as unity.

The system of PDEs with initial and boundary-value independent variables is then transformed into an ODE initial value problem by using MOL approach [48]. The transformation is carried out by representation of the spatial derivatives with the algebraic finite-difference approximations. Starting from an initial condition for radiation intensities in all directions, the resulting ODE system is integrated until steady state by using a powerful ODE solver. The ODE solver takes the burden of time discretization and chooses the time steps in a way that maintains the accuracy and stability of the evolving solution. Any initial condition can be chosen to start the integration, as its effect on the steady-state solution decays to insignificance. To stop the integration at steady state, a convergence criterion was introduced. If the intensities at all nodes and ordinates for all gray gases satisfy the condition given below, the solution at current time is considered to be the steady state solution and the integration is terminated. The condition for steady state is

$$\frac{|I_t - I_{t\text{-}1}|}{I_{t\text{-}1}} < \in \tag{2.32}$$

where $\in$ is the error tolerance, the subscript t denotes the solution at current print time and subscript $t–1$ indicates solutions at previous print time. As a result, evolution of radiative intensity with time at each node and ordinate is obtained. The steady-state intensity values yield the solution to Eq. (2.31) because the artificial

time derivative vanishes at steady state.

Once the steady state intensities at all grid points for all gray gases are available, the net radiative heat flux on enclosure boundaries and radiative source term at interior grid points can be evaluated by using Eqs. (2.29) and (2.30), respectively.

2.3.1 Parameters Affecting the Accuracy of MOL Solution of DOM

The accuracy and efficiency of MOL solution of DOM is determined by the following parameters:

- accuracy of angular discretization technique
- accuracy of the spatial discretization technique
- accuracy of the ODE solver utilized for time integration

Angular discretization is characterized by the angular quadrature scheme and order of approximation. In an investigation carried out by Selçuk and Kayakol [49] on the assessment of the effect of these parameters on the predictive accuracy of DOM by verification against exact solutions, it was concluded that the order of approximation plays a more significant role than angular quadrature scheme and spatial differencing schemes in the accuracy of predicted radiative heat fluxes and radiative energy source terms.

The order of approximation of DOM determines the total number of discrete directions, M. A sketch of the directions used in one octant of a unit sphere for S_2, S_4, S_6 and S_8 order of approximations is shown in Figure 2.3. As can be seen from the figure, discrete directions are ordered in levels (constant θ) and number of directions is different at each level. Table 2.1 summarizes the total number of discrete directions, total number of levels for each order of approximation and number of discrete directions on each level in one octant of a unit sphere for one- and multi-dimensional problems. When a discrete number of directions is used to approximate a continuous angular variation, ray effect is unavoidable [50]. The increase in the number of discrete directions would alleviate the ray effect, however, at the expense of additional computational time and memory requirement.

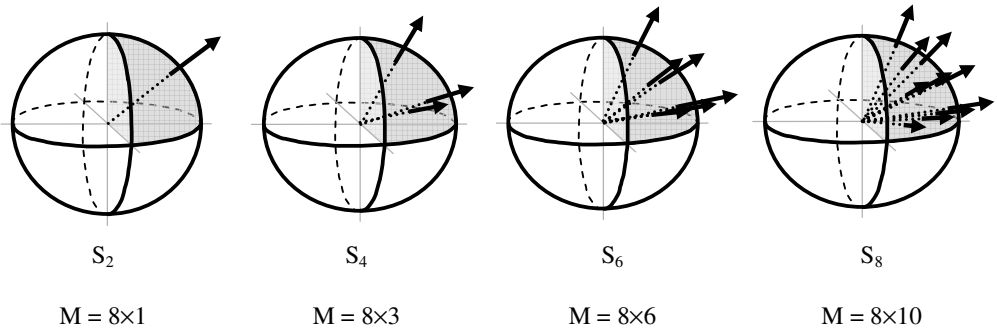

Figure 2.3 Orders of approximation

The angular quadrature scheme defines the specifications of ordinates Ω_m (μ_m, ς_m, ξ_m) and corresponding weights w_m used for the solution of RTE. The choice of quadrature scheme is arbitrary although restrictions on the directions and weights arise from the need to preserve symmetries and invariance properties of the physical system. Completely symmetric angular quadrature schemes, which mean symmetry of the point and surface about the center of the unit sphere, also about every

Table 2.1 Total number of discrete directions specified by order of approximation

Order of approximation	1-D $M = N$	3-D $M = 2^D N (N+2)/8$	Number of levels (= N/2)	Number of points at i^{th} level (= N/2 – i +1)
S_2	2	8	1	2-I
S_4	4	24	2	3-I
S_6	6	48	3	4-I
S_8	8	80	4	5-I

coordinate axis as well as every plane containing two coordinate axes, are preferred because of their generality and to avoid directional biasing solutions. Therefore, the description of the points in one octant is sufficient to describe the points in all octants. The quadrature sets are constructed to satisfy the key moments of the RTE and its boundary conditions. The quadrature schemes satisfy zeroth ($\sum_{m=1}^{M} w_m = 4\pi$), first ($\sum_{m=1}^{M} \zeta_m w_m = 0$) and second ($\sum_{m=1}^{M} \zeta_m^2 w_m = \frac{4\pi}{3}$) moments that correspond to incident energy, heat flux and diffusion condition, respectively in addition to higher moments.

The most frequently used angular quadrature scheme is S_N, originally developed by Carlson and Lathrop [46] and extended to higher order of approximations by Fiveland [51] and El Wakil and Sacadura [52]. Therefore, in this study MOL solution of DOM calculations will be based on S_N angular quadrature scheme. The quadrature ordinates and weights for axisymmetric cylindrical geometry of S_N approximations are listed in Appendix A.

Second parameter affecting the accuracy of MOL solution of DOM is the spatial discretization technique. The spatial discretization schemes used in this study are two-, and three-point upwind finite difference schemes [48, 53]. The reason behind the choice of upwind schemes is as follows: After the implementation of false-transients approach discrete ordinates equations take the form of first-order hyperbolic PDEs and for which it was demonstrated that upwind schemes eliminate the numerical oscillations caused by central differencing, as the direction of propagation of the dependent variables are taken into account in upwind schemes [48, 53]. The formulation and order of accuracy of the selected schemes are presented in Table 2.2.

Table 2.2 Spatial differencing schemes [48, 53]

Name of the scheme	Stencil	Formulation, $dI(\lambda I)/d\lambda \approx$	Order of accuracy
2-point upwind (DSS012)	○—●	$(I_i - I_{i-1}) / \Delta\lambda$	$O(\Delta\lambda)$
3-point upwind (DSS014)	○—○—●	$(3I_i - 4I_{i-1} + I_{i-2}) / 2\Delta\lambda$	$O(\Delta\lambda^2)$

The third factor affecting accuracy of MOL solution of DOM is the ODE integrator. In this thesis study ODE solver utilized is ROWMAP which is based on the ROW-methods of order 4 and uses Krylov techniques for the solution of linear systems. By a special multiple Arnoldi process the order of the basic method is preserved with small Krylov dimensions. Step size control is done by embedding with a method of order 6. Detailed description of ROWMAP can be found elsewhere [54].

2.4 Structure and Operation of the Computer Code

Figure 2.4 and Figure 2.5 show the flow diagram of the computer code Method of Lines Solution of Discrete Ordinates Method for spectral RTE (SMOLS4RTE) for absorbing-emmiting nongray medium in cylindrical coordinates. The absorption coefficient of the medium is calculated using either the PROPERTY_SLW or PROPERTY_WBCK subroutines from species concentration and temperature profiles. The general steps of the computer code are as follows:

1. Define the subdivision of the enclosure, order of approximation, spatial differencing scheme, number of gray gases and number of equations in the system of ODEs.
2. Declare 5-D arrays to store intensities, position derivatives, and time derivatives at each ordinate of each grid point for each gray gas. The 5-D arrays are of

dimensions [NG×NR×NZ×ND×NM] where NG is the number of gray gases considered in the calculation, NR and NZ are the number of nodes along r and z-axes respectively, ND stands for number of octants (ND = 2 for a one-dimensioanl problem, ND = 4 for a two-dimensioanl problem) and NM is the number of ordinates specifed by order of angular quadrature.

3. Read in input data specifying the physics of the problem which are, the dimensions of the enclosure, wall temperatures and emissivities, and temperature and concentration profiels of the medium.
4. Read in input data related with the ODE integrator which are the initial time, final time, print interval and the error tolerance.
5. Specify the direction cosines and corresponding weights.
6. Set the initial conditions required for the ODE integrator.
7. Initialize the intensities at all ordinates at all grid points for all gray gases.
8. Calculate absorption coefficients and associated weights at each grid point in the medium for each gray gas using either PROPERTY_SLW or PROPERTY_WBCK subroutines.
9. Set boundary conditions for the intensities leaving the boundary surfaces by using Eqs. (2.24-2.26 and 2.28).

<u>Calculation of the Approximations for the Spatial Derivatives</u>

10. Specify a gray gas, an octant, and an ordinate.
11. Specify a discrete location at the r direction.
12. Store the values of the intensities (at this direction and location for this gray gas) along r-axis in a 1-D array.
13. Call for spatial discretization subroutine which accepts the 1-D array of intensities as an input and computes the derivative with respect to r-axis as an output over the grid of NR points.
14. Transfer the 1-D array of spatial derivatives into the 5-D array of r-derivatives.

15. Repeat steps 10-15 for all discrete locations at r direction, all ordinates and all octants for all gray gases.
16. Repeat steps 10-16 for derivative terms with respect to z-axes, forming 1-D arrays along z-axes.

Calculation of the Time Derivatives

17. Calculate the intensities at the edges of angular range by using Eq. (2.22) for each directions and gray gases at each node.
18. Calculate the time derivative of intensity at each node for each ordinate of each octant for each gray gas using Eq. (2.31) to form a 5-D array of time derivatives.
19. Transform the 5-D arrays of intensities and time derivatives into 1-D arrays to be sent to the ODE solver.

Integration of the system of ODEs

20. Call the ODE solver subroutine to integrate the system of ODEs by using a time adaptive method. The ODE propogates in time by solving for the intensities at a time step j, calculating the time derivatives by performing steps 9 to 19 and integrating again to solve for intensities at the new time step j+1.
21. Return to the main program at prespecified time intervals.
22. Check if ODE integration has proceeded satisfactorily, print an error message if an error condition exists.
23. Transfer the solution at current print point from the 1-D array to a 5-D array.
24. Set the boundary conditions at current time step.
25. Print solution.
26. Check for convergence by comparing the solutions at current time step with those at previous three time steps. If current solution is within the specified range of the previous solutions, convergence is established go to step 30.

27. If convergence is not established, save the solution for convergence check.
28. Check the end of run time if final time is not reached go back to step 10.
29. If convergence is established or final time is reached, calculate the parameters of interest such as radiative heat flux and source terms.
30. Print output.
31. Stop.

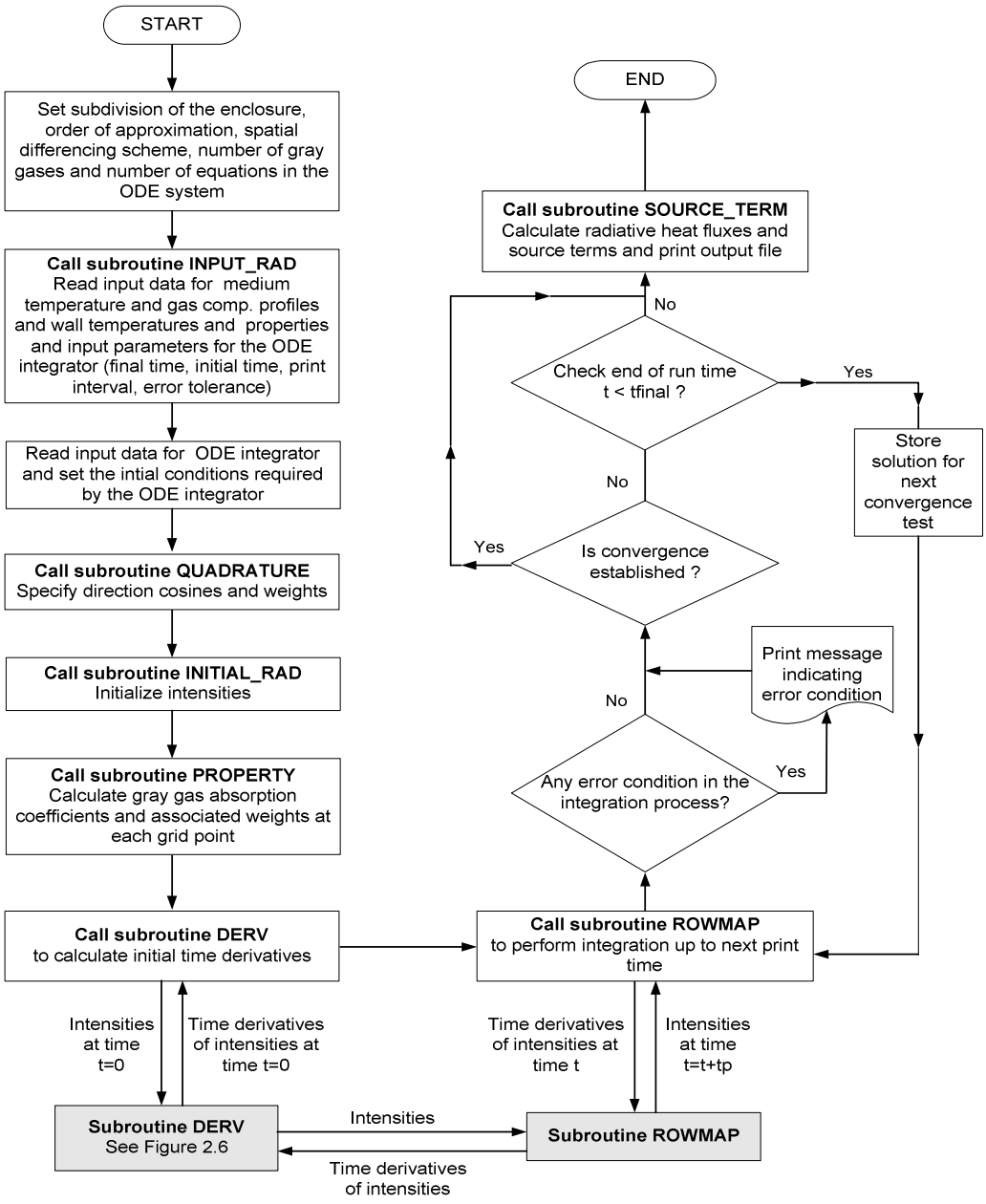

Figure 2.4 Flowchart for MOLS4RTE

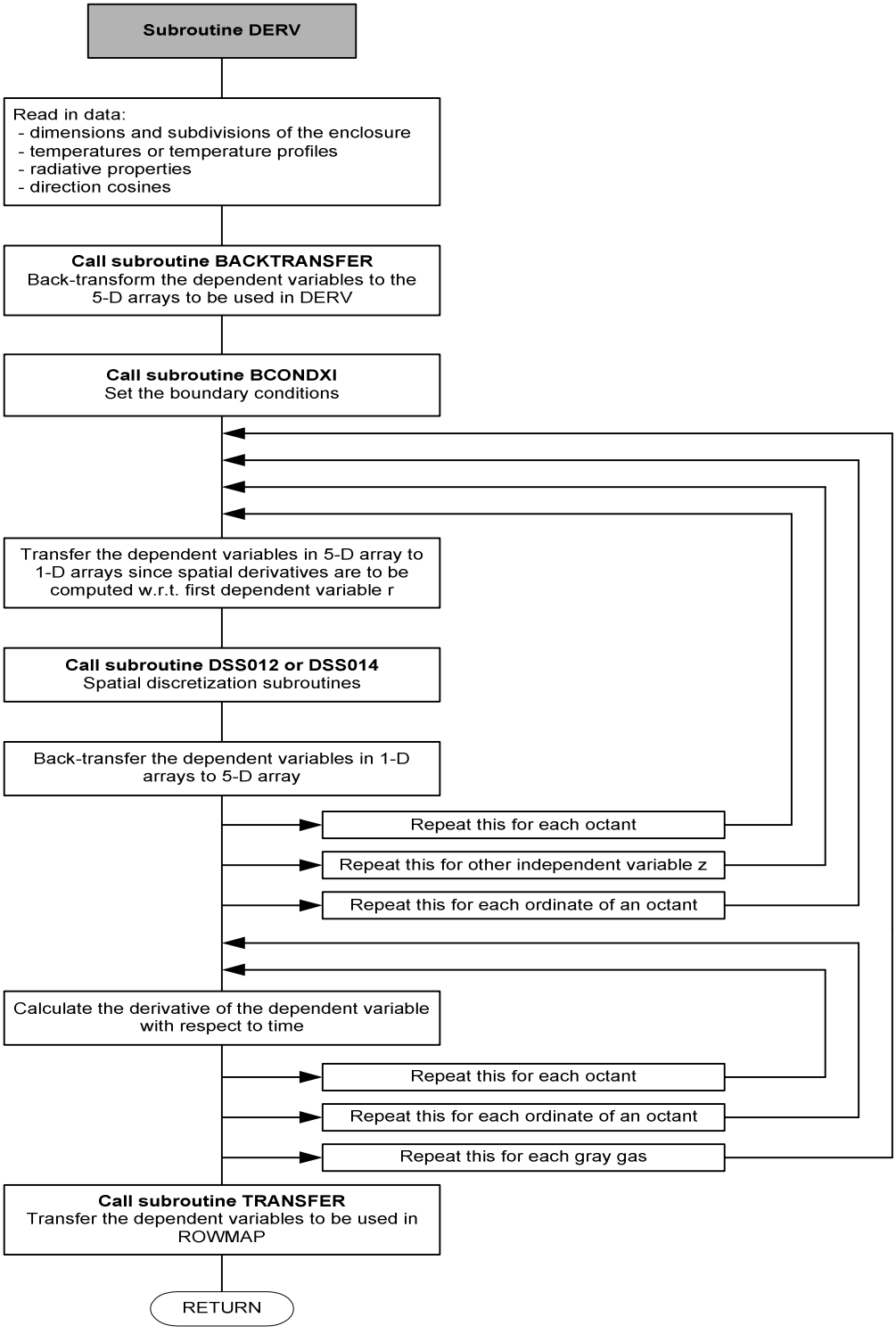

Figure 2.5 Algorithm of the subroutine DERV

CHAPTER 3

ESTIMATION OF RADIATIVE PROPERTIES

Accurate determination of radiative transfer necessitates both accurate solution of the RTE and reliable evaluation of the medium radiative properties. In the preceding chapter, MOL solution of DOM as an accurate and efficient technique for the solution of RTE has been explained. In this chapter, the gas radiative property models utilized in the present study will be described.

3.1 Gas Radiative Property Models

The most fundamental radiative property of participating gases is the absorption coefficient or the absorption cross-section when the absorption coefficient is normalized by the molar density [41]. The variation of absorption coefficient or absorption cross-section of a gas with wave number is called a spectrum, and it consists of millions of spectral lines, which are produced by the vibrational-rotational transitions in molecular energy levels. Figure 3.1 illustrates a high resolution portion of the H_2O spectrum generated at 1200 K and 1 atm total pressure by using HITRAN database [40, 41]. As can be clearly seen from the figure, absorption coefficient has a strong dependence on wave number. Because of this fact, numerical simulation of radiative heat transfer is a formidable task. A number of models with varying degrees of complexity and accuracy has been developed so far for the estimation of the radiative properties. These models can be classified into two main groups, namely gray and nongray gas radiative property models.

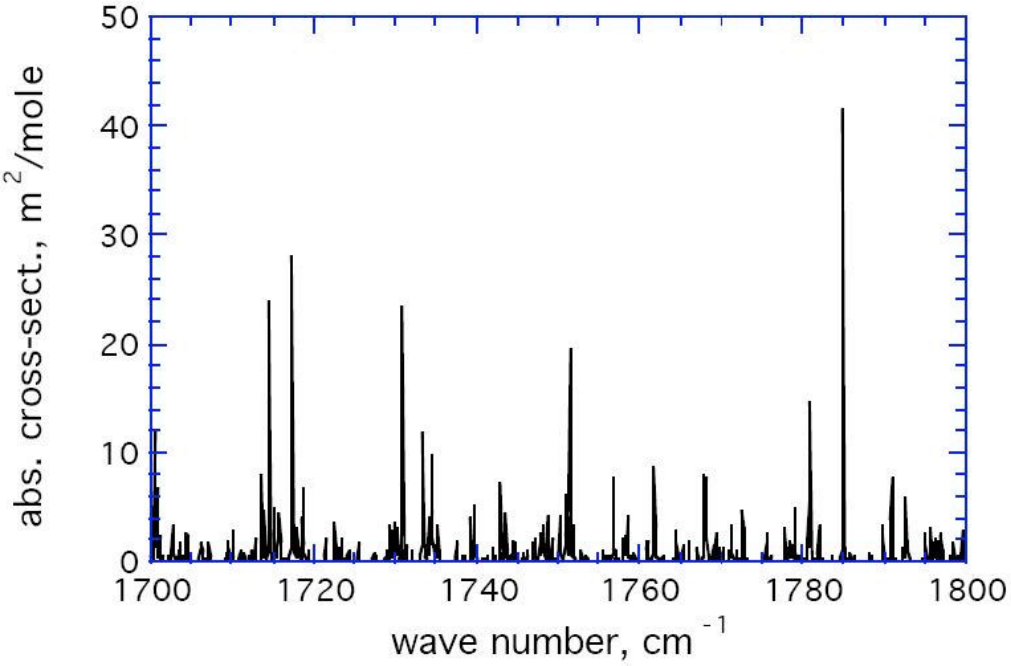

Figure 3.1 High resolution portion of the H_2O spectrum generated at 1200 K and 1 atm [41]

Gray gas model, which is the crudest approach, assumes that radiative property is independent of wave number. Nongray models, on the other hand, take into account this dependence. In the present study, two nongray gas radiative property models; SLW and WBCK models, as well as gray gas model, were used. The details of these models will be described in the following subsections.

3.1.1 Gray Gas Model

Gray gas model is an approximation, which assumes complete independence of radiative properties on wave number. Hence, in this model a single value of the absorption coefficient is used to represent the whole spectrum. Although this approach highly simplifies the RTE and its solution, it may bring about unpredictable errors [42]. However, there are many practical problems where the gray gas model

produces acceptable predictions [13, 16, 55].

In this model, the mean absorption coefficient of the medium is calculated from the expression given below

$$\kappa = -\frac{1}{L_m}\ln(1-\varepsilon_g) \tag{3.1}$$

where κ is the absorption coefficient and L_m is the mean beam length based on the whole enclosure. ε_g is the total emissivity estimated by Leckner's correlations [56] .

3.1.2 Spectral Line-Based Weighted Sum of Gray Gases (SLW) Model

As previously mentioned, the spectrum consists of millions of spectral lines. The approach of dividing the spectrum into small wave number intervals consisting of a sufficient number of spectral lines and solving the RTE for each of these intervals is computationally very intensive. However, approximately the same value of the absorption cross-sections is observed in many wave number intervals. All these wave number intervals having an absorption cross-section within a certain range delineated by two consecutive supplemental absorption cross-sections, $\tilde{C}_{abs,j}$, can be combined in groups and treated as separate gray gases with constant absorption cross-sections, $C_{abs,j}$. Figure 3.2 schematically illustrates how the real spectrum can be approximated by grouping into 4 gray gases. This idea of replacing a nongray (real) gas by a set of gray gases forms the basis of WSGG model which was first introduced by Hottel and Sarofim [31] for the approximation of gas total emissivity;

$$\varepsilon = \sum_j a_j (1 - e^{-C_{abs,j} N L}) \tag{3.2}$$

where $C_{abs,j}$ is the discrete gray gas absorption cross-section, N is the molar density, L is the path length and a_j is the associated gray gas weight. The gray gas weights can be physically interpreted as the fraction of the blackbody energy in the spectral regions where the absorption cross-section is $C_{abs,j}$ [31]. Smith *et al.*[32], determined the weights and absorption coefficients for water vapor and carbon dioxide as well as

for the mixture of both gases by minimizing the error between total emissivities and the emissivity given by Eq. (3.2)

Modest [33] extended the applicability of WSGG model to any RTE solution technique by substituting the WSGG expression for the absorptivity into the RTE integrated along a line of sight. This derivation yielded the so-called WSGG RTE (Eq. (2.11)). Modest's derivation requires that the gray gas absorption coefficients are constant along the line of sight and that the boundaries are black. Later, Denison and Webb [35] derived WSGG RTE by a discontinuous integration over a model histogram spectrum consisting of relatively few discrete values of absorption cross-section. This derivation demonstrated that the use of this form of RTE does not require spatially constant absorption coefficients and weights and it is not limited to black boundaries.

Denison and Webb [36, 39], further improved the WSGG approach by introducing an absorption-line blackbody distribution function which incorporates the local value of the blackbody distribution function together with the local absorption cross-section.

The procedure of the SLW model consists of two main stages;

i) calculation of absorption coefficients

ii) calculation of gray gas weights

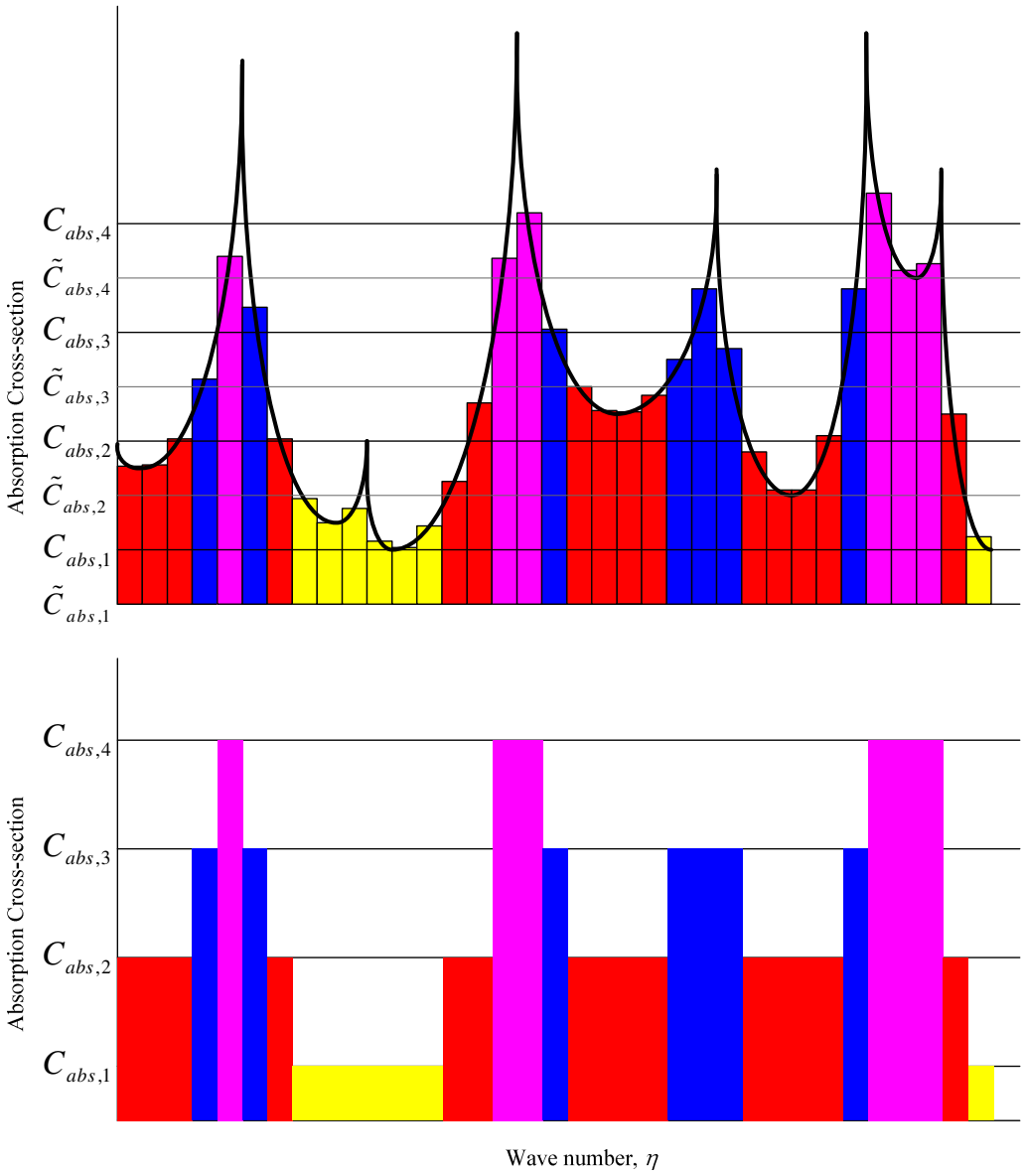

Figure 3.2 Approximation of a real spectrum by grouping into 4 gray gases [41]

3.1.2.1 Calculation of Absorption Coefficients

The primary variable used in the calculation of absorption coefficients is absorption cross-section, which is defined as the ratio absorption coefficient to the molar density, *N*. In order to calculate the absorption coefficients, first, a set of

logarithmically spaced absorption cross-sections are selected to span the whole range found in practical problems. In this study, 10, 15 and 20 absorption cross-sections logarithmically spaced between 3×10^{-5} and 60 m^2/mol for water vapor and 3×10^{-5} and 120 m^2/mol for carbon dioxide were utilized following the recommendations of Denison [41]. These logarithmically spaced absorption cross-sections are called supplemental absorption cross-sections, $\tilde{C}_{abs,j}$ as they are used to determine the blackbody weights, a_j but do not appear directly in the corresponding gray gas absorption coefficient calculation. Each of the spaces between two consecutive supplemental absorption cross sections, $\tilde{C}_{abs,j}$ and $\tilde{C}_{abs,j+1}$, is considered as a separate gray gas associated with a constant absorption cross- section calculated from the following relation;

$$C_{abs,j} = \exp\left[\frac{\ln(\tilde{C}_{abs,j}) + \ln(\tilde{C}_{abs,j+1})}{2}\right] \tag{3.3}$$

Once the absorption cross-sections for each gray are obtained, local absorption coefficients of each gray gas are calculated from;

$$\kappa_j = N \cdot C_{abs,j} \tag{3.4}$$

where molar density, *N,* is evaluated from any equation of state with local values of temperature and composition. In the present study, ideal gas equation of state was used. One gray gas is associated with zero absorption coefficient and utilized to account for the transparent regions and it is called a "transparent gas".

3.1.2.2 Calculation of Blackbody Weights

The absorption-line blackbody distribution function, F_s, which provides an efficient correlation for evaluation of blackbody weights, a_j is defined as the fraction of the blackbody energy, $E_{b,\eta}$, in the portion of the spectrum where the high-resolution spectral absorption cross-section of the gas $C_{abs,\eta}$ is less than the prescribed value C_{abs} , as illustrated in Figure 3.3 for a few absorption lines at high resolution.

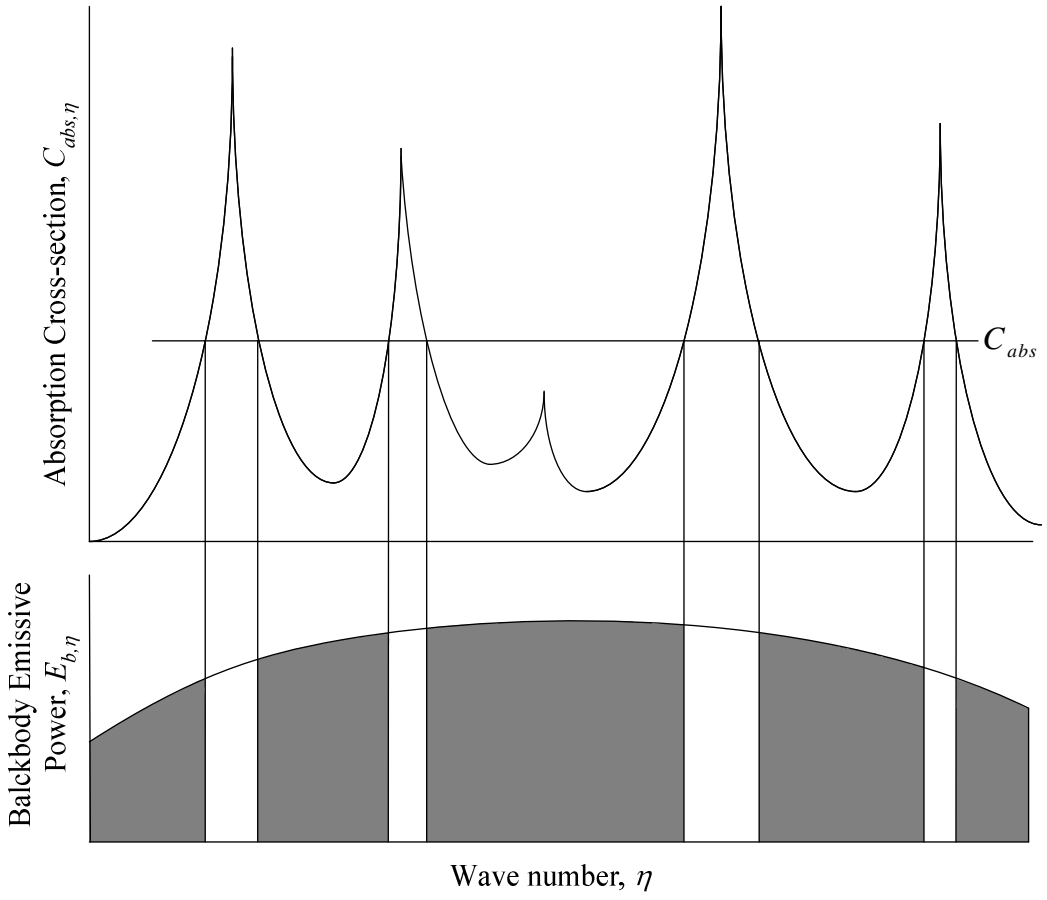

Figure 3.3 Portions of the spectrum, for a few representative absorption lines, where fraction of blackbody energy is calculated [41]

The portions of the spectrum over which Planck's function is integrated are represented by the shaded segments in the figure. The distribution function for species *s* is then expressed as,

$$F_s(C_{abs},T_b,T_g,P_T,Y_s)=\frac{1}{\sigma T_b^4}\sum_i\int_{\Delta\eta_i(C_{abs},T_b,T_g,P_T,Y_s)}E_{b,\eta}(\eta,T_b)d\eta \tag{3.5}$$

where $E_{b,\eta}$ is Planck's function evaluated at the wave number, η and blackbody temperature, T_b. The subscript *i* refers to the i^{th} spectral segment and summation is performed over all segments covering the entire spectrum. The dependence of the

function on the spectrum is through the spectral integration of each segment $\Delta\eta_i$ which is dependent on the absorption cross-section, gas temperature T_g, total pressure P_T and species mole fraction Y_s [36].

The blackbody weights, a_j, are expressed as the fractions of the blackbody energy at local gas temperature in the spectral regions where the absorption cross-section is between $\tilde{C}_{abs,j}$ and $\tilde{C}_{abs,j+1}$, as shown by the shaded areas in Figure 3.4 and may be calculated as the difference between the absorption-line blackbody distribution functions evaluated at these two consecutive supplemental absorption cross-sections, and local gas temperature, T_g;

$$a_j = F_s(\tilde{C}_{abs,j+1}, T_b, T_g, Y_s) - F_s(\tilde{C}_{abs,j}, T_b, T_g, Y_s) \tag{3.6}$$

Denison and Webb [36, 39] provided simple mathematical correlations for the absorption-line blackbody distribution function, F_s , for H_2O and CO_2. For H_2O, the following hyperbolic equation is recommended;

$$F_w = \frac{1}{2}\tanh\left[P_w(T_g, T_b, \chi - \chi_{sb})\right] + \frac{1}{2} \tag{3.7}$$

where the function P_w is given as

$$P_w = \sum_{l=0}^{3}\sum_{m=0}^{3}\sum_{n=0}^{3} b_{lmn}\left(\frac{T_g}{2500}\right)^n \left(\frac{T_b}{2500}\right)^m (\chi - \chi_{sb})^l \tag{3.8}$$

and

$$\chi = \ln(C_{abs}) \tag{3.9}$$

χ_{sb} is introduced to account for the self-broadening;

$$\chi_{sb} = \sum_{l=0}^{3}\sum_{m=0}^{3}\sum_{n=0}^{2} c_{lmn}\left(\frac{T_b}{2500}\right)^n \chi^m (Y_w)^{l+1} \tag{3.10}$$

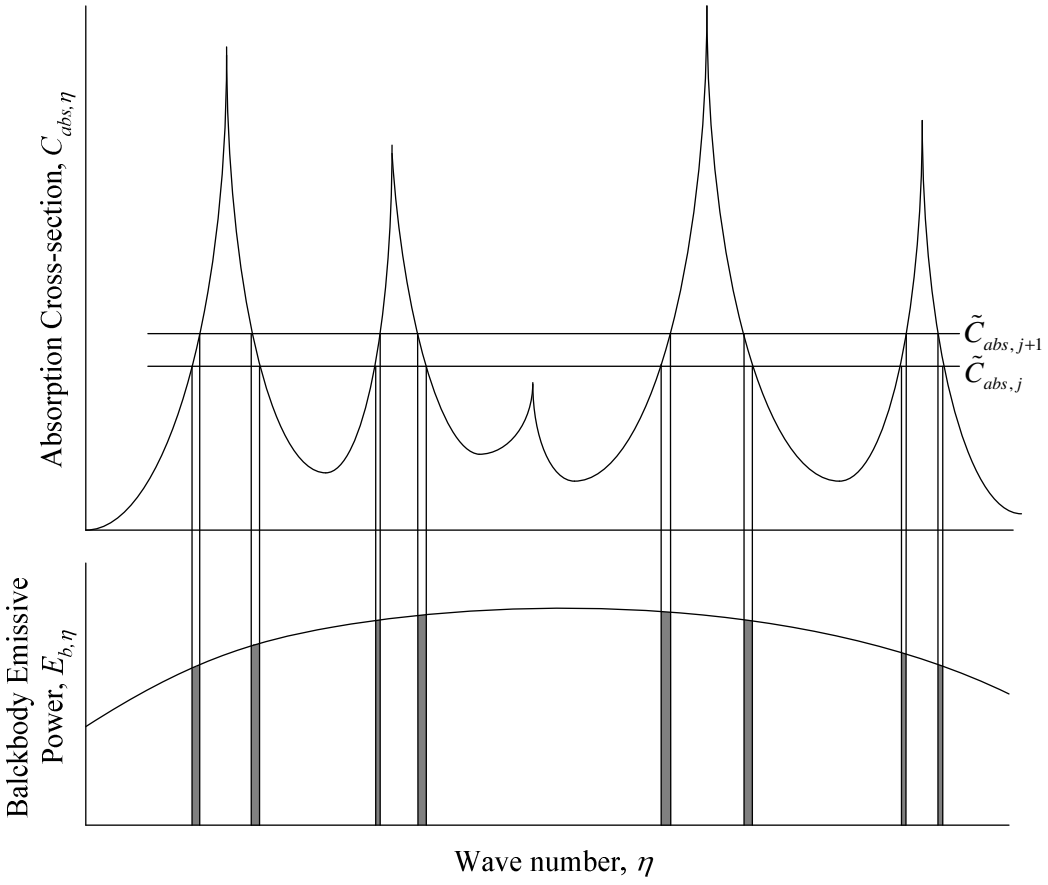

Figure 3.4 Portions of the spectrum, for a few representative absorption lines, where $C_{abs,\eta}$ is between $\tilde{C}_{abs,j}$ and $\tilde{C}_{abs,j+1}$ [41]

The coefficients of the correlation b_{lmn} and c_{lmn} are given in Table 3.1 and 3.2, respectively.

Table 3.1 The coefficients of b_{lmn} appearing in Eq. (3.8) for H_2O [41]

$l = 0$

m/n	0	1	2	3
0	1.6103	-4.0931	5.1435	-2.0857
1	-0.81812	15.5525	-21.819	9.8775
2	2.6001	-21.204	31.0828	-14.279
3	-1.3171	9.6524	-14.474	6.6747

$l = 1$

m/n	0	1	2	3
0	0.440187	-0.63348	0.871627	-0.38798
1	-0.82164	5.0239	-5.9818	2.6355
2	1.5149	-7.8032	9.8642	-4.1931
3	-0.81023	3.727	-4.874	1.9868

$l = 2$

m/n	0	1	2	3
0	0.106647	-0.43116	0.689598	-0.29831
1	-0.38573	1.8865	-2.9712	1.2834
2	0.578351	-2.6218	4.2698	-1.7929
3	-0.28014	1.1785	-1.9568	0.787249

$l = 3$

m/n	0	1	2	3
0	8.25027E-03	-3.28556E-02	6.81563E-02	-3.04815E-02
1	-3.10578E-02	0.123369	-0.26154	0.117452
2	4.39319E-02	-0.15792	0.350948	-0.15308
3	-2.03699E-02	6.61142E-02	-0.15283	6.34035E-02

Table 3.2 The coefficients of c_{lmn} appearing in Eq. (3.10) for H_2O [41]

$l = 0$

m/n	0	1	2
0	4.72	-8.5482	5.2394
1	-0.84969	0.312478	-0.13804
2	-3.47243E-02	4.02461E-02	-5.80104E-02
3	5.79830E-04	3.94125E-03	-5.29017E-03

$l = 1$

m/n	0	1	2
0	-8.9615	16.9547	-10.76
1	1.5861	-2.0166	1.46
2	4.34730E-02	-0.67133	0.633231
3	2.87067E-03	-7.06830E-02	6.23710E-02

$l = 2$

m/n	0	1	2
0	9.1461	-17.327	11.1864
1	-1.3975	1.9965	-1.6935
2	8.46419E-02	0.599994	-0.70054
3	7.14719E-03	6.62086E-02	-6.87294E-02

$l = 3$

m/n	0	1	2
0	-3.5504	6.624	-4.3058
1	0.485392	-0.7071	0.689109
2	-6.77456E-02	-0.18179	0.269308
3	-5.92726E-03	-2.04694E-02	2.56411E-02

For CO_2, the hyperbolic equation for the absorption-line blackbody distribution function (Eq. (3.9)) takes the following form;

$$F_c = \frac{1}{2}\tanh\left[P_c(T_g, T_b, \chi)\right] + \frac{1}{2} \tag{3.11}$$

where the function P_c is given as

$$P_c = \sum_{l=0}^{3}\sum_{m=0}^{3}\sum_{n=0}^{3} d_{lmn}\left(\frac{T_g}{2500}\right)^n\left(\frac{T_b}{2500}\right)^m \chi^l \tag{3.12}$$

χ is given by Eq.(3.7). The coefficients of the correlation d_{lmn} are given in Table 3.3.

Table 3.3 The coefficients of d_{lmn} appearing in Eq. (3.12) for CO_2 [41]

$l = 0$

m/n	0	1	2	3
0	2.45702	-5.45334	6.53751	-2.52344
1	-4.0232	15.67297	-24.3247	11.33757
2	7.54549	-23.8023	39.51896	-19.1137
3	-3.63104	11.9078	-20.3606	9.97877

$l = 1$

m/n	0	1	2	3
0	7.65678E-02	2.36184	-3.95061	2.17482
1	0.2901819	-12.0041	22.44342	-13.0467
2	-0.64282	21.5003	-40.8667	23.66762
3	0.3942158	-11.5818	22.05176	-12.6536

$l = 2$

m/n	0	1	2	3
0	-3.30582E-02	0.4367742	-0.725331	0.4138566
1	0.3672993	-3.52466	6.74885	-3.96295
2	-0.69811	6.60703	-12.9667	7.58713
3	0.3831158	-3.65683	7.19415	-4.16496

$l = 3$

m/n	0	1	2	3
0	-1.87927E-03	1.92123E-02	-3.25863E-02	1.98493E-02
1	2.85033E-02	-0.223537	0.4402715	-0.26267
2	-5.49594E-02	0.4370937	-0.881494	0.521958
3	3.04198E-02	-0.247793	0.4990777	-0.291566

3.1.2.3 Treatment of Non-Isothermal and Non-Homogeneous Media

The real spectrum has a complex dependence on temperature, pressure and mole fractions of the absorbing gases. In general, the gases become more absorbing with increasing temperature due to the growth of hot lines in their spectrum. Therefore, consideration of local variation of the absorption coefficient with temperature, pressure and composition is of great importance.

SLW model allows spatial dependence of the gray gas absorption cross-sections, $C_{abs,j}$, on temperature, pressure and species concentration. In order to do so, the high resolution absorption cross-section spectrum is idealized by expressing the spectral absorption cross-section as the product of two functions:

$$C_{abs,\eta}(\eta, T_g, P, Y_s) = \phi(T_g, P, Y_s)\,\psi(\eta) \tag{3.13}$$

where P is the total pressure and is taken as 1 atm. Hence, hereafter it will be excluded from the equations for the sake of brevity. It should be noted that the spectral dependence is defined only by the function, $\psi(\eta)$. This idealized behavior of the spectrum is illustrated in Figure 3.5, with a few high-resolution absorption lines at two separate temperatures and mole fractions. As can be seen from the figure, all the wave numbers, η, corresponding to the intersection points for a given value of the absorption cross-section remain unchanged regardless of temperature and mole fraction. Therefore, the spectrum only shifts upwards as the temperature and mole fraction increase from state 1 (T_{g1}, Y_{s1}) to state 2 (T_{g2}, Y_{s2}). Examination of Figure 3.5 also reveals that, the absorption-line blackbody distribution functions, demonstrated as the shaded area under the blackbody emissive power, $E_{b,\eta}$ curve, are identical for states 1 and 2. From these observations, the following equality was deduced [37];

$$F_s\left[C_{abs,j}(T_2, Y_{s2}); T_b = T_{ref}; T_g = T_2; Y_s = Y_{s2}\right] = F_s\left[C_{abs,j}(T_1, Y_{s1}); T_b = T_{ref}; T_g = T_1; Y_s = Y_{s1}\right] \tag{3.14}$$

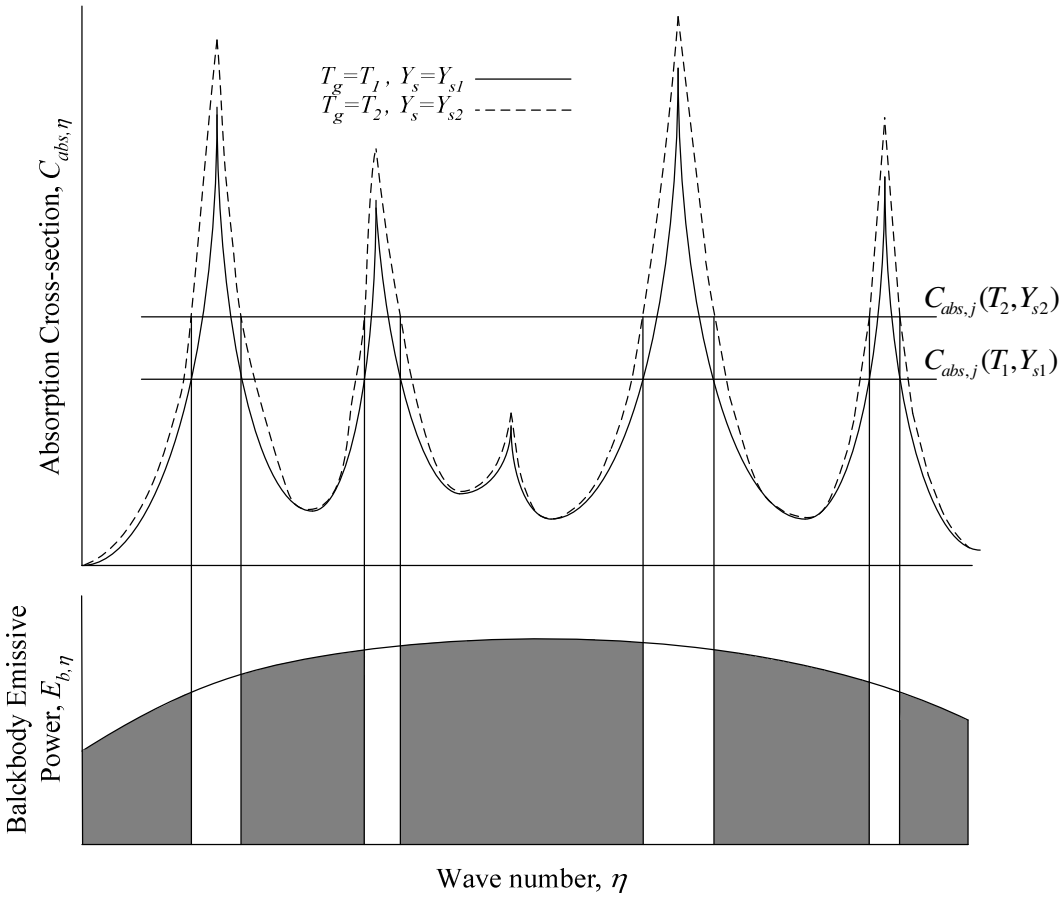

Figure 3.5 Idealized gas temperature dependence of high-resolution spectrum resulting in equivalent blackbody fractions [41]

which provides an implicit dependence of $C_{abs,j}$ on local gas state (temperature and mole fractions of the absorbing species). In practice, a reference state is selected as the spatial averages of temperature and mole fraction fields, and Eq.(3.14) is rewritten for equivalent absorption-line blackbody distribution function evaluated at the reference and local states;

$$F_s\left[C_{abs,j};T_b=T_{ref};T_g=T_{loc};Y_s=Y_{s,loc}\right]=F_s\left[C_{abs,j,ref};T_b=T_{ref};T_g=T_{ref};Y_s=Y_{s,ref}\right] \tag{3.15}$$

The reference absorption cross-sections, $C_{abs,j,ref}$, are the discrete values determined from Eq. (3.3). Then, the local values of $C_{abs,j}$ are determined from this implicit relation by using an iterative technique. In this study, bisection method was used.

The local absorption coefficients are then found as the product of the local molar density determined from ideal gas equation of state and the local gray gas absorption cross-section evaluated from Eq.(3.4):

$$\kappa_j = N(T_{loc}, P_T, Y_{s,loc}) C_{abs,j}(T_{loc}, P_T, Y_{s,loc}) \tag{3.16}$$

The blackbody weights of the gray gases are calculated as described in section 3.2.2.2 from the following relation;

$$a_j = F_s(\tilde{C}_{âbs,j+1}; T_b = T_{loc}; T_g = T_{ref}; Y_s = Y_{s,ref}) - F_s(\tilde{C}_{âbs,j}; T_b = T_{loc}; T_g = T_{ref}; Y_s = Y_{s,ref}) \tag{3.17}$$

where T_{loc}, is the local value of the temperature and T_{ref} and $Y_{s,ref}$ are the reference values of the temperature and mole fraction, respectively.

3.1.2.4 Treatment of Binary Gas Mixtures

In order to calculate, total heat transfer rates in a mixture of two gases, H_2O and CO_2, the WSGG form of RTE [Eq. (2.11)] is modified by including an additional gray gas index, *k*, to account for the second specie [37];

$$\frac{dI_{j,k}}{ds} = \kappa_{j,k}\left(a_{j,k} I_b - I_{j,k}\right) \tag{3.18}$$

The joint gray gas weights, $a_{j,k}$ are defined as the fraction of blackbody energy in the high resolution spectrum where the effective absorption cross-sections of H_2O and CO_2 are $C_{abs,w,j}$ and $C_{abs,c,k}$, respectively (see Figure 3.6). The indices *j* and *k* denote the j^{th} and k^{th} gray gas for H_2O and CO_2, respectively. Including the spectral windows, these joint gray gas weights sum to unity:

$$\sum_j \sum_k a_{j,k} = 1 \tag{3.19}$$

It has been shown by Denison and Webb [37] that the joint gray gas weights are well approximated by the product of two individual weights as defined in Eq. (3.1)

$$a_{j,k} = a_j \cdot a_k \tag{3.20}$$

The absorption coefficients $\kappa_{j,k}$ are given as the sum of contributions of the two species:

$$\kappa_{j,k} = N_w C_{abs,w,j} + N_c C_{abs,c,k} \tag{3.21}$$

where N_w and N_c are the molar densities of H_2O and CO_2, respectively.

In the case of non-isothermal and non-homogeneous media, local supplemental absorption coefficients and gray gas weights are calculated separately for each participating gas (H_2O and CO_2) and the mixture absorption coefficient and the corresponding weights are determined through Eqs. (3.20) and (3.21), respectively.

Once the gray gas absorption coefficients and weights are calculated, they are substituted into the WSGG RTE and radiative heat transfer calculations are performed for each gray gas.

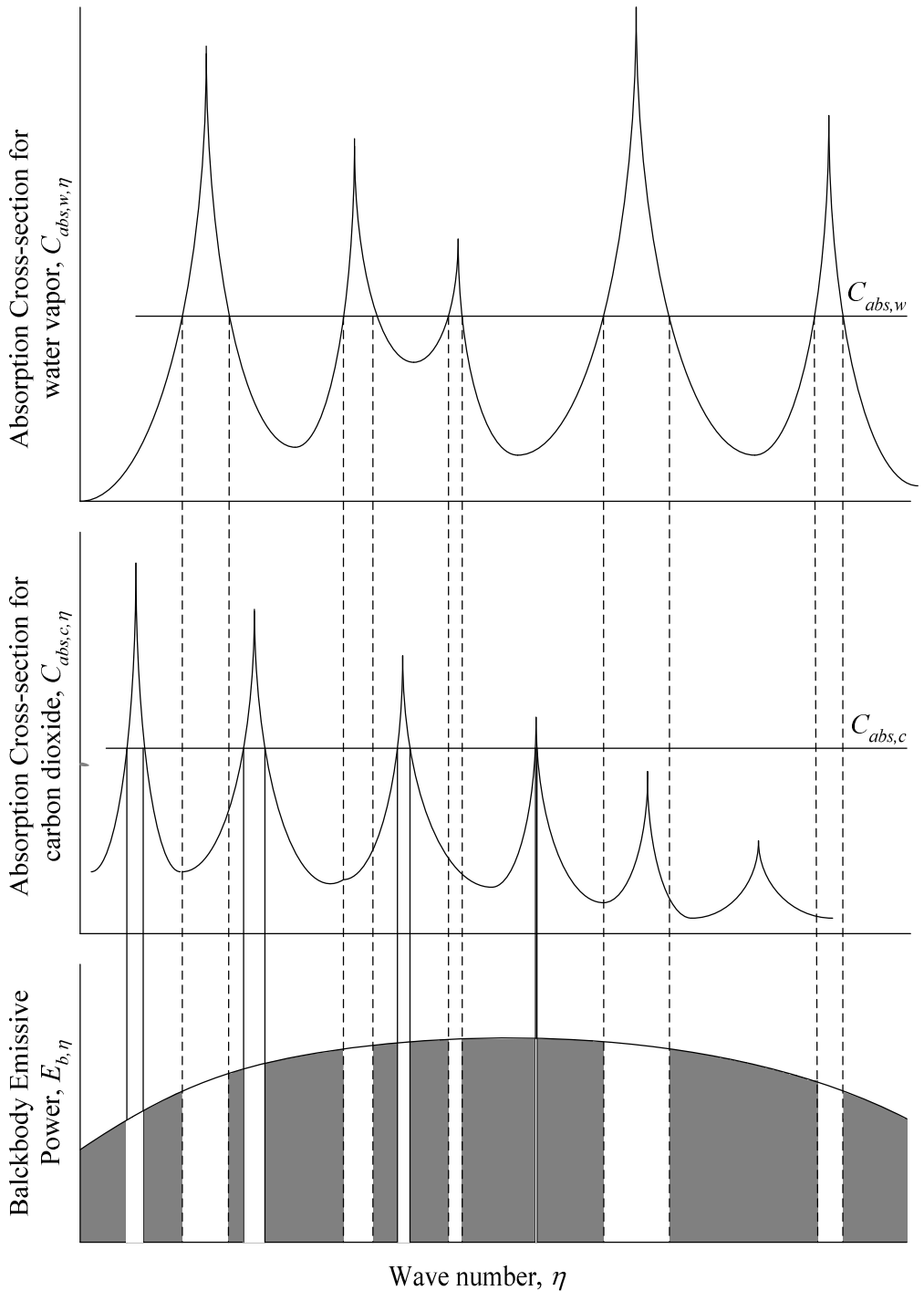

Figure 3.6. Portions of the spectrum where the absorption-line blackbody distribution function for H_2O-CO_2 mixture is calculated [41]

3.1.3 Wide Band Correlated-*k* (WBCK) Model

Absorption and emission of radiation from gases is concentrated only in certain regions of the spectrum, which are called vibration-rotation bands. Inside each band, the spectral absorption coefficient, κ_η , varies arbitrarily with the wave number, η. For demonstration, a particularly simple distribution of the spectral absorption coefficient, κ_η over a vibration-rotation band is shown in Figure 3.7(a)

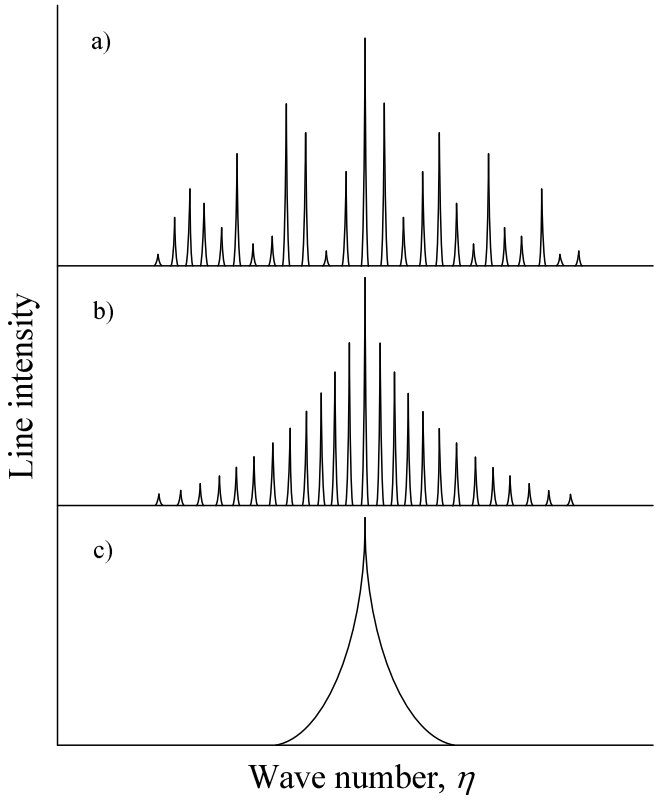

Figure 3.7. Simple representation of a typical vibration rotation band,
a) realistic, b) exponential, c) re-ordered [57]

Wide band models (WBM) treat entire vibrational-rotational band as a whole, which makes it possible to replace the actual absorption coefficient with an averaged value over a wide band. The most frequently used wide band model is the exponential wide band model (EWBM) developed by Edwards and his co-workers [22, 58].In this model, the detailed knowledge of the position, shape and intensity of the spectral lines constructing the wide bands are considered to be unimportant,

instead the band shape is approximated by an exponential function, as illustrated in Figure 3.7 (a) and (b).

The radiative properties are obtained by specifying three model parameters, namely band strength parameter, α, line overlap parameter, β and band width parameter, ω that characterize a given wide band. Figure 3.8 shows physical meaning of these parameters.

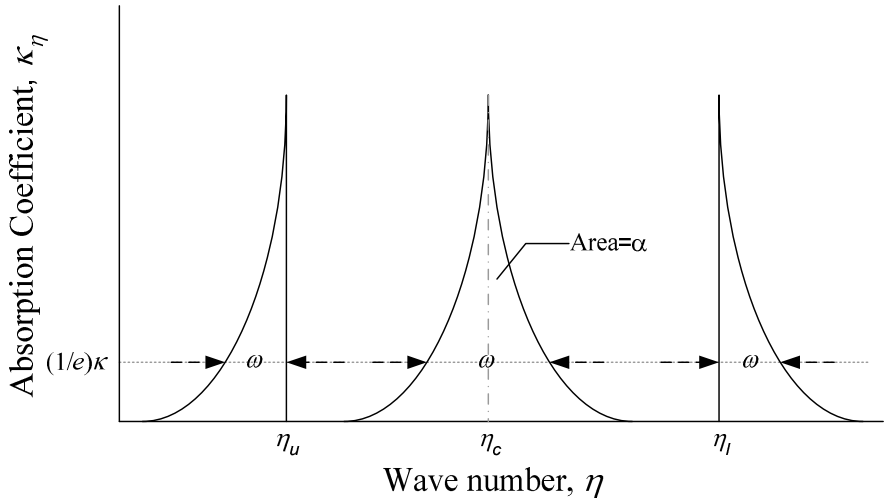

Figure 3.8 Band shapes for EWBM

As can be seen from the figure, α is associated with the area under the wide bands and ω is the width of the band at 1/*e* of the maximum value of the absorption coefficient. A detailed description and empirical correlations from which these parameters are calculated are given in Appendix B.

The radiative properties, in EWBM, are expressed as wide band absorptances, *A*, which are approximated by the so-called four-region expression;

$$A^* = \begin{cases} \tau_0 & \text{for } \tau_0 \le 1 \text{ and } \tau_0 \le \beta \\ (4\beta\tau_0)^{1/2} - \beta & \text{for } \beta \le \tau_0 \le 1/\beta \text{ and } \beta \le 1 \\ \ln(\tau_0\beta) + 2 - \beta & \text{for } 1/\beta \le \tau_0 \le \infty \text{ and } \beta \le 1 \\ \ln(\tau_0) + 1 & \text{for } \tau_0 \ge 1 \text{ and } \beta \ge 1 \end{cases} \tag{3.22}$$

where $A^{*}=A/\omega$ is the dimensionless band absorption and τ_0 is the optical thickness at the band head. The transmittance τ_k for each the wide band is assumed to be constant and calculated from;

$$\tau_k = \left(\frac{\tau_0}{A}\right)\left(\frac{dA}{d\tau_0}\right) \tag{3.23}$$

One drawback of EWBM is the need to determine a pathlength to evaluate the absorption coefficient from Beer's law;

$$\kappa_k = -\frac{1}{L_m}\ln(\tau_k) \tag{3.24}$$

If a beam length is approximated, errors are introduced into the solution [41]. Therefore, recently, there has been increased attention in the development of nongray gas radiative property models, which yield absorption coefficient and hence allow the use of arbitrary solution methods of the RTE written in terms of absorption coefficient. More recently, the *k*-distribution method has been extended to wide bands [27, 28, 30] and a new hybrid method WBCK was developed.

WBCK model is based on re-ordering the wave numbers within the wide bands to yield a smooth, monotonic decreasing function, which makes it possible to introduce a discretized set of absorption coefficients, each representing a gray gas that can easily be applied to the WSGG RTE (Eq. (2.11). The procedure of the WBCK model consists of three stages;

i) calculation of absorption coefficients

ii) calculation of wave numbers within the limits of wide bands

iii) calculation of gray gas weights

3.2.3.1 Calculation of Absorption Coefficients

The gray gas absorption coefficients are calculated as in SLW model for which the detailed explanation is given in section 3.1.2.2 For the sake of brevity, the procedure will not be repeated here.

3.2.3.2 Calculation of Wave Numbers

In order to calculate the wave numbers within a wide band, Denison and Fiveland [29] have proposed the following correlation by a fit to the four-region expression for wide band absorptance, *A* given in Eq. (3.22).

$$\xi^*(\kappa^*) = \sum_{i=1}^{n_p} C_{i,1} E_1(p_i \kappa^*) + C_{1,2} \frac{e^{-p_1 \kappa^*}}{p_1} \tag{3.25}$$

where dimensionless re-ordered wave number ξ^*, dimensionless absorption coefficient, κ^* and exponential integral function of order 1, E_1 are defined in Equations (3.26), (3.27) and (3.28), respectively.

$$\xi^* = \frac{\xi}{\omega} \tag{3.26}$$

$$\kappa^* = \frac{\kappa}{\rho\alpha/\omega} = \frac{\tilde{C}_{abs}}{M_w \alpha/\omega} \tag{3.27}$$

$$E_1(p_i \kappa^*) = \int_1^\infty e^{-p_i \kappa^* t} \frac{dt}{t} \tag{3.28}$$

In Eq. (3.26), ρ and M_w are the density and molecular weight of the absorbing gas, respectively. The coefficients $C_{i,j}$, poles p_i and n_p appearing in Eq.(3.25) are given as functions of line-overlap parameter β and tabulated in Table 3.4. The exponential wide band model parameters, α, β and ω are evaluated for each wide band at the average temperature and mole fraction of the medium. Then by making use of these model parameters, a single spectrum representing the entire domain will be constructed.

Once the re-ordered wave numbers, ξ_j , are evaluated from Eq.(3.25), the wave numbers, η , are calculated from the following equation depending on whether the band head is situated in the center, lower limit or upper limit of the band (see Figure 3.9);

$$\eta(\kappa) = \begin{cases} \eta_l + \xi_j(\kappa) & \text{(lower limit)} \\ \eta_c \pm \xi_j(\kappa)/2 & \text{(centre)} \\ \eta_u - \xi_j(\kappa) & \text{(upper limit)} \end{cases} \tag{3.29}$$

Table 3.4 Poles, p_i, and coefficients, $C_{i,j}$ [29]

	$0.001 < \beta \leq 0.0202256$	$0.0202256 < \beta < 0.2003$	$0.2003 \leq \beta \leq 1$
n_p	3	2	1
p_1	$6.78622E\text{-}4 + 3.61937\beta - 30.2514\beta^2 + 2181.40\beta^3$	$7.27821E\text{-}2 - 1.39993\beta + 104.659\beta^2 - 996.743\beta^3 + 3117.65\beta^4$	$1 + 2.864\sqrt{1 - \frac{(1-\beta)^4}{0.408986}}$
p_2	$1/p_1$	$1/p_1$	-
p_3	1	-	-
$C_{1,1}$	$p_1 C_{2,1}$	$(p_1^2 - p_1)/(p_1^2 - 1)$	1
$C_{2,1}$	$0.952246 - 12.9573\beta + 877.601\beta^2 - 14851.1\beta^3$	$(p_1 - 1)/(p_1^2 - 1)$	-
$C_{3,1}$	$1 - C_{1,1} - C_{2,1}$	-	-
$C_{1,2}$	0	0	$p_1^2 - p_1$

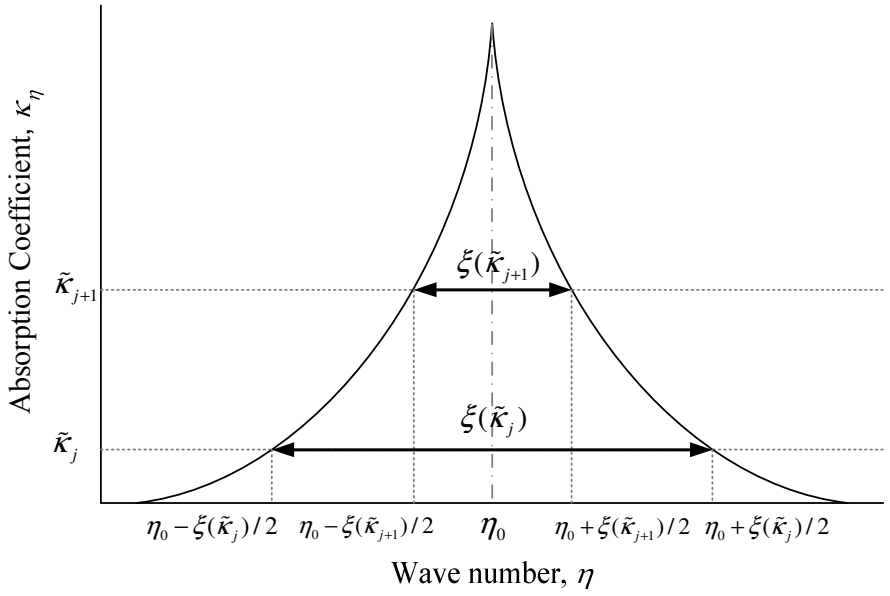

Figure 3.9 Discretization of representative re-ordered band

According to the magnitude of these wave numbers, the total spectrum is subdivided by the wave number limits, η_i, for all bands and gray gases, as shown in Figure 3.10. For each wave number interval, $\Delta\eta_i$, defined as the difference of two consecutive wave number limits η_i and η_{i+1}, the actual absorption coefficient is calculated as the sum of all gray gas absorption coefficients, κ_j , for all overlapping bands:

$$\kappa_{act}(\Delta\eta) = \sum_{k=1}^{\substack{Number\ of \\ overlapping \\ bands}} \kappa_j(\Delta\eta, k) \tag{3.30}$$

These actual absorption coefficients are used only for the calculation of the blackbody weights of the gray gases.

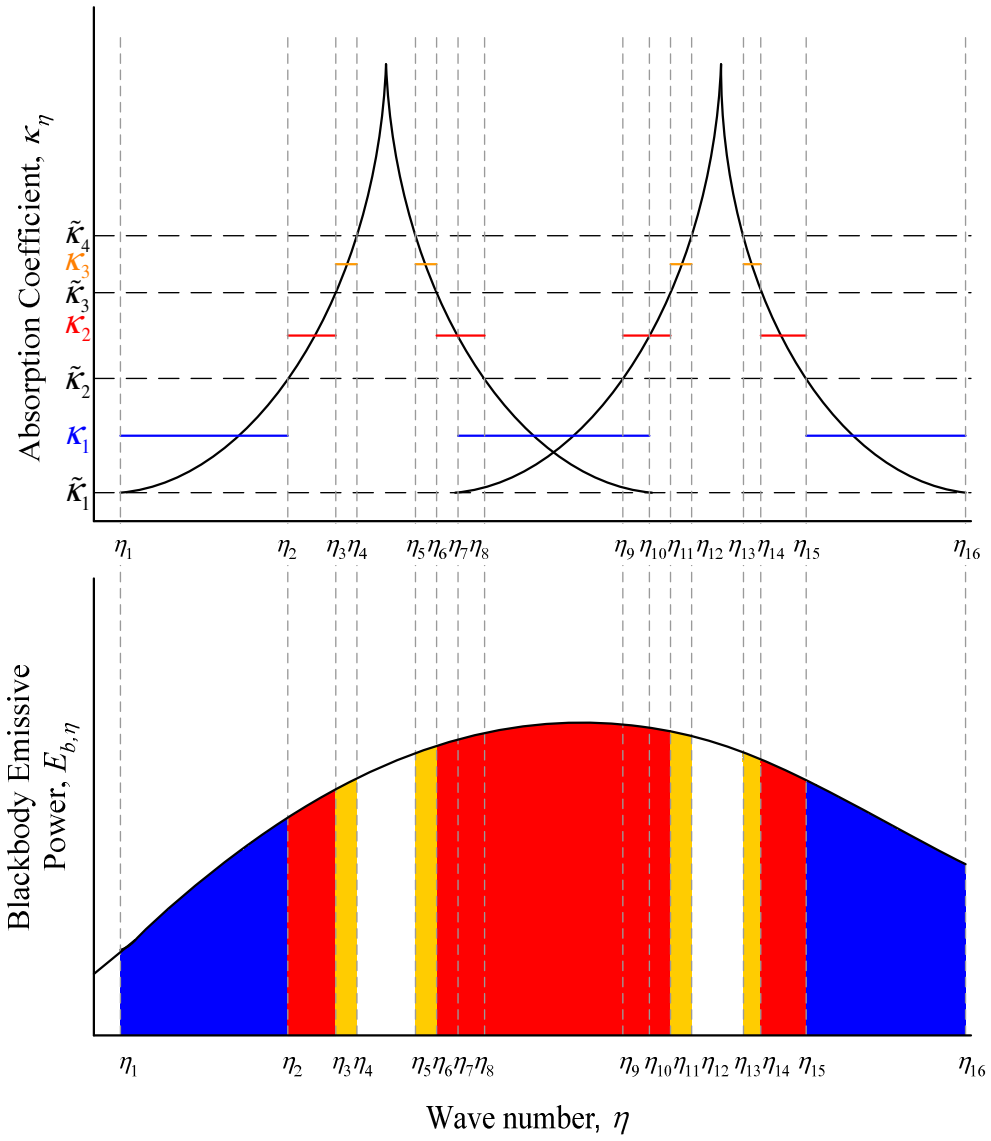

Figure 3.10 Discretization of the re-ordered wave number spectrum (top) and the corresponding blackbody fractions (bottom) for two overlapping bands

3.2.3.3 Calculation of Blackbody Weights

The gray gas weights, a_j , are calculated as the sum of the blackbody fractions for all intervals, $\Delta\eta$, where the actual absorption coefficient, κ_{act}, lies between the bounding supplemental absorption coefficients, $\tilde{\kappa}_j$ and $\tilde{\kappa}_{j+1}$ (where $\tilde{\kappa} = N\tilde{C}_{abs}$).

$$a_j = \sum_i \left[F(\eta_{i-1}, T) - F(\eta_i, T) \right] \quad \text{for} \quad \tilde{\kappa}_j < \kappa_{act}(\Delta\eta_i) < \tilde{\kappa}_{j+1} \tag{3.31}$$

Figure 3.10, demonstrates two overlapping wide bands schematically. As can be seen from the figure, for wave number interval $\Delta\eta_1$ bounded by η_1 and η_2 , the actual absorption coefficient is κ_1, since it is the only contributing gray gas absorption coefficient for that interval. However, when the overlapping regions are considered, for example wave number interval $\Delta\eta_8$, the actual absorption coefficient becomes $2 \cdot \kappa_1$ which is greater than the supplemental absorption coefficient $\tilde{\kappa}_2$ but smaller than $\tilde{\kappa}_3$, hence the blackbody fraction of interval $\Delta\eta_8$ is contributed to gray gas 2.

In Eq. (3.31) F represents the fraction of the total blackbody emissive power defined as;

$$F(\eta, T) = \frac{\int_0^{\eta} E_{b,\eta}\, d\eta}{\int_0^{\infty} E_{b,\eta}\, d\eta} = \frac{1}{\sigma T^4} \int_0^{\eta} E_{b,\eta}\, d\eta \tag{3.32}$$

where $E_{b,\eta}$ is the blackbody emissive power. Chang and Rhee [59], have provided a function for the fractional emission in each band;

$$F(\eta, T) = \frac{15}{\pi^4} \sum_{n=1}^{\infty} \frac{e^{-n\nu}}{n} \left(\nu^3 + \frac{3\nu^2}{n} + \frac{6\nu}{n^2} + \frac{6}{n^3} \right) \tag{3.33}$$

where $\nu = C_2\eta/T$ and C_2=14388 μm K. This series converges to exact result rapidly for n=4 [60] . All weights including the one for transparent gas sum to unity;

$$\sum_{j=1}^{NG} a_j = 1 \tag{3.34}$$

Calculated gray gas absorption coefficients and weights are supplied to the WSGG RTE (Eq. (2.11)) and radiative heat transfer calculations are performed for each gray gas.

CHAPTER 4

RESULTS AND DISCUSSION

The predictive accuracy and computational efficiency of MOL solution of DOM with two nongray radiative property models, namely WBCK and SLW, were assessed by applying it to the predictions of radiative source term distribution and net radiative heat fluxes for which measurements and benchmark solutions had previously been reported in the literature. In order to demonstrate the improvements brought about by these two spectral models over and above the ones obtained by gray gas approximation, predictions obtained by WBCK and SLW models were also compared with those of gray gas model.

For all test problems, which will be described in the following subsections, the S_N scheme of Carlson and Lathrop [46] and ROWMAP integration subroutine [54] were utilized as angular quadrature scheme and ODE solver, respectively. The computational parameters related to the ODE solver subroutine are summarized in Appendix C.

4.1 One-Dimensional Parallel Plate Test Cases

In an attempt to test the predictive accuracy of MOL solution of DOM with WBCK and SLW models, the developed code was first applied to eight one-

dimensional parallel plate test cases for which the conditions are summarized in Table 4.1. The schematic representation for one-dimensional test cases is also demonstrated in Figure 4.1. The predicted radiative source term distributions and net radiative heat fluxes were compared with those of previously reported LBL model [41]. In all eight test cases, the medium was at a total pressure of 1 atm.

For one-dimensional test problems, RTE (Eq. (2.1)) and its discrete ordinates representation were reduced to one-dimensional forms and the resulting equation was transformed into transient form by using false transients approach (see Appendix D). The resulting system of PDEs was transformed into an ODE initial value problem by making use of MOL approach. The transformation was carried out by using two- and three- point upwind discretization schemes for spatial derivative.

Table 4.1 Summary of one-dimensional test cases

Test Case	Medium Composition	Mole Fraction Profile	Temperature Profile	Length [m]
1	100 % H_2O	Uniform	Uniform	0.1 and 1.0
2	10 % H_2O	Uniform	Cosine Profile	2.0
3	H_2O	Parabolic Profile	Uniform	1.0
4	H_2O	Sine Profile	Sine Profile	10.0
5	10 % CO_2	Uniform	Uniform	0.5
6	30 % CO_2	Uniform	Cosine Profile	0.2
7	40 % H_2O+ 20 % CO_2	Uniform	Uniform	0.1
8	H_2O + CO_2	Cosine Profile	Cosine Profile	3.0

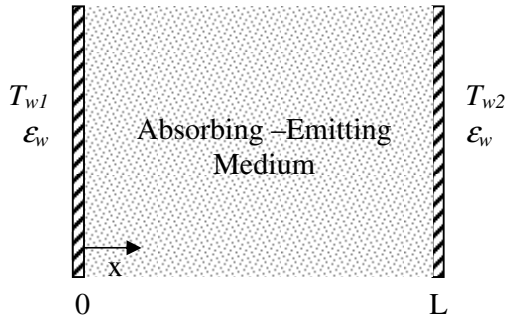

Figure 4.1 Schematic representation for one-dimensional test cases

Effects of order of approximation (S_2, S_4, S_6, S_8), spatial discretization (21, 31, 41, 51, 101 grid points), spatial differencing schemes (DSS012, DSS014) and number of gray gases (10, 15, 20 gray gases) on the predictive accuracy of the method were investigated for all one-dimensional test problems. For the sake of brevity, only the parameter independent results were presented (see Appendix E for independent parameter values).

4.1.1 Test Case 1: Isothermal and Homogeneous Medium of H_2O

In order to assess the predictive ability of the developed code, it was applied to the test problem initially proposed by Kim *et al*. [61]. The physical system under consideration is two black and cold (0 K) parallel plates containing pure water vapor at a uniform temperature of 1000 K. Two wall spacings of a) 0.1 m and b) 1.0 m were considered.

The source term predictions obtained with WBCK and SLW models as well as with gray gas model were compared with those of LBL model [41]. The comparisons are illustrated in Figures 4.2 and 4.3 for L=0.1 m and L=1.0 m, respectively. As can be seen from the figures, for both wall spacings, the predictions obtained with WBCK and SLW models are found to be in excellent agreement with the benchmark solutions. Gray gas model, on the other hand, leads to underprediction of the radiative source term in the vicinity of the walls and overprediction of the radiative source term near the center.

The average and maximum absolute relative percent errors in the source term field for SLW and WBCK models as well as for gray gas model for both wall spacings are listed in Table 4.2. As can be seen from the table, for both wall spacings, the nongray treatment of the medium results in average absolute relative errors less than 3 %. However, when gray gas assumption is invoked, the average absolute relative errors are found to be 11.9 % and 41.3 % for L=0.1 m and L=1.0 m, respectively.

Inspection of the source term distributions in Figures 4.2 and 4.3 reveals that steeper gradients are observed in the vicinity of the walls for optically thinner medium (Figure 4.2), that is the step change between the wall and medium temperatures affects the source term distribution more profoundly. On the other hand, when the medium becomes optically thicker, the radiative source term approaches zero as it does in Figure 4.3. The physical justification of this situation is that in the optically thick central region, the amount of energy emitted from a volume of the gas is close to the amount of energy absorbed by the same gas volume.

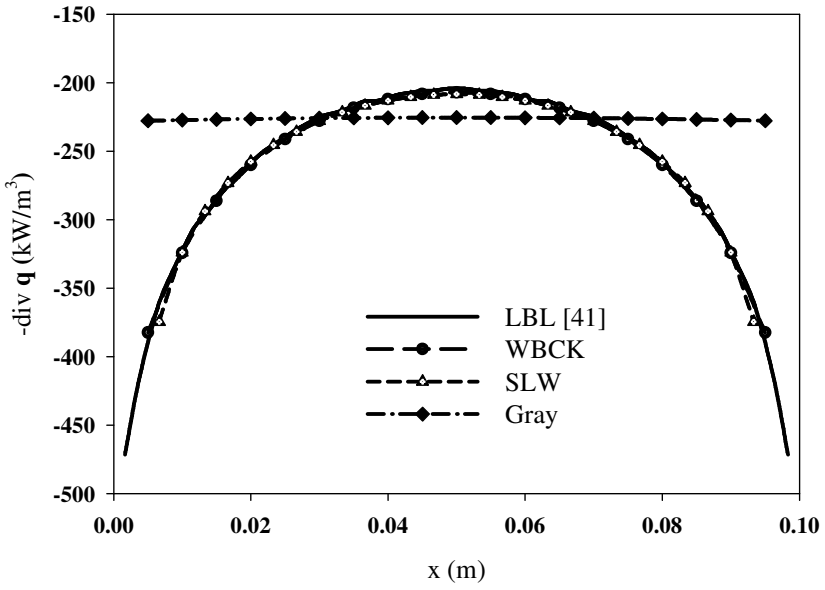

Figure 4.2 Comparison between the source term predictions of the present study and LBL results for 100 % H_2O for L=0.1 m

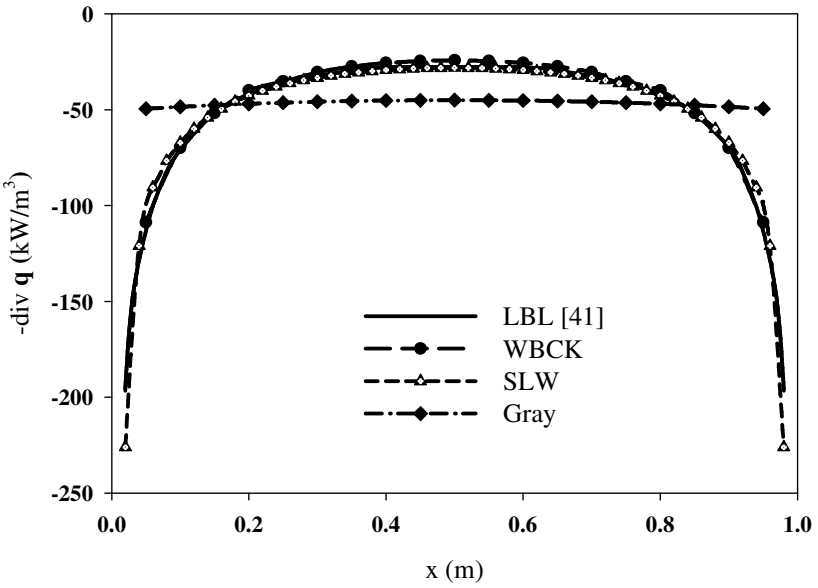

Figure 4.3 Comparison between the source term predictions of the present study and LBL results for 100 % H_2O for L=1.0 m

Table 4.2 Maximum and average percent relative errors in the radiative source term predictions of the present study for test case 1

		Test Case 1(a)	Test Case 1(b)
WBCK	Max. Abs. % Rel. Error[a]	1.4	5.0
	Avg. Abs. % Rel. Error	0.8	2.0
SLW	Max. Abs. % Rel. Error	1.5	5.1
	Avg. Abs. % Rel. Error	0.7	2.7
Gray	Max. Abs. % Rel. Error	29.6	61.8
	Avg. Abs. % Rel. Error	11.9	41.3

[a]Absolute % relative error = (|predicted-LBL| / LBL) × 100

The predicted net radiative heat fluxes on the cold wall were also compared with those of LBL solutions. The results, corresponding errors and CPU times were tabulated in Table 4.3. Inspection of the values in table shows that for test cases 1(a) and 1(b) both models (WBCK and SLW) produce accurate net wall heat fluxes where absolute percentage error never exceeds 7 %. Furthermore, for gray gas model it is seen that the radiative heat flux estimation is much more forgiving when compared to the source term prediction with the lowest execution time requirement.

Table 4.3 Net radiative heat fluxes on the cold wall and relative CPU times for test case 1

Test Case	Model	Net Radiative Heat Flux	Absolute % Error[a]	Relative CPU time
1(a)	LBL	13.6	-	-
	WBCK	12.6	7.3	3700
	SLW	13.9	2.4	9500
	Gray	14.6	7.3	1.0
1(b)	LBL	28.7	-	-
	WBCK	26.7	6.9	2067
	SLW	29.8	3.8	1312
	Gray	30.3	5.6	1.0

[a] Absolute % relative error = $(|q_{predicted}-q_{LBL}| / q_{LBL}) \times 100$

4.1.2 Test Case 2: Non-Isothermal and Homogeneous Medium of H_2O

The physical situation under consideration for test case 2 is a non-isothermal medium of 10 % H_2O confined within black parallel plates. The temperature of the medium is given with the following cosine profile;

$$T = T_{ave} + \frac{\Delta T}{2}\cos(\pi x / L) \tag{4.1}$$

where T_{ave} and ΔT are the average temperature and the maximum temperature difference in the physical system, respectively. x is the spatial distance from the first wall [41]. This temperature profile provides a systematic departure from an isothermal medium by increasing the temperature variation ΔT (see Figure 4.4). Predictions were obtained for ΔT's of a) 100 K, b) 500 K and c) 1000 K and T_{ave} was taken as 1000 K. The walls are black and are spaced 2 m apart.

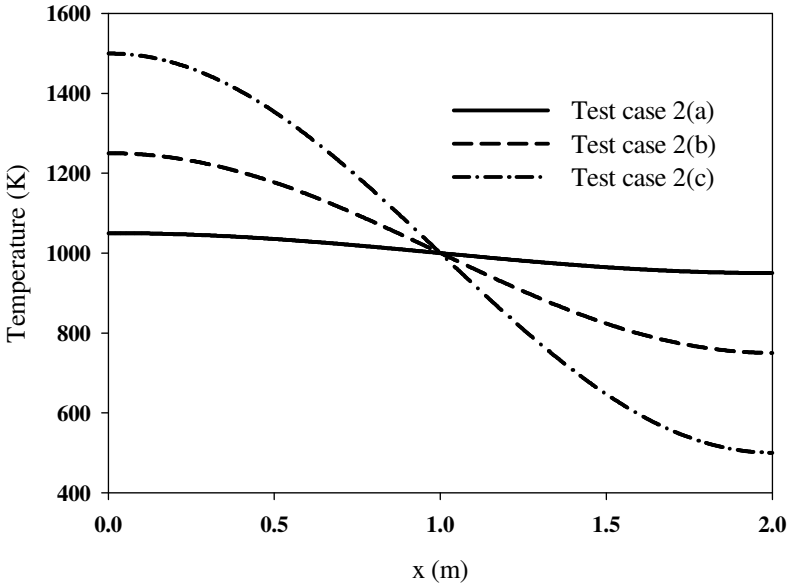

Figure 4.4 Cosine temperature profiles for test case 2 given in Eq. (4.1)

Comparisons between the predictions of LBL model [41] and those of the present study for the source term distribution were illustrated in Figures 4.5, 4.6 and 4.7 for maximum temperature differences of 100 K, 500 K and 1000 K, respectively. Examination of the source term fields in the corresponding figures reveals that as ΔT increases the discrepancies in the cold region increase for both models as well as for gray gas model.

For WBCK model, the error reaches the maximum value in the cold region of the medium where there is overprediction in the absorption. The failure of this method lies in the assumption that a single spectrum constructed at the average temperature of the system may represent the entire domain. Specifically in this test case, the cold regions where gases are less absorbing in reality could not be accurately represented due to the fact that in these regions the real spectrum contains less so-called "hot" absorption lines that become significant at sufficiently high temperatures than the spectrum constructed at the average temperature of the system. Moreover, as ΔT increases the difference between the local temperatures and the average temperature of the medium also increases resulting in higher errors in the cold regions. The same situation is observed when gray gas model was used. On the other hand, in SLW model, since local variation of absorption cross-section with temperature change is accounted for, the discrepancies in the cold regions are less pronounceable. The average and maximum absolute percent relative errors in the source term field for SLW and WBCK models as well as for gray gas model are tabulated in Table 4.4.

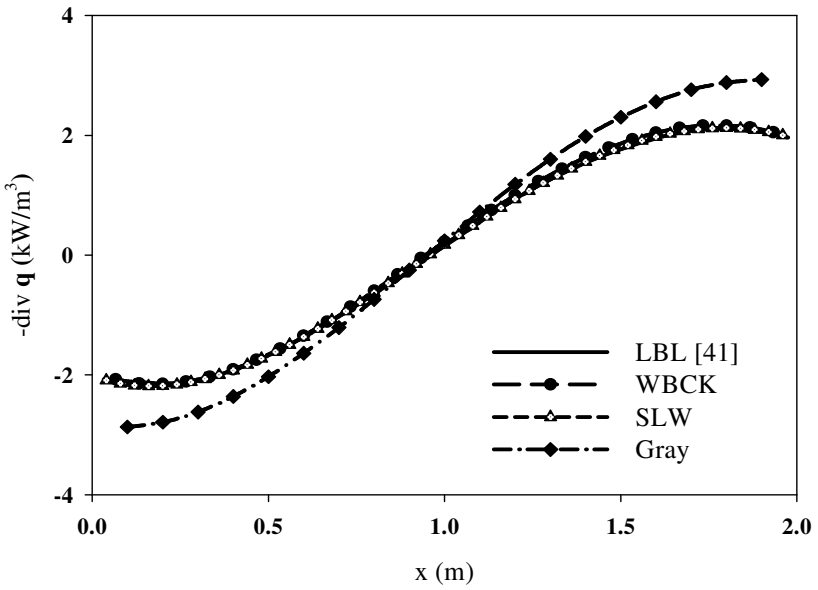

Figure 4.5 Comparison between LBL results and the source term predictions of the present study for 10 % H_2O with cosine temperature profile for ΔT=100 K

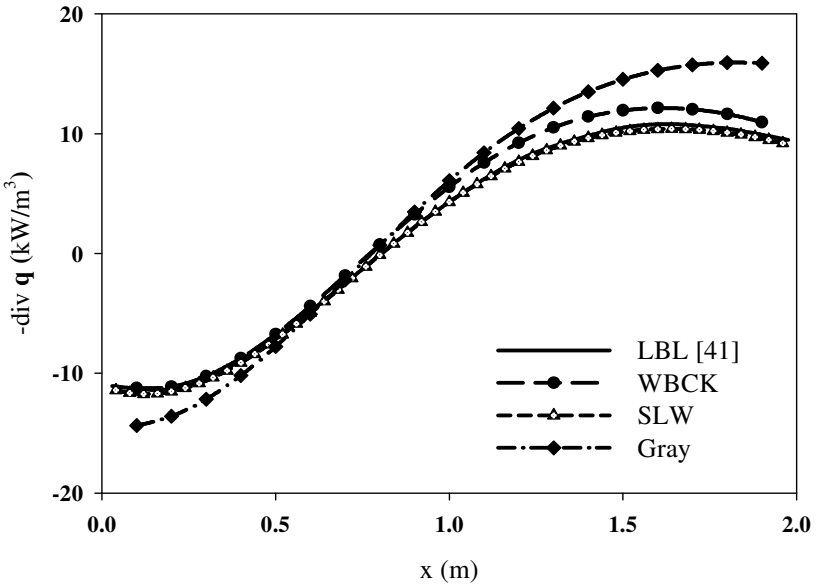

Figure 4.6 Comparison between LBL results and the source term predictions of the present study for 10 % H_2O with cosine temperature profile for ΔT=500 K

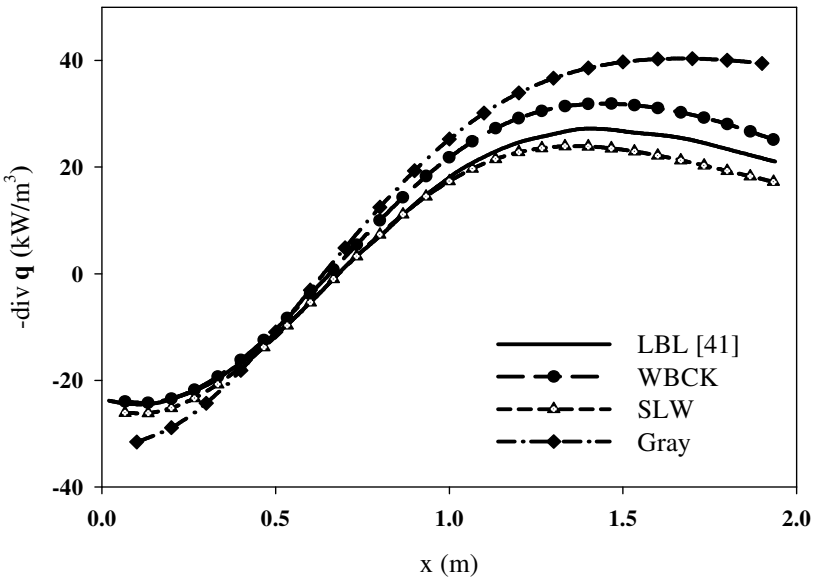

Figure 4.7 Comparison between LBL results and the source term predictions of the present study for 10 % H_2O with cosine temperature profile for ΔT=1000 K

Table 4.4 Maximum and average percent relative errors in the radiative source term predictions of the present study for test case 2

		Test Case 2(a)	Test Case 2(b)	Test Case 2(c)
WBCK	Max. Abs. % Rel. Error	5.0	28.2	41.7
	Avg. Abs. % Rel. Error	2.3	12.3	18.8
SLW	Max. Abs. % Rel. Error	6.6	3.6	17.7
	Avg. Abs. % Rel. Error	1.3	2.1	8.0
Gray	Max. Abs. % Rel. Error	35.0	52.2	76.7
	Avg. Abs. % Rel. Error	23.1	30.5	44.1

The cold wall net radiative heat fluxes calculated in the present study were also compared with those of LBL model [41]. The comparisons and relative computational times were tabulated in Table 4.5. As can be seen from the table, both models (WBCK and SLW) are in good agreement with the LBL solutions for test cases 2(a), 2(b) and 2(c). Moreover, the gray treatment of the medium also produces accurate heat flux predictions.

Table 4.5 Net radiative heat fluxes on the cold wall and relative CPU times for test case 2

Test Case	Model	Net Radiative Heat Flux	Absolute % Error	Relative CPU time
2(a)	LBL	19.6	-	-
	WBCK	19.4	0.8	144
	SLW	19.5	0.4	366
	Gray	19.5	0.4	1
2(b)	LBL	103	-	-
	WBCK	100	2.7	10
	SLW	102	0.3	57
	Gray	99.8	3.1	1
2(c)	LBL	241	-	-
	WBCK	234	2.9	10
	SLW	243	0.9	28
	Gray	228	5.3	1

4.1.3 Test Case 3: Isothermal and Non-Homogeneous Medium of H_2O

This test case, initially proposed by Kim *et al*. [61], consists of two black parallel plates containing an absorbing-emitting medium of H_2O with a uniform temperature field of 1000 K. The concentration of H_2O was given by the following parabolic profile:

$$Y_w = -4x^2 + 4x \tag{4.2}$$

where Y_w is the mole fraction of water vapor and x is the distance from the first wall. The parallel plates were placed 0.1 m apart. The predictions of the present study

were validated against previously reported LBL solutions [41].

Figure 4.8 shows the source term predictions of the present study and those of LBL solutions. As can be seen from the figure, nongray treatment of the medium results in source term distributions with two peaks towards the walls. Kim *et al.* [61] interpreted these features of the nongray solutions as follows: First, since the H_2O concentration goes to zero as the walls are approached there can be no absorption (hence, emission) by the gas. Consequently, source term tends to be zero close to the walls. Secondly, as the gas becomes optically thick, source term tends to be zero at the center. Thirdly, source term cannot be negative under these conditions. Consequently, in view of these conditions nongray solutions yield the source term distributions, shown in the figure. Comparisons presented in Figure 4.8 also show that the best agreement with the benchmark solution is achieved with SLW model. For WBCK model, however, the variation of H_2O concentration leads to relatively large errors near the walls. These discrepancies can be attributed to the use of single spectrum to represent the whole domain. Single spectrum generated at average mole fraction cannot represent the concentration gradient close to the walls correctly. Furthermore, inspection of the figure reveals that the structure of the source term distribution is lost under the gray gas model which treats the medium as optically thin and exhibits a single maximum radiative source term at the center. The average and maximum absolute percent relative errors in the source term field for SLW and WBCK models as well as for gray gas model are tabulated in Table 4.6. As can be seen from the table, the average absolute errors are generally lower than 12 % and 3.4 % for WBCK and SLW models, respectively. However, when gray gas model is employed, the average absolute relative error is found to be 18.4 %.

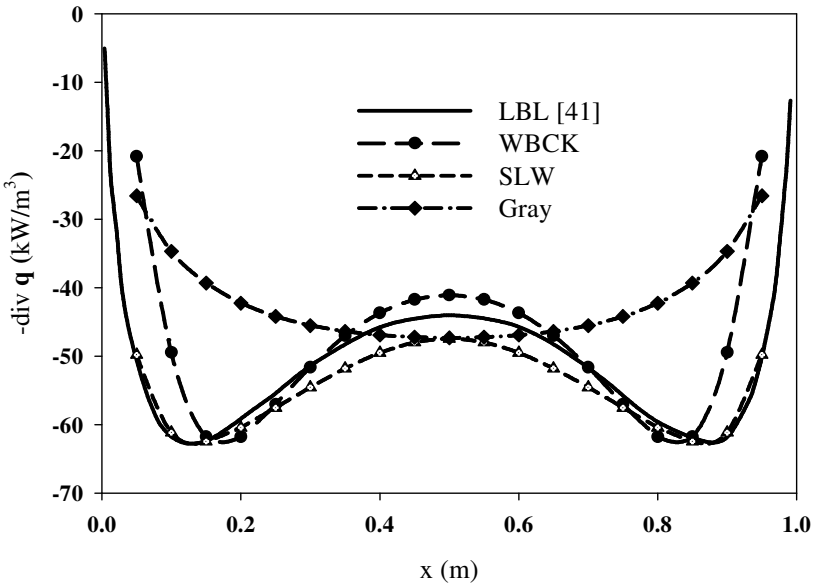

Figure 4.8 Comparison between LBL results and the source term predictions of the present study for H_2O with parabolic concentration profile at 1000 K

Table 4.6 Maximum and average percent relative errors in the radiative source term predictions of the present study for test case 3

	Max. Abs. % Rel. Err.	Avg. Abs. % Rel. Err.
WBCK	50.0	12.0
SLW	8.0	3.4
Gray	43.7	18.4

The predicted net radiative heat fluxes on cold wall were also compared with those of LBL model. Comparisons and corresponding relative computational times were tabulated in Table 4.7. As can be seen from the table, the use of SLW model for

radiative property estimation produces accurate net wall heat fluxes where absolute percentage error is 2 %. This error increases up to 11 % and 20 % for WBCK model and gray gas model, respectively. However, WBCK model turned out to be computationally more economical than SLW model in this test case.

Table 4.7 Net radiative heat fluxes on the cold wall and relative CPU times for test case 3

Model	Net Radiative Heat Flux	Absolute % Error	Relative CPU time
LBL	25.5	-	-
WBCK	22.8	10.7	183.7
SLW	25.8	1.9	3487.5
Gray	20.3	20.4	1.0

4.1.4 Test Case 4: Non-Isothermal and Non-Homogeneous Medium of H_2O

The physical system under consideration consists of water vapor confined between two black parallel plates which are spaced 10 m apart. The temperature and mole fraction profiles within the medium are given with the following sine distributions:

$$T = T_w + (T_c - T_w)\sin(\pi x / L) \tag{4.3}$$

$$Y_w = \sin(\pi x / L) \tag{4.4}$$

where T_w and T_c are the temperatures at the wall and center and were taken as 500 K and 1500 K, respectively. Y_w is the mole fraction of water vapor [41]. Figures 4.9 and 4.10 show the temperature and mole fraction profiles, respectively.

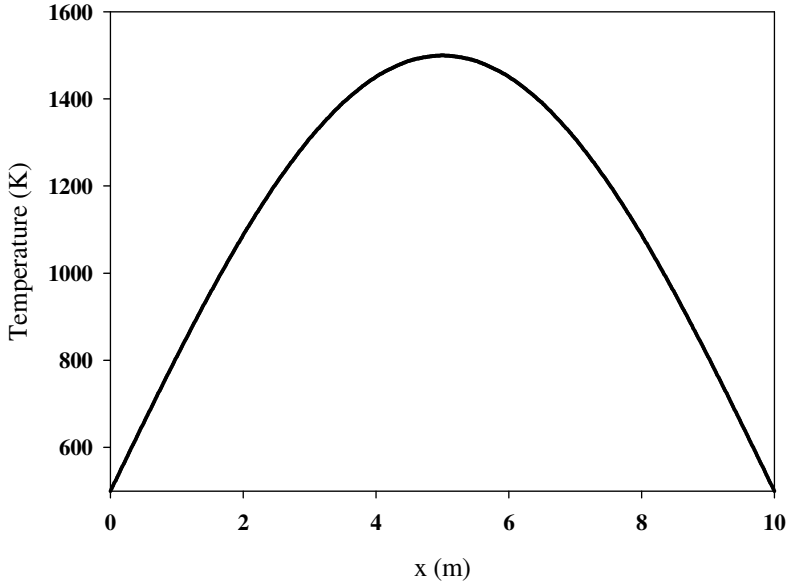

Figure 4.9 Sine temperature profile for test case 4 given in Eq. (4.3)

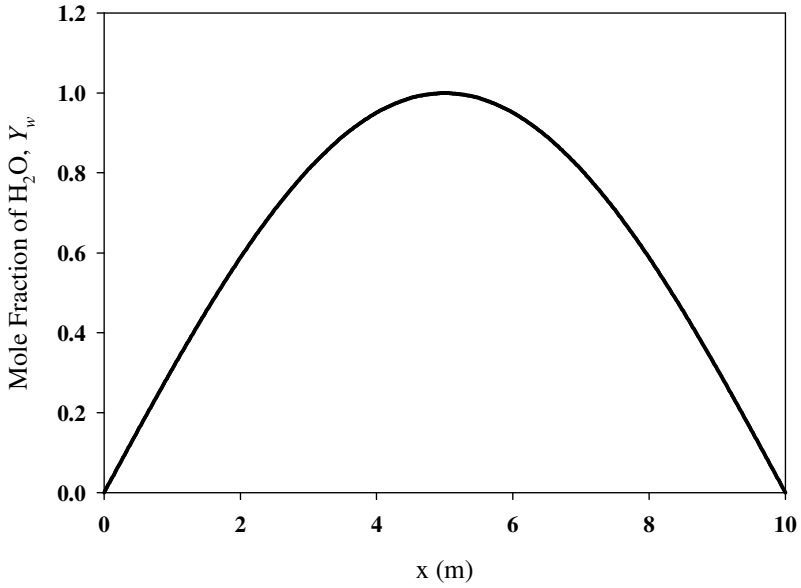

Figure 4.10 Sine mole fraction profile for test case 4 given in Eq. (4.4)

The source term distribution obtained from the present study was benchmarked against LBL solutions available in the literature [41] and the comparisons are illustrated in Figure 4.11. As can be seen from the figure, best agreement is obtained with WBCK model with an average error of 8 % and a maximum error of 16 % near the walls. The maximum absolute error of 13 % is in the center for SLW model; however, the average absolute error is 10 %. For gray treatment of the medium, the maximum error increases up to 40 % near the walls while the average absolute error is 17 %.

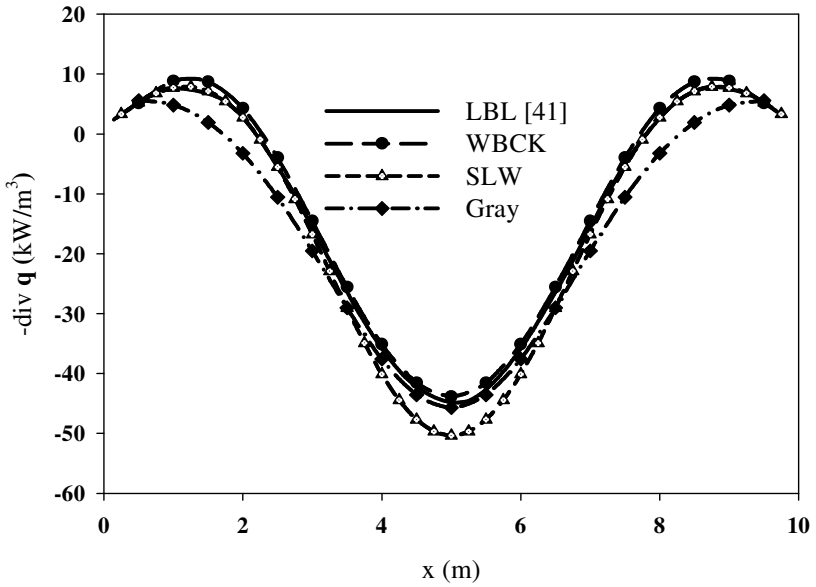

Figure 4.11 Comparison between LBL results and the source term predictions of the present study for H_2O with cosine temperature and concentration profile

The comparison between the net radiative heat fluxes on cold wall predictions of the present study with those of LBL model is given in Table 4.8. As can be seen from the table, the use of both WBCK and SLW models for radiative property estimation produces accurate net wall heat fluxes with absolute percentage errors of

7.5 % and 12.5 %, respectively. This error increases up to 18.5 % for gray gas model.

Table 4.8 Net radiative heat fluxes on the cold wall and relative CPU times for test case 4

Model	Net Radiative Heat Flux	Absolute % Error	Relative CPU time
LBL	62.6	-	-
WBCK	57.9	7.5	483
SLW	70.4	12.5	616
Gray	74.2	18.5	1.0

4.1.5 Test Case 5: Isothermal and Homogeneous Medium of CO_2

The physical system under consideration for test case 5 is an absorbing emitting medium of 10 % CO_2 bounded by two black parallel plates which are spaced 0.5 m apart and are kept at a constant temperature of 300 K. The medium temperature is set to 1500 K [41]. The source term distribution obtained from MOL solution of DOM with WBCK and SLW models as well as with gray gas model were compared with the LBL results [41]. Figure 4.12 illustrates this comparison. As can be seen from the figure, predictions obtained by incorporation of WBCK and SLW models into MOL solution of DOM are found to be in favorable agreement with the LBL solutions. The maximum absolute errors are 13 % and 10 % for WBCK and SLW models, respectively. Gray gas model, on the other hand, gives rise to underprediction of the radiative source term in the medium close to the walls and overprediction of the radiative source term in the center. The average and maximum absolute relative errors are found to be 80 % and 120 %, respectively.

The cold wall net radiative heat fluxes predicted in the present study were also compared with LBL solutions [41]. The results, corresponding errors and computation times were tabulated in Table 4.9. As can be seen from the table, use of

WBCK and SLW models for radiative property estimation produce accurate net wall heat fluxes where absolute relative errors are 9 % and 10 %, respectively. Furthermore, for gray gas model this error increases remarkably up to 20 %.

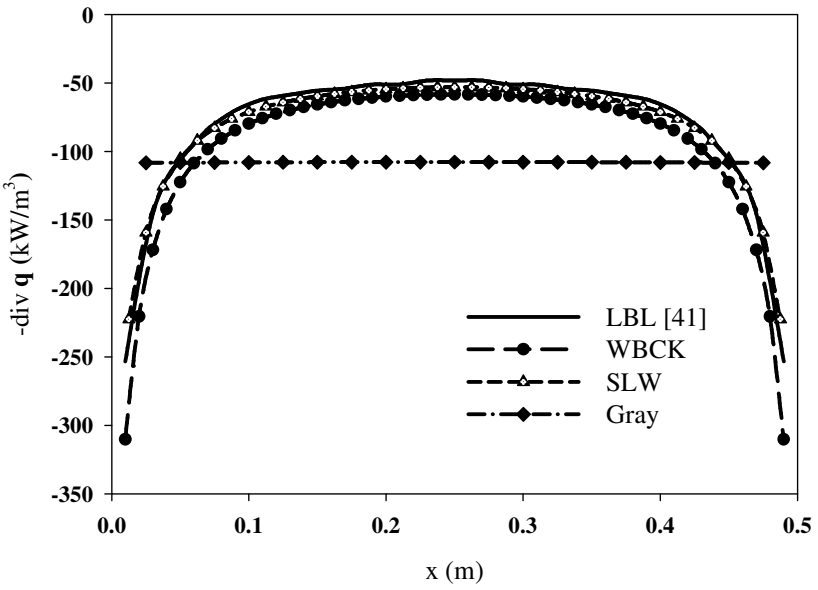

Figure 4.12 Comparison between LBL results and the source term predictions of the present study for 10 % CO_2 at 1500 K (black walls at 300 K)

Table 4.9 Net radiative heat fluxes on the cold wall and required CPU times for test case 5

Model	Net Radiative Heat Flux	Absolute % Error	Relative CPU time
LBL	22.4	-	-
WBCK	24.3	8.8	20.9
SLW	20.2	9.8	14.5
Gray	26.8	20.0	1.0

4.1.6 Test Case 6: Non-Isothermal and Homogeneous Medium of CO_2

The physical system chosen in test case 6 consists of 30 % CO_2 confined between two black parallel plates. The distance between parallel plates is 0.2 m. The temperature profile is given with Eq. (4.1) with T_{ave} and ΔT are taken as 1250 K and 1000 K, respectively [41].

Comparisons between the predictions of LBL model [41] and those of the present study for the source term distribution were illustrated in Figure 4.13. Examination of the source term field given in the figure reveals that for all models the errors increase as the cold wall is approached. The larger errors encountered in the colder region arises from the fact that the spectrum of CO_2 is much more temperature dependent at temperatures below 1000 K [41]. Furthermore, comparisons in Figure 4.13 show that MOL solution of DOM with SLW model is in favorable agreement with LBL solutions with maximum errors of 10 % in the cold region and 15 % in the hot region. It can also be seen from the figure that for the WBCK model, although the maximum absolute error in the hot region is only 10 %, in the cold region the error in the source term increases to approximately 60 %. This error in the source term predicted by WBCK model can be attributed to use of single spectrum generated at average temperature to represent whole domain. Single spectrum cannot model the temperature gradient in the cold region accurately. Significant errors occur in the source term prediction with gray gas model. The errors in the cold and hot regions reach 40 % and 170 %, respectively.

The net radiative heat fluxes on cold wall predicted by MOL solution of DOM with WBCK and SLW models as well as with gray gas model were also compared with those of LBL model [41]. The results and corresponding relative execution times are summarized in Table 4.10. As can be seen from the table, use of WBCK and SLW models as well as gray gas model for radiative property estimation produce accurate net wall heat fluxes where absolute percentage errors are 1.4 % for WBCK model, 0.7 % for both SLW model and gray gas model.

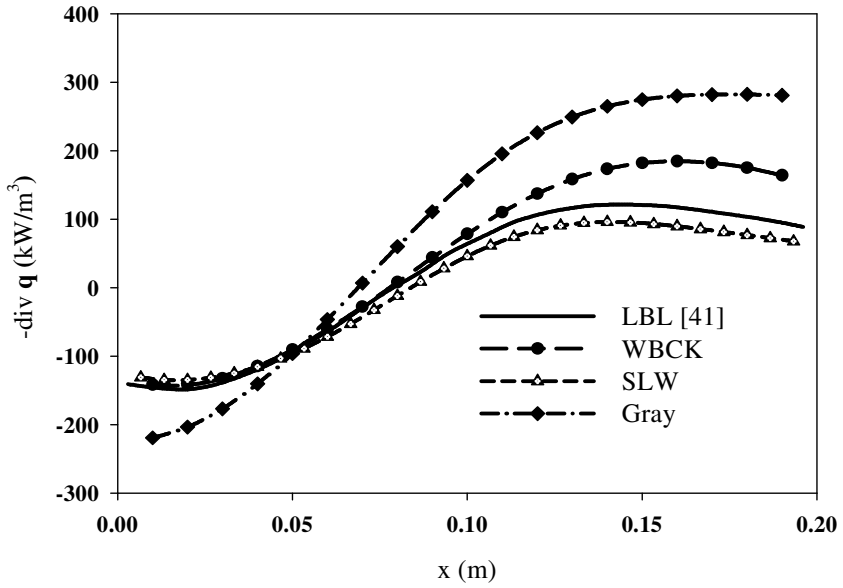

Figure 4.13 Comparison between LBL results and the source term predictions of the present study for 30 % CO_2 with cosine temperature profile

Table 4.10 Net radiative heat fluxes on the cold wall and relative CPU times for test case 6

Model	Net Radiative Heat Flux	Absolute % Error	Relative CPU time
LBL	498	-	-
WBCK	491	1.4	15.3
SLW	494	0.75	4.9
Gray	494	0.75	1

4.1.7 Test Case 7: Isothermal and Homogeneous Medium of H_2O – CO_2 Mixture

The absorbing gas between gray parallel plates consist of 40 % H_2O and 20 % CO_2 at a uniform temperature of 1250 K. The walls with emissivities of 0.8 are spaced 0.1 m apart. The walls are kept at constant temperatures of 400 K and 1500 K [41].

Figure 4.14 demonstrates the comparison between the source term predictions of the present study and those of LBL solutions [41]. As can be seen from the figure, good agreement with the benchmark solutions is obtained when WBCK and SLW models were utilized. The maximum absolute errors are 14 % and 10 % for WBCK and SLW models, respectively. However, the average errors are 5 % for both models. Gray treatment of the medium results in underprediction of the source term distribution with a maximum error of 300 % near the first wall.

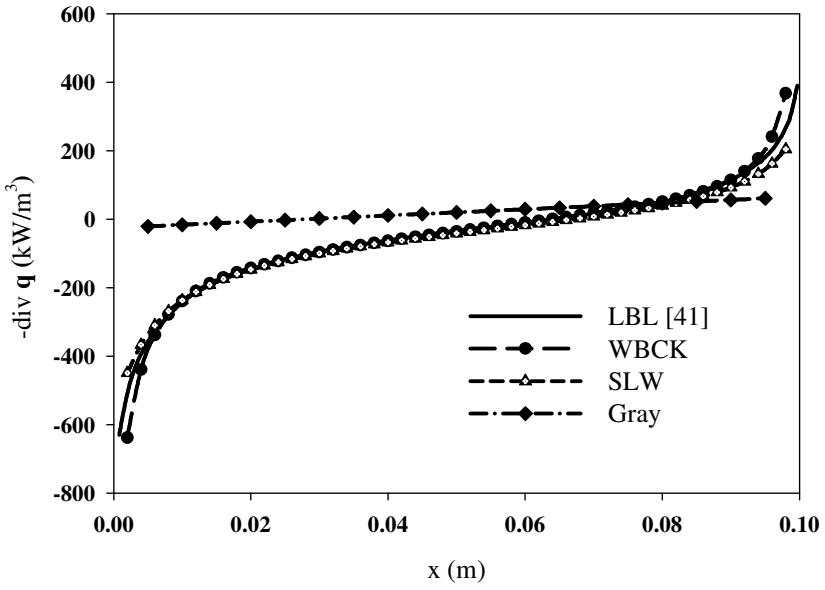

Figure 4.14 Comparison between LBL results and the source term predictions of the present study for 40 % H_2O and 20 % CO_2 mixture at 1250 K (gray walls with ε_w=0.8)

Table 4.11 displays the comparison between the net radiative heat fluxes on cold wall predictions of the present study with those of LBL model. As can be seen from the table, use of WBCK and SLW models as well as gray gas model for radiative property estimation produce accurate net wall heat fluxes where absolute percentage errors are 0.5 % for WBCK model 0.07 % for SLW model and 2.3 % for gray gas model.

Table 4.11 Net radiative heat fluxes on the cold wall and required CPU times for test case 7

Model	Net Radiative Heat Flux	Absolute % Error	Relative CPU time
LBL	184	-	-
WBCK	185	0.5	921
SLW	184.1	0.07	775
Gray	179	2.3	1.0

4.1.8 Test Case 8: Non-Isothermal and Non-Homogeneous Medium of H_2O-CO_2 Mixture

The physical situation under consideration for test case 8 is two gray parallel plates containing an absorbing emitting medium of H_2O and CO_2 mixture. The distance between parallel plates is 3 m. The temperature profile is given with Eq. (4.1) with T_{ave} and ΔT are taken as 700 K and -600 K, respectively. The temperature profile is shown in Figure 4.15. The H_2O and CO_2 mole fractions are given by the same cosine function:

$$Y = Y_{ave} + \frac{\Delta Y}{2}\cos(\pi x / L) \tag{4.5}$$

where Y_{ave} is 0.2 for H_2O and 0.3 for CO_2 and ΔY is -0.3 for H_2O and -0.45 for CO_2 [41] (see Figure 4.16). The ratio of the mole fractions of CO_2 to H_2O is constant at 2/3 which represent the conditions for combustion of many hydrocarbon fuels [37].

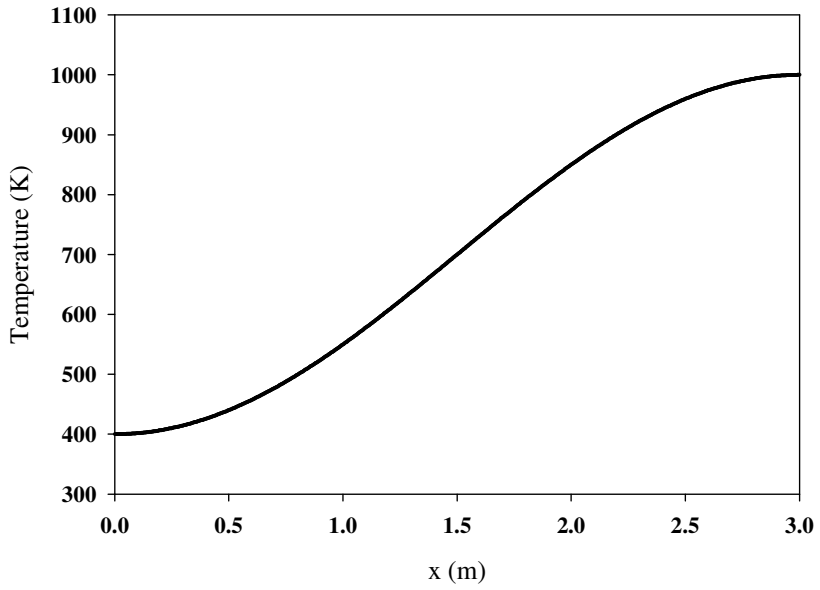

Figure 4.15 Cosine temperature profile for test case 8 given in Eq. (4.1)

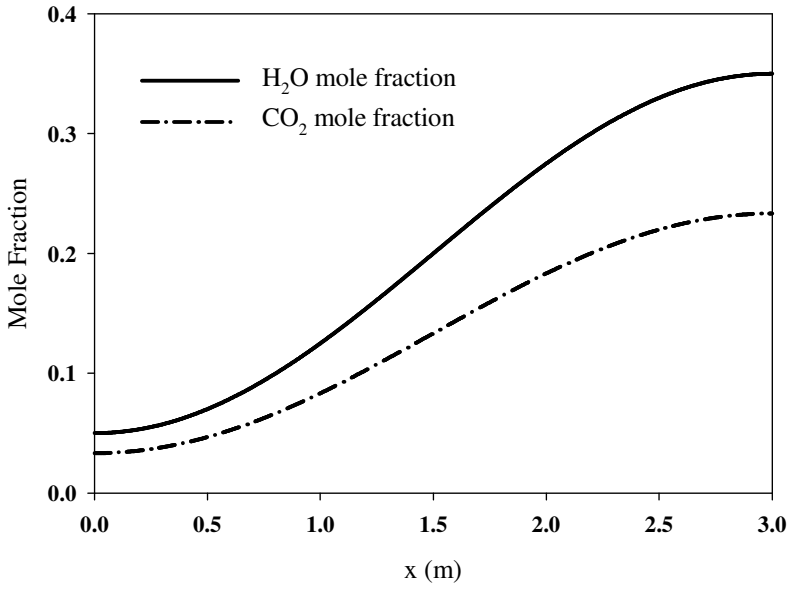

Figure 4.16 Cosine mole fractions for test case 8 given in Eq. (4.5)

Comparison between the source term field predictions of the present study and the LBL solutions [41] is demonstrated in Figure 4.17. Analysis of the figure reveals that, the best agreement with the benchmark solutions is obtained from MOL solution of DOM with SLW model where the maximum error is 10 % in the hot region. WBCK model leads to an overprediction in the radiative source term in the hot region by 30 %. The predictions obtained with gray gas model agree well with the benchmark solution in the hot region, however; the maximum absolute relative error increases up to 190 % in the cold region.

The net radiative heat fluxes on cold wall predicted by MOL solution of DOM with WBCK and SLW models as well as with gray gas model were also compared with those of LBL solutions [41]. The results, together with the errors and computation times were tabulated in Table 4.12. As can be seen from the table, both WBCK and SLW models produce accurate net wall heat fluxes where absolute percentage error is 0.85 % and 0.12 %, respectively. This error increases up to 6.7 % with gray gas model.

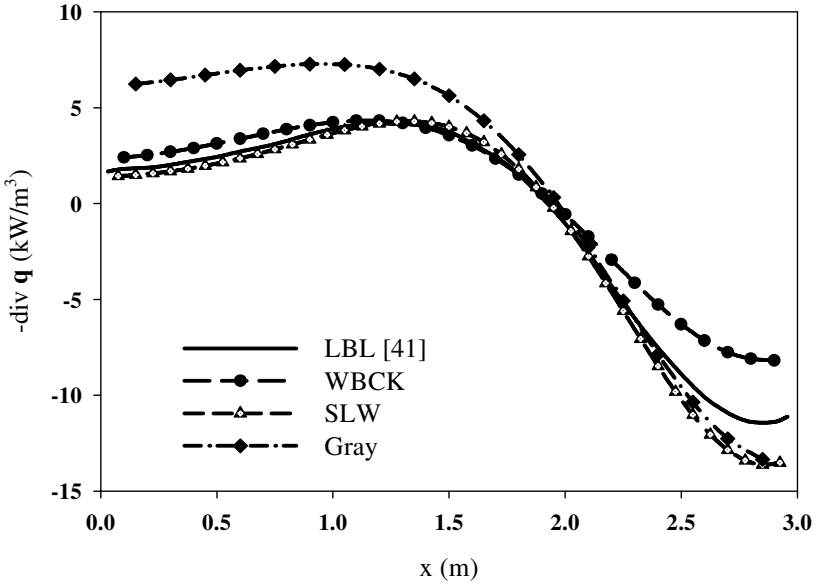

Figure 4.17 Comparison between LBL results and the source term predictions of the present study for H_2O and CO_2 mixture with cosine temperature and concentration profiles (gray walls with ε_w=0.75)

Table 4.12 Net radiative heat fluxes on the cold wall and required CPU times for test case 8

Model	Net Radiative Heat Flux	Absolute % Error	Relative CPU time
LBL	23.3	-	-
WBCK	23.1	0.85	343.2
SLW	23.2	0.12	980
Gray	24.8	6.7	1

4.1.9 Evaluation of Performances of Nongray Models

The computational efficiency of two nongray models, SLW and WBCK were evaluated by applying both models to test cases 5, 6, 7 and 8. In order to provide the same basis for comparison, computations were carried out using the same number of grid points (51), order of approximations (S_6), spatial discretization scheme (DSS014) and number of gray gases (20 gray gases) on a Intel Pentium M 2.1 GHz processor with 1 GB of RAM. The CPU times that the programs use to reach converged results for each test case are tabulated in Table 4.13

Table 4.13 Comparison between performances of WBCK and SLW models

	CPU time (s)			
	Test Case 5	Test Case 6	Test Case 7	Test Case 8
WBCK	8.6	11.2	17.7	52.1
SLW	7.4	15.3	138	211

As can be seen from the table, in isothermal case (test case 5), SLW and WBCK models are comparable in terms of computational efficiency. However, in non-isothermal case (test case 6) WBCK was found to be 37 % faster than SLW model. This is an expected result because WBCK model uses a single spectrum constructed at the average temperature whereas SLW model uses separate spectrums generated at each spatial location. For test case 7, where the medium consists of isothermal and homogeneous mixture of H_2O and CO_2, SLW model turned out to be 8 times slower than WBCK model since in SLW model the RTE is solved for H_2O and CO_2 separately whereas in WBCK model the RTE is solved only once for the mixture. For test case 8 where the medium consists of non-isothermal and non-homogeneous mixture of H_2O and CO_2, WBCK model was found to be 4 times faster than SLW model.

4.1.10 Effect of Medium Temperature and Concentration

A parametric study was performed in order to elucidate the conditions under which the source term predictions obtained with gray gas model agrees with those of nongray gas radiative property models. For this purpose, four cases with identical wall temperatures and wall spacings but different mole fractions and temperatures were selected. The conditions for each case are summarized in Table 4.14.

Table 4.14 Conditions for the cases

	Mole Fraction	Gas Temperature (K)	Wall Temperature (K)	Wall Spacing (m)
Case 1	0.1	1000	500	0.1
Case 2	1.0	1000	500	0.1
Case 3	0.1	2000	500	0.1
Case 4	1.0	2000	500	0.1

Comparisons between the source term predictions obtained with gray gas and SLW models were demonstrated in Figures 4.18 (a)-(d) for Cases 1-4, respectively. Analysis of the figures reveals that the best agreement between the predictions is achieved in Case 1 where the gas temperature and mole fraction are relatively low. The agreement between the predictions results from the considerably low values of absorption coefficients. In Case 2, where the mole fraction of water vapor increases to 1.0 while keeping gas temperature constant at 1000 K, nongray solution yields a parabolic source term distribution, and hence, large discrepancies towards the walls are observed between gray and nongray solutions. In Case 3, where the gas composition is low yet the temperature is high, the shape of source term distribution was found to be almost linear in both gray and nongray solutions (similar to case 1). However, there are large differences between both predictions. Comparison of the profiles for Case 1 and Case 3 shows that while temperature significantly affects the

magnitude of the source terms, it does not change the shape of the source term distribution appreciably. The maximum discrepancy is observed in Case 4 where the temperature and mole fraction of water vapor is high.

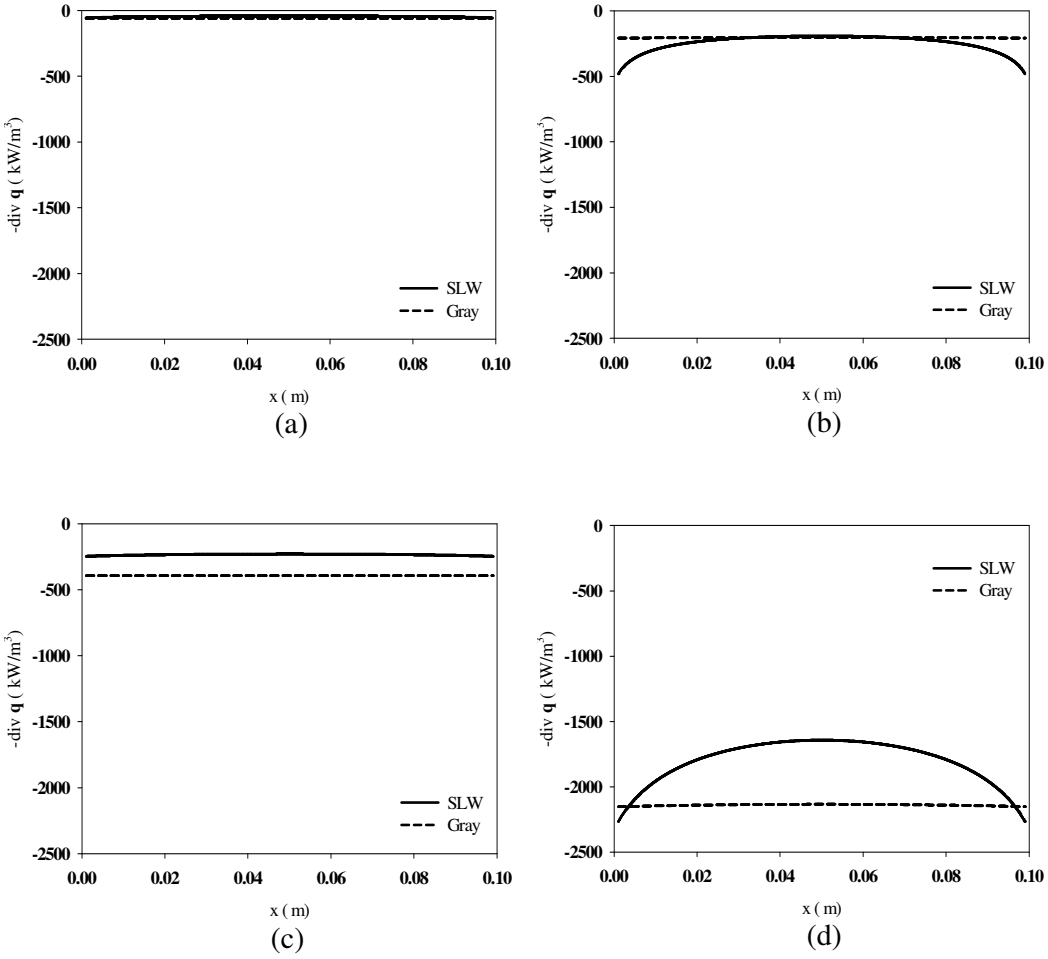

Figure 4.18 Comparisons between the source term predictions obtained with gray gas and SLW models for a) Case 1, b) Case 2, c) Case 3, d) Case 4

On the whole, although temperature affects the magnitude of the source terms, concentration more significantly influences the magnitude of source terms as well as their distribution. Therefore, solutions with gray gas model and non-gray models yield comparable predictions at low temperatures and concentrations.

4.2 Two-Dimensional Axisymmetric Cylindrical Test Cases

Having validated the method on one-dimensional test problems, the predictive accuracy of MOL solution of DOM with WBCK and SLW models were also tested by applying it to two-dimensional test cases involving axisymmetric cylindrical geometry and benchmarking their source term and net radiative heat flux predictions against measurements [62] and LBL results [41].

4.2.1 Isothermal-Homogeneous Medium of H_2O

The predictive accuracy of MOL solution of DOM with WBCK and SLW models was tested by applying it to an isothermal homogeneous two-dimensional test problem for the prediction of centerline source term distribution and net radiative heat flux at the wall. This test problem, proposed by Denison [41], consists of 10 % H_2O at a uniform temperature of 950 K in an axisymmetric cylindrical enclosure. The enclosure is 3 m in diameter and 5 m in length. The walls are gray with emissivities of 0.8 and are kept at a constant temperature of 400 K.

Effects of order of approximation (S_2, S_4, S_6), spatial discretization (7x21, 13x41, 25x81, 31x101 in r- and z-directions, respectively), spatial differencing schemes (DSS012, DSS014) and number of gray gases (10, 15, 20 gray gases) on the predictive accuracy of the method were investigated. However, only the parameter independent results were presented (see Appendix E for independent values).

Figure 4.19 illustrates the comparison between source term distribution predicted by MOL solution of DOM with WBCK and SLW models and LBL solutions along the centerline. As can be seen from the figure the source terms predicted with both models (WBCK and SLW) are in good agreement with the LBL solutions. Utilization of gray gas model, on the other hand, leads to significant errors in the source term distribution. Figure 4.20 shows the comparison between the LBL results of the net radiative heat flux at the wall and those predicted by MOL solution of DOM with WBCK and SLW models. It can be seen that predicted heat fluxes with both models are found to be in very good agreement with the LBL solutions over the whole length of the enclosure. For this test case, the predicted net radiative heat fluxes at the wall and source terms are within 1 % and 6 % of the benchmark,

respectively for WBCK model. Moreover, for SLW model, the predicted net radiative heat fluxes at the wall and source terms are found to be 2 % and 3 % of the benchmark, respectively.

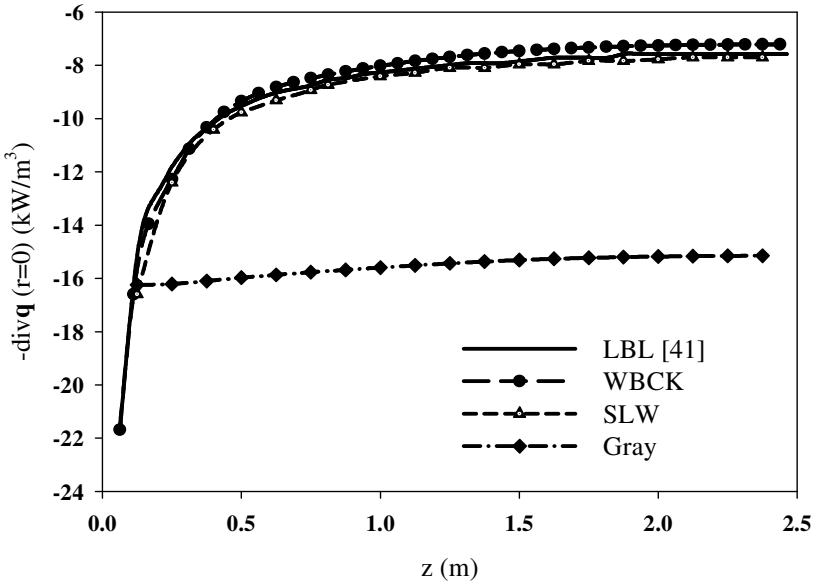

Figure 4.19 Comparison between LBL results and the source term predictions of the present study for 10 % H_2O at uniform temperature of 950 K (gray walls with ε_w=0.8)

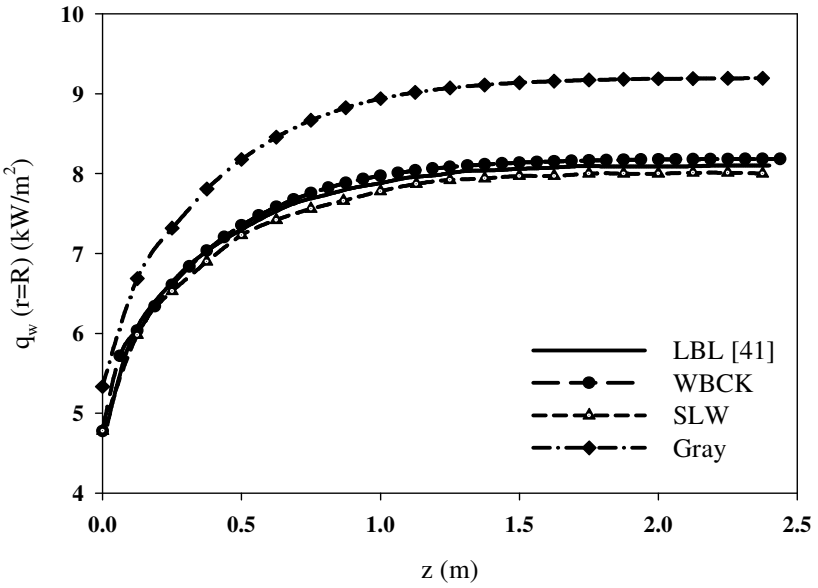

Figure 4.20 Comparison between LBL results and the net wall heat flux predictions of the present study for 10 % H_2O at uniform temperature of 950 K (gray walls with ε_w=0.8)

4.2.2 Gas Turbine Combustor Simulator (GTCS)

The last test case is the combustion chamber of GTCS treated as axisymmetric cylindrical enclosure with diffuse gray walls containing absorbing-emitting medium. Predictive accuracy of MOL solution of DOM with SLW model was assessed by applying it to the prediction of incident radiative heat fluxes on the wall of combustor and comparing its predictions with measurements.

Gas turbine combustor simulator is a cylindrical enclosure containing turbulent diffusion flame of propane mixed with air and was designed, constructed and operated within the framework of NATO-AGARD T51/PEP with the objective of providing experimental data for testing the accuracy of predictions of a novel code for cylindrical combustors.

Figure 4.21 (a) shows a schematic diagram of GTCS. The combustion chamber was one of the main sections of the test rig (air/fuel inlet, fuel conditioning section and combustion chamber). It is about 420 mm in length (excluding exit

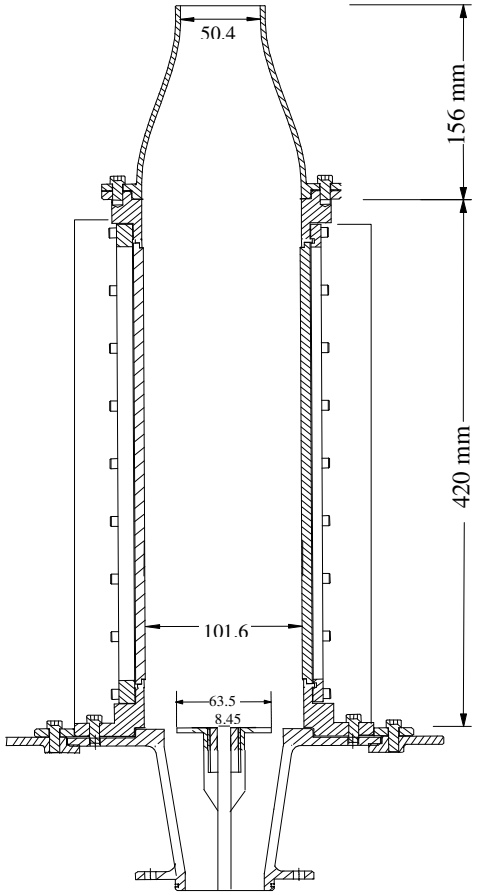

(a)
The physical system: schematic diagram of GTCS

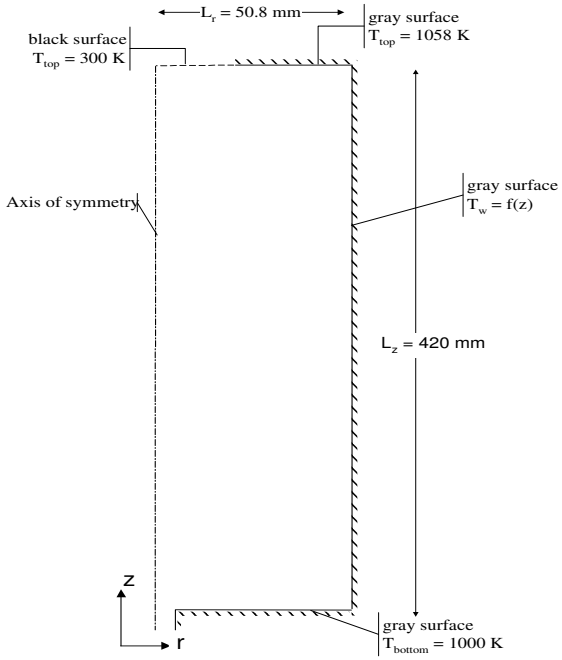

(b)
Treatment of GTCS as 2-D cylindrical enclosure

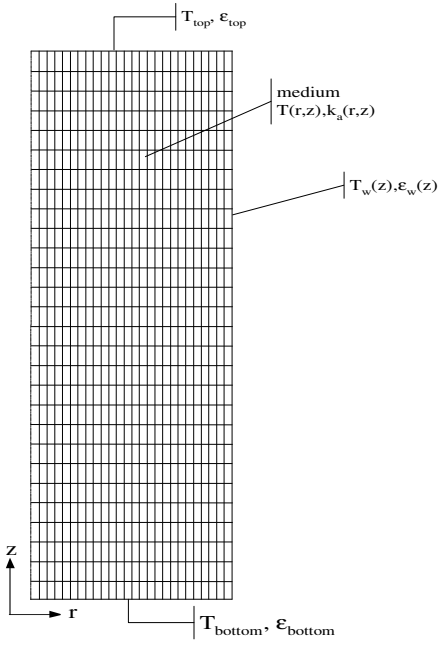

(c)
Solution domain and boundary conditions used in MOL solution of DOM

Figure 4.21 Treatment of GTCS and solution domain for MOL solution of DOM

length), 101.6 mm in diameter with an exit opening of 50 mm in diameter. It was constructed as a confined turbulent diffusion flame with bluff body stabilizer. The air is injected into the chamber around the bluff body while the fuel is injected through the center of the disc. The circular cross-section of the bluff body represents a 65 % area of blockage of the chamber entrance. To reduce thermal losses through the chamber walls, 0.0254 m thick ceramic fiber blanket of Al_2O_3 was wrapped around the chamber from the level of bluff body to the beginning of the exit cone. For the purpose of modeling radiative exchange, the converging exit of the GTCS was approximated by a circular disc of the same diameter as the main body of the combustion chamber, having an inner circular opening of the same diameter as that of the exit cone. Opening is approximated as a black surface which means radiation that leave the opening will not come back and the temperature of the artificial surface is taken to be 300 K which is the surrounding temperature. The physical system and treatment of the combustor are schematically illustrated in Figure 4.21.

Experimental data for wall and gas temperatures, incident radiative heat fluxes along the side wall and gas composition inside the medium were obtained for fuel and air flow rates of 0.0009 m^3/s and 0.0425 m^3/s, respectively, corresponding to an equivalence ratio of 0.5. The range of measurement locations for wall temperatures was 57.2-362.0 mm. Gas temperatures were measured in the ranges of 51.9-354.2 mm in axial and 0-46 mm in radial directions, respectively. Gas and wall temperatures were measured by using uncoated S and K type thermocouples, respectively. The thermocouple measurement uncertainty was reported as ~5 % of readings for the gas temperatures and ~2 % for the wall temperatures. Measured gas compositions were available within 21-291 mm in axial and 0-45 mm in radial directions, respectively. The uncertainty of the readings for the water vapor measurements was reported as ~10 % and ~6 % for carbon dioxide. Incident radiative heat fluxes on the chamber wall were available in the range of 51.5-351.5 mm with ~7 % uncertainty of the reading. Detailed description of the measurements can be found in Kayakol *et al.* [62].

Gas temperature and composition measurements were carried out at discrete points of measurement covering a certain volume of GTCS as mentioned above. These values are reported in [63]. However, for evaluation of radiation parameters at

any grid points throughout the combustor, it is necessary to approximate the values of these parameters in the range outside of the measurements. This has been achieved by fitting fourth order polynomials, along r and z axes separately, which are then used to interpolate and extrapolate measured data throughout the domain. Input data at discrete grid points for gas temperatures and compositions, obtained from these polynomials, are given in [63]. The values of these radiation variables required for any other grid resolution are calculated from the known values by using two-dimensional Lagrange interpolation, by using the formula below

$$T(\mathrm{i},\mathrm{j}) = \left[\frac{z(\mathrm{j}) - z(\mathrm{N})}{z(\mathrm{N}) - z(\mathrm{N}+1)}\right]\times\left[\frac{r(\mathrm{i}) - r(\mathrm{M})}{r(\mathrm{M}) - r(\mathrm{M}+1)}\right]\times \left[\, T(\mathrm{M},\mathrm{N}) - T(\mathrm{M}+1,\mathrm{N}) - T(\mathrm{M},\mathrm{N}+1) + T(\mathrm{M}+1,\mathrm{N}+1)\right] \tag{3.6}$$

which is illustrated schematically in Figure 4.22.

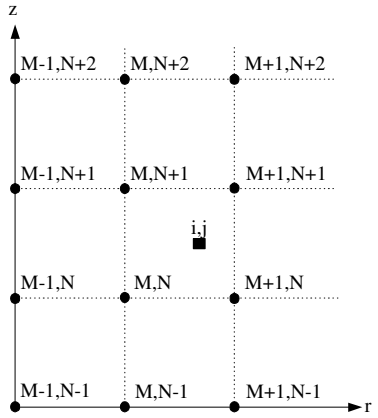

Figure 4.22 Schematic representation of the nodes used in Lagrange interpolation

The comparison between the measured incident radiative heat flux and those predicted by MOL solution of DOM with SLW model is illustrated in Figure 4.23.

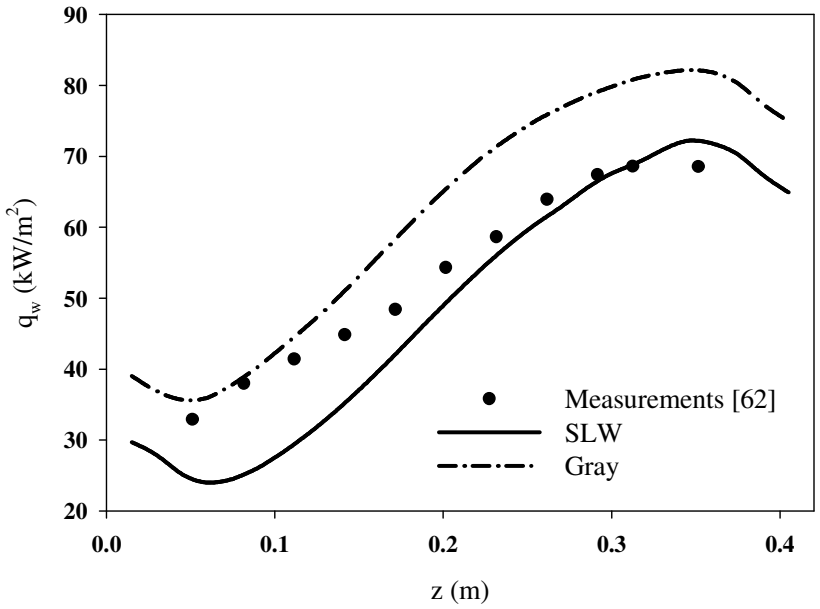

Figure 4.23 Comparison between measured incident heat fluxes with predictions of MOL solution of DOM with SLW model and gray gas model

Analysis of Figure 4.23 indicates that for the GTCS application, the incident heat flux prediction of SLW model shows slightly better agreement with the measurements in comparison to the gray gas model. For this experimental test case, Kayakol et al. [62] reported that the uncertainty in the heat flux measurements is ~7 %. Hence, the observed discrepancy between the computational predictions with SLW model and the experimental data can be attributed to the uncertainties in the measurements as the same method of solution reproduced the benchmark solutions perfectly in the previous test cases.

CHAPTER 5

CONCLUSIONS

A radiation code based on MOL solution of DOM for the prediction of radiative heat transfer in nongray absorbing-emitting media was developed. WBCK and SLW models were chosen for the estimation of spectral radiative properties of participating gases due to their computational efficiency and compatibility with MOL solution of DOM. The predictive accuracy and computational efficiency of the developed code was assessed by applying it to the simulation of radiative heat transfer in several test problems and comparing its predictions with LBL solutions or measurements. Predictions obtained with the WBCK and SLW models were also compared with those of gray gas model in order to show the improvements brought about by these two spectral models in addition to the ones obtained with gray gas approximation.

The code was first applied to prediction of net wall radiative heat fluxes and source terms in several one-dimensional parallel plate test problems including isothermal/non-isothermal and homogeneous/non-homogeneous media of water vapor, carbon dioxide or mixture of both. Predicted steady-state solutions were validated against LBL results. Comparisons show that, for isothermal and homogeneous media, both WBCK and SLW models produce accurate source term and net wall radiative heat flux predictions with low computational costs. In the case of non-isothermal and non-homogeneous media, on the other hand, SLW model

yields the most accurate results at the expense of computational time. Moreover, gray gas model may lead to high errors in the source term predictions when compared to spectral models.

Having validated the predictions of the code on one-dimensional test problems, its performance was also tested by applying it to two different two-dimensional axisymmetric cylindrical test problems. In the first problem which involves isothermal and homogeneous medium of water vapor, the source term and net wall radiative heat flux predictions obtained from MOL solution of DOM with WBCK and SLW models were found to be in excellent agreement with the LBL results. However, in the second problem which is Gas Turbine Combustor Simulator (GTCS) containing a non-isothermal and non-homogeneous medium of water vapor and carbon dioxide mixture, discrepancies were observed between the incident wall radiative heat flux predictions of MOL solution of DOM with SLW model and measurements. The observed discrepancies can be attributed to the uncertainties in the measurements.

Finally, a parametric study was performed in order to ascertain the conditions under which the predictions obtained with gray gas model agrees with those of gas spectral radiative property models. Source term predictions obtained with gray and spectral models are found to be in reasonable agreement only for problems containing low concentration absorbing-emitting media at low temperatures.

5.1 Suggestions for Future Work

Based on the experience gained in this study, the following recommendations for future extension of the work are suggested:

- The radiation code developed to simulate the radiation field can be strongly recommended for incorporation into a novel CFD code based on the same approach under development of this department.
- The computational burden of the code can be reduced by optimization of the SLW model.

- Modification of the code for the treatment of absorbing-emitting-scattering medium is required.
- Effect of absorption coefficient on the predictions obtained with gray and spectral models can be investigated in detail.

REFERENCES

[1] Oymak, O., The Method of Lines Solution of Time-Dependent 2D Navier-Stokes Equations for Incompressible Separated Internal Flows, Ph.D. Thesis, Middle East Technical University, Ankara, Turkey, 1997.

[2] Oymak, O. and N. Selçuk, MOL vs FDM Solutions of an Unsteady Viscous Flow Problem, *Proc. of International Conference on Numerical Methods in Laminar and Turbulent Flow*, VIII, Part 1, pp. 153-162, 1993

[3] Oymak, O. and N. Selçuk, Method of Lines Solution of Time-Dependent Two-Dimensional Navier-Stokes Equations, *International Journal of Numerical Methods in Fluids*, Vol. 23, pp. 455-466, 1996.

[4] Oymak, O. and N. Selçuk, Transient Simulation of Internal Separated Flows Using an Intelligent High-Order Spatial Discretization Scheme, *International Journal of Numerical Methods in Fluids*, Vol. 24, pp. 759-769, 1997.

[5] Oymak, O. and N. Selçuk, The Method of Lines Solution of Time-Dependent 2D Navier-Stokes Equations Coupled with the Energy Equation, *Proc. of CHT 97: Advances in Computational Heat Transfer*, Çeşme, Turkey, Begell House, pp. 256-264, 1997

[6] Selçuk, N. and O. Oymak, A Novel Code for the Prediction of Transient Flow Field in a Gas Turbine Combustor Simulator, *Proc. of NATO/RTA/AVT Symposium on Gas Turbine Engine Combustion, Emissions and alternative Fuels*, Lisbon, Portugal, NATO/RTA Meeting Proceedings 14, pp. 11/1-10, 1999

[7] Erşahin, C., Parallelization of a Transient Navier-Stokes Code Based on Method of Lines, M. Sc. Thesis, Middle East Technical University, Ankara, Turkey, 2001.

[8] Fiterman, A., R. Ben-Zvi, and A. Kribus, Dots: Pseudo-Time Stepping Solution of the Discrete Ordinate Equations, *Numerical Heat Transfer Part B-Fundamentals*, Vol. 35, pp. 163-183, 1999.

[9] Yucel, A., Solution of the Discrete Ordinates Equations for a Radiatively Participating Medium by the Method of Lines, *Proc. of Advances in Computer Methods for Partial Differential Equations VII*, New Brunswick: IMACS, pp. 838-844, 1992

[10] Selçuk, N. and N. Kayakol, Evaluation of Discrete Ordinates Method for Radiative Transfer in Rectangular Furnaces, *International Journal of Heat and Mass Transfer*, Vol. 40, pp. 213-222, 1997.

[11] Selçuk, N., G. Kırbaş, and T. Tarhan, Evalution of Method of Lines Solution of Discrete Ordinates Method and Finite Volume Method in a Planar Medium, *Proc. of International Conference on Computational Heat and Mass Transfer*, Gazimağusa, Northern Cyprus, Eastern Mediterranean University Printing House, Gazimağusa, Northern Cyprus, pp. 358-364, 1999

[12] Kırbaş, G., The Method of Lines Solution of Discrete Ordinates Method for Radiative Heat Transfer in Enclosure, M.Sc. Thesis, Middle East Technical University, Ankara, Turkey, 1999.

[13] Selçuk, N. and G. Kirbaş, The Method of Lines Solution of the Discrete Ordinates Method for Radiative Heat Transfer in Enclosures, *Numerical Heat Transfer Part B-Fundamentals*, Vol. 37, pp. 379-392, 2000.

[14] Selçuk, N., A. Batu, and I. Ayrancı, Performance of Method of Lines Solution of Discrete Ordinates Method in the Freeboard of a Bubbling Fluidized Bed Combustor, *Journal of Quantitative Spectroscopy and Radiative Transfer*, Vol. 73, pp. 503-516, 2002.

[15] Ayrancı, I., The Method of Lines Solution of Discrete Ordinates Method for Radiative Heat Transfer in 3-D Enclosures Containing Scattering Media, M. Sc. Thesis, Middle East Technical University, Ankara, Turkey, 2001.

[16] Harmandar, S. and N. Selçuk, The Method of Lines Solution of the Discrete Ordinates Method for Radiative Heat Transfer in Cylindrical Enclosures, *Journal of Quantitative Spectroscopy and Radiative Transfer*, Vol. 84(4), pp. 395-407, 2004.

[17] Ayrancı, I. and N. Selçuk, MOL Solution of DOM for Radiative Transfer in 3-D Scattering Media, *Journal of Quantitative Spectroscopy and Radiative Transfer*, Vol. 84, pp. 409-422, 2004.

[18] Selçuk, N., A.B. Uygur, I. Ayranci, and T. Tarhan, Transient Simulation of Radiating Flows, *Journal of Quantitative Spectroscopy and Radiative Transfer*, Vol. 93(1-3), pp. 151-161, 2005.

[19] Taine, J., A Line-by-Line Calculations of Low-Resolution Radiative Properties of CO_2-CO-Transparent Nonisothermal Gases Mixtures up to 3000 K, *Journal of Quantitative Spectroscopy and Radiative Transfer*, Vol. 30, pp. 371-379, 1983.

[20] Goody, R.M. and Y.L. Yung, *Atmospheric Radiation*, Clarendon Press, Oxford, 1989.

[21] Liu, F., Ö.L. Gülder, and G.J. Smallwood, Non-Grey Gas Radiative Transfer Analysis Using the Statistical Narrow-Band Model, *International Journal of Heat and Mass Transfer*, Vol. 41(14), pp. 2227-2236, 1998.

[22] Edwards, D.K., Molecular Gas Band Radiation, *Advances in Heat Transfer*, Vol. 12, pp. 115-193, 1976.

[23] Ströhle, J. and P.J.Coelho, On the Application of the Exponential Wide Band Model to the Calculation of Radiative Heat Transfer in One- and Two-Dimensional Enclosures, *International Journal of Heat and Mass Transfer*, Vol.45, pp. 2129-2139, 2002.

[24] Goody, R.M., R. West, L. Chen, and D. Chrisp, The Correlated-*k* Method for Radiation Calculations in Non-Homogeneous Atmospheres, *Journal of Quantitative Spectroscopy and Radiative Transfer*, Vol. 42, pp. 539-550, 1989.

[25] Lacis, A.A. and V. Oinas, A Description of the Correlated-*k* Distribution Method for Modeling Nongray Gaseous Absorption, Thermal Emission, and Multiple Scattering in Vertically Inhomogeneous Atmospheres, *Journal of Geophysical Research*, Vol. 96, pp. 9027-9063, 1991.

[26] Coelho, P.J., Numerical Simulation of Radiative Heat Transfer from Non-Gray Gases in Three-Dimensional Enclosures, *Journal of Quantitative Spectroscopy and Radiative Transfer*, Vol. 74, pp. 307-328, 2001.

[27] Marin, O. and R.O. Buckius, Wideband Correlated-*k* Method Applied to Absorbing, Emitting and Scattering Media, *Journal of Thermophysics and Heat Transfer*, Vol. 10, pp. 364-371, 1996.

[28] Parthasarathy, G., J.C. Chai, and S.V. Patankar, A Simple Approach to Non-Grey Gas Modelling, *Numerical Heat Transfer Part B-Fundamentals*, Vol. 29, pp. 113-123, 1996.

[29] Denison, M.K. and W.A. Fiveland, A Correlation for the Reordered Wave Number of the Wide-Band Absorptance of Radiating Gases, *ASME Journal of Heat Transfer*, Vol.119, pp. 853-856, 1997.

[30] Lee, P.Y.C., K.G.T. Hollands, and G.D. Raithby, Reordering the Absorption Coefficient within the Wide Band for Predicting Gaseous Radiant Exchange, *Journal of Heat Transfer*, Vol. 118, pp. 394-400, 1996.

[31] Hottel, H.C. and A.F. Sarofim, *Radiative Transfer*, McGraw-Hill, New York, 1967.

[32] Smith, T.F., Z.F. Shen, and J.N. Friedman, Evaluation of Coefficients for the Weighted Sum of Gray Gases Model, *ASME Journal of Heat Transfer*, Vol. 104, pp. 602-608, 1982.

[33] Modest, M.F., The Weighted-Sum-of-Gray-Gases Model for Arbitrary Solution Methods in Radiative Transfer, *ASME Journal of Heat Transfer*, Vol. 113, pp. 650-656, 1991.

[34] Denison, M.K. and B.W. Webb, *k*-Distributions and Weighted-Sum-of-Gray-Gases-a Hybrid Model, *Heat Transfer*, Vol. 2, pp. 19-24, 1994.

[35] Denison, M.K. and B.W. Webb, A Spectral Line-Based Weighted-Sum-of-Gray-Gases Model for Arbitrary RTE Solvers, *ASME Journal of Heat Transfer*, Vol. 115, pp. 1004-1012, 1993.

[36] Denison, M.K. and B.W. Webb, An Absorption-Line Blackbody Distribution Function for Efficient Calculation of Gas Radiative Transfer, *Journal of Quantitative Spectroscopy and Radiative Transfer*, Vol. 50, pp. 499-510, 1993.

[37] Denison, M.K. and B.W. Webb, The Spectral Line-Based Weighted-Sum-of-Gray-Gases Model for H_2O/CO_2 Mixtures, *ASME Journal of Heat Transfer*, Vol. 117, pp. 788-792, 1995.

[38] Denison, M.K. and B.W. Webb, The Spectral Line-Based Weighted-Sum-of-Gray-Gases Model in Non-Isothermal Non-Homogeneous Media, *ASME Journal of Heat Transfer*, Vol. 117, pp. 359-365, 1995.

[39] Denison, M.K. and B.W. Webb, Development and Application of an Absorption-Line Blackbody Distribution Function for CO_2, *International Journal of Heat and Mass Transfer*, Vol. 38, pp. 1813-1821, 1995.

[40] Rothman, L.S., R.R. Gamache, R.H. Tipping, C.P. Rinsland, M.A.H. Smith, D.C. Benner, V.M. Devi, J.M. Flaud, C. Camy-Peyret, A. Perrin, A. Goldman, S.T. Massie, and L.R. Brown, The Hitran Molecular Database: Editions of 1991 and 1992a, *Journal of Quantitative Spectroscopy and Radiative Transfer*, Vol. 48(5/6), pp. 469-507, 1992.

[41] Denison, M.K., A Spectral Line-Based Weighted-Sum-of-Gray-Gases Model for Arbitrary RTE Solvers, Ph.D. Thesis, Brigham Young University, Provo, Utah, 1994.

[42] Solovjov, V., Spectral Line-Based Weighted Sum of Gray Gases Modeling of Radiative Heat Transfer in Multicomponent Mixtures of Hot Gases, Ph.D. Thesis, Brigham Young University, Provo, Utah, 1999.

[43] Solovjov, V.P. and B.W. Webb, SLW Modeling of Radiative Transfer in Multicomponent Gas Mixtures, *Journal of Quantitative Spectroscopy and Radiative Transfer*, Vol. 65, pp. 655-672, 2000.

[44] Goutiére, V., A. Charette, and L. Kiss, Comparative Performance of Nongray Gas Modeling Techniques, *Numerical Heat Transfer Part B-Fundamentals*, Vol. 41, pp. 361-381, 2002.

[45] Kayakol, N., Discrete Transfer and Discrete Ordinates Methods for Radiative Heat Transfer in Furnaces, Ph.D. Thesis, Middle East Technical University, Ankara, Turkey, 1998.

[46] Carlson, B.G. and K.D. Lathrop, *Transport Theory-the Method of Discrete Ordinates*, Computing Methods in Reactor Physics, ed. H. Greenspan, C.N. Kelber, and D. Okrent, Gordon and Breach, New York, 1968.

[47] Hyde, J. and J.S. Truelove, *The Discrete Ordinates Approximation for Multidimensional Radiant Heat Transfer in Furnaces*. 1977.

[48] Schiesser, W.E., *The Numerical Method of Lines in Integration of Partial Differential Equations*, Academic Press Inc., San Diego, 1991.

[49] Selçuk, N. and N. Kayakol, Evaluation of Angular Quadrature and Spatial Differencing Schemes for Discrete Ordinates Method in Rectangular Furnaces, *Proc. of Proceedings of 31st National Heat Transfer Conference*, Houston, Texas, 325(3), ASME HDT, pp. 151-158, 1996

[50] Chai, J.C., H.S. Lee, and S.V. Patankar, Ray Effect and False Scattering in the Discrete Ordinates Method, *Numerical Heat Transfer Part B-Fundamentals*, Vol. 24, pp. 373-389, 1993.

[51] Fiveland, W.A., The Selection of Discrete Ordinate Quadrature Sets for Anisotropic Scattering*, Fundamentals of Radiation Heat Transfer*. 1991. pp. 89-96.

[52] Wakil, N.E. and J.F. Sacadura, Some Improvements of Discrete Ordinates Method for the Solution of the Radiative Transport Equation in Multi-Dimensional Anisotropically Scattering Media*, Developments in Radiative Heat Transfer*, pp. 119-127, 1992.

[53] Saucez, P., W.E. Schiesser, and A.V. Wouver, Upwinding in the Method of Lines, *Mathematics and Computers in Simulation*, Vol. 56, pp. 171-185, 2001.

[54] Weiner, R., B.A. Schmitt, and H. Podhaisky, Rowmap- a Row-Code with Krylov Techniques for Large Stiff Odes, *Applied Numerical Mathematics*, Vol. 25(2-3), pp. 303-319, 1997.

[55] Selçuk, N. and I. Ayranci, The Method of Lines Solution of the Discrete Ordinates Method for Radiative Heat Transfer in Enclosures Containing Scattering Media, *Numerical Heat Transfer Part B-Fundamentals*, Vol. 43(2), pp. 179-201, 2003.

[56] Leckner, B., Spectral and Total Emissivity of Water Vapor and Carbon Dioxide, *Combustion and Flame*, Vol. 19, pp. 33-48, 1972.

[57] Ströhle, J., *Spectral Modelling of Radiative Heat Transfer in Industrial Furnaces*, Shaker Verlag, Aachen, 2004.

[58] Edwards, D.K. and A. Balakrishnan, Thermal Radiation by Combustion Gases, *International Journal of Heat and Mass Transfer*, Vol. 16, pp. 25-40, 1973.

[59] Chang, S.L. and K.T. Rhee, Blackbody Radiation Functions, *International Communications in Heat Mass Transfer*, Vol. 11, pp. 451-455, 1984.

[60] Mengüç, M.P. and R. Viskanta, On the Radiative Properties of Polydispersions: A Simplified Approach, *Combustion Science and Technology*, Vol. 44, pp. 143-159, 1985.

[61] Kim, T.K., J.A. Menart, and H.S. Lee, Nongray Radiative Gas Analyses Using the S-N Discrete Ordinates Method, *ASME Journal of Heat Transfer*, Vol. 113, pp. 946-952, 1991.

[62] Kayakol, N., N. Selçuk, I. Champbell, and Ö.L. Gülder, Performance of Discrete Ordinates Method in a Gas Turbine Combustor Simulator, *Experimental Thermal and Fluid Science*, Vol. 21, pp. 134-141, 2000.

[63] Karamehmetoğlu, S., The Method of Lines Solution of Discrete Ordinates Method for Radiative Heat Transfer in Cylindrical Enclosures, M. Sc. Thesis, Middle East Technical University, Ankara, 2002.

[64] Modest, M.F., *Radiative Heat Transfer*, Academic Press Inc, San Diego, 2003.

APPENDIX A

ORDINATES AND WEIGHTS FOR S_N APPROXIMATIONS

Table A.1 Discrete ordinates for the S_N approximation for axisymmetric cylindrical geometry

Order of Approximation	Ordinates			Weights
	μ_m	ς_m	ξ_m	w_m
S_2	0.5000000	0.7071068	0.5000000	3.1415927
S_4	0.2958759	0.2958759	0.9082483	1.0471976
	0.2958759	0.9082483	0.2958759	1.0471976
	0.9082483	0.2958759	0.2958759	1.0471976
S_6	0.1838670	0.1838670	0.9656013	0.3219034
	0.1838670	0.6950514	0.6950514	0.7252938
	0.6950514	0.1838670	0.6950514	0.7252938
	0.1838670	0.9656013	0.1838670	0.3219034
	0.6950514	0.6950514	0.1838670	0.7252938
	0.9656013	0.1838670	0.1838670	0.3219034
S_8	0.1422555	0.1422555	0.9795543	0.3424718
	0.1422555	0.5773503	0.8040087	0.1984568
	0.5773503	0.1422555	0.8040087	0.1984568
	0.1422555	0.8040087	0.5773503	0.1984568
	0.5773503	0.5773503	0.5773503	0.9234358
	0.8040087	0.1422555	0.5773503	0.1984568
	0.1422555	0.9795543	0.1422555	0.3424718
	0.5773503	0.8040087	0.1422555	0.1984568
	0.8040087	0.5773503	0.1422555	0.1984568
	0.9795543	0.1422555	0.1422555	0.3424718

APPENDIX B

EXPONENTIAL WIDE BAND MODEL PARAMETERS

B.1 Calculation of Band Strength Parameter, α:

The empirical correlation form which the band strength parameter, α, is calculated is given by Edwards [22] as follows:

$$\alpha(T) = \alpha_0 \frac{\psi^*(T)}{\psi^*(T_0)} = \alpha_0 \frac{\left\{1-\exp\left(-\sum_{k=1}^{m} u_k \delta_k\right)\right\}\psi(T)}{\left\{1-\exp\left(-\sum_{k=1}^{m} u_{0,k} \delta_k\right)\right\}\psi(T_0)} \tag{B.1}$$

where

$$\psi(T) = \frac{\prod_{k=1}^{m} \sum_{\upsilon_k=\upsilon_{0,k}}^{\infty} \frac{(\upsilon_k + g_k + |\delta_k| - 1)!}{(g_k - 1)!\upsilon_k!} e^{-u_k \upsilon_k}}{\prod_{k=1}^{m} \sum_{\upsilon_k=0}^{\infty} \frac{(\upsilon_k + g_k + -1)!}{(g_k - 1)!\upsilon_k!} e^{-u_k \upsilon_k}} \tag{B.2}$$

and

$$u_k = \frac{hc\eta_k}{kT}, \qquad u_{0,k} = \frac{hc\eta_k}{kT_0} \tag{B.3}$$

$$\upsilon_{0,k} = \begin{cases} 0 & for \ \ \delta_k \geq 0 \\ |\delta_k| & for \ \ \delta_k \leq 0 \end{cases} \tag{B.4}$$

T_0 is the reference temperature and is taken as 100 K, h (=6.6261×10^{-34} J.s) is the Planck's constant, c (=2.998×10^8 m/s) is the speed of light and k (=1.3807×10^{-23} J/K) is Boltzmann's constant. The summation over υ_k were carried until 10 and 20 for H_2O and CO_2, respectively. Beyond these numbers the results remain unchanged. Values of EWBM correlation parameters m, band strength parameter at the reference condition, $\alpha_0\left(=\alpha(T_0)\right)$, the lowest possible initial state, $\upsilon_{0,k}$, change in vibrational quantum number, δ_k , vibrational quantum numbers, η_k, statistical weights (unity for non-degenerate vibrations, greater for degenerate ones), g_k are tabulated in Tables B.1 and B.2 [64] for CO_2 and H_2O, respectively. For calculation of $\psi(T_0)$, temperature T is simply set T_0 in Eq. (B.2)

Table B.1 Exponential wide band model correlation parameters for H_2O

Band Location		Pressure Parameters		Correlation Parameters		
η_0 [cm^{-1}]	δ_k	n	b	α_0 [cm^{-1}/(g/m^2)]	γ_0	ω_0 [cm^{-1}]
H_2O	m=3, η_1=3652 cm^{-1}, η_2=1595 cm^{-1}, η_3=3756 cm^{-1}, g_k = (1,1,1)					
140	(0,0,0)	1	$8.6\sqrt{(T_0/T)}+0.5$	5.455	0.143	69.3
1600	(0,1,0)	1	$8.6\sqrt{(T_0/T)}+0.5$	41.2	0.094	56.4
3760	(0,2,0)	1	$8.6\sqrt{(T_0/T)}+0.5$	0.2	0.132	60.0
	(1,0,0)			2.3		
	(0,0,1)			23.4		
5350	(0,1,1)	1	$8.6\sqrt{(T_0/T)}+0.5$	3.0	0.082	43.1
7250	(1,0,1)	1	$8.6\sqrt{(T_0/T)}+0.5$	2.5	0.116	32.0

Table B.2 Exponential wide band model correlation parameters for CO_2

Band Location		Pressure Parameters		Correlation Parameters		
η_0 [cm^{-1}]	δ_k	n	b	α_0 [$cm^{-1}/(g/m^2)$]	γ_0	ω_0 [cm^{-1}]
CO_2	m=3, η_1=1351cm^{-1}, η_2=666 cm^{-1}, η_3=2396 cm^{-1}, g_k = (1,2,1)					
667	(0,1,0)	0.7	1.3	19.0	0.062	12.7
960	(-1,0,1)	0.8	1.3	2.47×10^{-9}	0.040	13.4
1060	(-1,0,1)	0.8	1.3	2.47×10^{-9}	0.119	10.1
2410	(0,0,1)	0.8	1.3	110.0	0.247	11.2
3660	(1,0,1)	0.65	1.3	4.0	0.133	23.5
5200	(2,0,1)	0.65	1.3	0.06	0.393	34.5

B.2 Calculation of Line Overlap Parameter, β:

The empirical correlation form which the line overlap parameter, β, is calculated is given by Edwards [22] as follows:

$$\beta(T) = \gamma P_e = \gamma_0 \sqrt{\frac{T_0}{T}} \frac{\Phi(T)}{\Phi(T_0)} P_e \tag{B.5}$$

where

$$\Phi(T) = \frac{\left\{ \prod_{k=1}^{m} \sum_{\upsilon_k=\upsilon_{0,k}}^{\infty} \sqrt{\frac{(\upsilon_k + g_k + |\delta_k| - 1)!}{(g_k - 1)!\upsilon_k!} e^{-u_k \upsilon_k}} \right\}^2}{\prod_{k=1}^{m} \sum_{\upsilon_k=\upsilon_{0,k}}^{\infty} \frac{(\upsilon_k + g_k + |\delta_k| - 1)!}{(g_k - 1)!\upsilon_k!} e^{-u_k \upsilon_k}} \tag{B.6}$$

and

$$P_e = \left[\frac{p}{p_0} \left(1 + (b-1) \frac{p_a}{p} \right) \right]^n \tag{B.7}$$

Pe is the effective pressure. P_0 is the reference pressure and is taken as 1 atm and P_a is the partial pressure of the absorbing gas. The summation over υ_k were carried until 10 and 20 for H_2O and CO_2, respectively. Beyond these numbers the results remain unchanged. Values of EWBM correlation parameters, pressure parameters n and b, line overlap parameter at the reference condition, $\gamma_0 \left(= \gamma(T_0)\right)$, the lowest possible initial state, $\upsilon_{0,k}$, change in vibrational quantum number, δ_k, vibrational quantum numbers, η_k, statistical weights (unity for non-degenerate vibrations, greater for degenerate ones), g_k values are tabulated in Tables B.1 and B.2 [64] for CO_2 and H_2O, respectively. For calculation of $\Phi(T_0)$, temperature T is simply set T_0 in Eq. (B.6)

1.1 Calculation of Band Width Parameter, ω:

The empirical correlation form which band width parameter, ω, is calculated is given by Edwards [22] as follows:

$$\omega(T) = \omega_0 \sqrt{\frac{T}{T_0}} \tag{B.8}$$

where ω_0 is band width parameter at the reference condition listed in Tables B.1 and B.2 [64] for CO_2 and H_2O, respectively.

APPENDIX C

INITIAL PARAMETERS FOR THE ODE SOLVER (ROWMAP) SUBROUTINE

The radiation codes developed in this study require specifications of certain input parameters for the ODE solver subroutine in addition to the input data relevant with the physical system and subdivisions of angular and spatial domains which are presented in the text. Initial parameters for the ODE solver are the absolute and relative error tolerances (ABSERR and RELERR), time interval for printing (TP) and convergence criteria for terminating the integration. Tables C.1 and C.2 present the input parameters utilized to obtain solutions for the one-dimensional and two-dimensional test cases, respectively.

Table C.1 Initial parameters utilized for ROWMAP subroutine for the one-dimensional test cases

Test Case	ABSERR	RELERR	TP	$\in$
1	0.001	0.001	10	0.001
2	0.001	0.001	10	0.001
3	0.001	0.001	10	0.001
4	0.001	0.001	10	0.001
5	0.001	0.001	10	0.001
6	0.001	0.001	10	0.001
7	0.001	0.001	10	0.001
8	0.001	0.001	10	0.001

Table C.2 Initial parameters utilized for ROWMAP subroutine for the two-dimensional test cases

	ABSERR	RELERR	TP	$\in$
Test Case 1	0.001	0.001	10	0.001
Test Case 3	0.001	0.001	10	0.001

APPENDIX D

DETAILS OF MOL SOLUTION OF DOM FOR ONE-DIMENSIONAL TEST CASES

The physical situation in one-dimensional test cases consist of two infinitely long parallel plates containing a uniform or non-uniform, nongray, absorbing-emitting medium confined within gray, diffuse walls. For radiative transfer in a plane-parallel geometry the WSGG form of RTE (Eq. 2.11) simplifies as follows

$$\mu \frac{dI_j}{dx} = \kappa_j (a_j I_b - I_j(x, \mathbf{\Omega})) \tag{D.1}$$

where x is the distance along the axis perpendicular to the plates and μ stands for the direction cosine with respect to the x-axis. The subscript j denotes the spectral division with respect to gray gases.

The boundary conditions for intensities leaving the walls that diffusely emit and reflect radiant energy are as follows;

$$I_j(0,\mu) = \varepsilon_w a_j I_b(T_{w1}) + 2(1-\varepsilon_w) \int_{-1}^{0} I_j(0,\mu') \left|\mu'\right| d\mu' \qquad \text{for} \quad \mu > 0 \tag{D.2}$$

$$I_j(L,\mu) = \varepsilon_w a_j I_b(T_{w2}) + 2(1-\varepsilon_w) \int_{0}^{1} I_j(L,\mu') \left|\mu'\right| d\mu' \qquad \text{for} \quad \mu < 0 \tag{D.3}$$

The discrete ordinates representation of Eq. (D.1) was obtained by evaluating the equation at each ordinate m (m=1, 2, 3, …, M);

$$\mu_m \frac{dI_j^m}{dx} = \kappa_j (a_j I_b - I_j^m(x, \mathbf{\Omega})) \tag{D.4}$$

where μ_m stand for direction cosines and a_j are the blackbody weights determined from the absorption line blackbody distribution functions. Similarly, the boundary conditions were obtained by evaluating Eqs. (D.2) and (D.3) at each ordinate;

$$I_j^m(0, \mu_m) = \varepsilon_w a_j I_b(T_{w1}) + \frac{(1 - \varepsilon_w)}{\pi} \sum_{\mu_{m'} < 0} I_j^{m'}(0, \mu_{m'}) \mu_{m'} w_{m'} \qquad \text{for} \quad \mu_m > 0 \tag{D.5}$$

$$I_j^m(L, \mu_m) = \varepsilon_w a_j I_b(T_{w2}) + \frac{(1 - \varepsilon_w)}{\pi} \sum_{\mu_{m'} > 0} I_j^{m'}(L, \mu_{m'}) \mu_{m'} w_{m'} \qquad \text{for} \quad \mu_{m'} < 0 \tag{D.6}$$

where *wm* represent quadrature weights tabulated in Table D.1 together with the direction cosines, μ_m.

Table D.1 Direction cosines and weights for one-dimensional parallel plate geometry

Order of Approximation	Ordinates μ_m	Weights w_m
S_2	0.5000000	1.0000000
S_4	0.2958759	0.6666667
	0.9082483	0.3333333
S_6	0.1838670	0.4357983
	0.6950514	0.4617364
	0.9656013	0.1024650
S_8	0.1422555	0.3443658
	0.5773503	0.4202803
	0.8040087	0.1263415
	0.9795543	0.1090122

Once the intensities at each ordinate and at each grid point for each gray gas are evaluated, the net radiative flux and source term can be obtained from the following equations

$$q_{net} = \varepsilon_w \left(\sum_j^{NG} \sum_m^M w_m \mu_m I_j^m - a_j \pi I_b \right) \tag{D.7}$$

$$div\mathbf{q} = \sum_j^{NG} \kappa_j (4\pi a_j I_b - \sum_m^M w_m I_j^m) \tag{D.8}$$

In order to solve the discrete ordinates equations with MOL, false-transients method was implemented by incorporating a pseudo-time derivative to Eq. (D.4).

$$k_t \frac{\partial I_j^m}{\partial t} = -\mu_m \frac{\partial I_j^m}{\partial x} + \kappa_j (a_j I_b - I_j^m(x, \mathbf{\Omega})) \tag{D.9}$$

The resulting system of PDEs was transformed into an ODE initial value problem by using the method of lines approach. The transformation was carried out by two-point and using three-point upwind discretization schemes (DSS012 and DSS014) for the spatial derivative. Starting from an initial condition for radiation intensities in all discrete directions, the resulting ODE system was integrated until steady-state by using a powerful ODE solver, namely ROWMAP [54].

APPENDIX E

INDEPENDENT PARAMETERS FOR THE TEST CASES

The parameters required for the parameter independent solutions are tabulated in Tables E.1 and E.2 for one-dimensional and two-dimensional test cases, respectively.

Table E.1 Independent parameters for one-dimensional test cases

Test Case		Model	Order of Approximation	Number of Grid Points	Spatial Differencing Scheme	Number of Gray Gases
1	a	WBCK	S_8	21	DSS012	20
		SLW	S_4	31	DSS014	10
		Gray Gas	S_4	21	DSS012	-
	b	WBCK	S_8	31	DSS012	20
		SLW	S_4	51	DSS014	15
		Gray Gas	S_6	21	DSS014	-
2	a	WBCK	S_6	31	DSS012	10
		SLW	S_4	51	DSS012	10
		Gray Gas	S_6	21	DSS012	-
	b	WBCK	S_4	21	DSS012	10
		SLW	S_4	51	DSS012	20
		Gray Gas	S_8	21	DSS012	-
	c	WBCK	S_4	31	DSS012	10
		SLW	S_4	31	DSS014	10
		Gray Gas	S_6	21	DSS012	-
3		WBCK	S_4	21	DSS012	10
		SLW	S_6	31	DSS012	15
		Gray Gas	S_4	21	DSS012	-
4		WBCK	S_6	21	DSS012	10
		SLW	S_4	41	DSS012	10
		Gray Gas	S_8	21	DSS012	-

Table E.1 Independent parameters for one-dimensional test cases (Continued)

Test Case	Model	Order of Approximation	Number of Grid Points	Spatial Differencing Scheme	Number of Gray Gases
5	WBCK	S_6	51	DSS012	15
	SLW	S_6	41	DSS012	10
	Gray Gas	S_8	21	DSS012	-
6	WBCK	S_4	21	DSS012	15
	SLW	S_6	31	DSS014	10
	Gray Gas	S_6	21	DSS012	-
7	WBCK	S_8	51	DSS012	20
	SLW	S_4	51	DSS012	15
	Gray Gas	S_4	21	DSS012	-
8	WBCK	S_4	21	DSS014	20
	SLW	S_6	31	DSS012	10
	Gray Gas	S_6	21	DSS012	-

Table E.2 Independent parameters for two-dimensional test cases

Test Case	Model	Order of Approximation	Number of Grid Points	Spatial Differencing Scheme	Number of Gray Gases
1	WBCK	S_4	25×81	DSS012	10
	SLW	S_4	25×81	DSS012	10
	Gray Gas	S_4	13×41	DSS012	-
2 (GTCS)	SLW	S_4	27×29	DSS012	10
	Gray Gas	S_4	27×29	DSS012	-